

DISSERTATION

High Temperature Superconductors For Fusion Magnets

ausgeführt zum Zwecke der Erlangung
des akademischen Grades eines
Doktors der technischen Wissenschaften
unter der Leitung von

Univ. Prof. Dr. phil. Dr. h.c. Harald W. Weber
E141
Atominstitut

eingereicht an der Technischen Universität Wien
Fakultät für Physik

von

Mag. Michal Chudý
e0727452
Alliiertenstraße 4
1020 Wien

Wien, Dezember 2010

Acknowledgements

I would like to thank Prof. H.W. Weber for giving me an opportunity to spend the last few years at the Atominstitut. It was my pleasure to work under his supervision on such an exciting scientific topic as superconductivity. I thank very much for all the support, patience and freedom which I had on my experimental work.

Thanks to Michael Eisterer for his support and patience. This work would not be like it is without his valuable ideas, advices and frequent discussions.

Then special thanks to B. Holzhapfel for his outstanding leadership of the NESPA network programme which covered the financial support for this scientific work; to B.A. Glowacki for his great supervision during my stay in Cambridge.

Thanks to all my colleagues in the group for good atmosphere and work environment, to Marcus Weigand, René Fuger, Florian Hengstberger and Tom Withnell for assistance by the experiments.

Thanks to all NESPA fellows for collaboration and great times on the NESPA events.

Thanks to Wolfgang Moens, Lukas Jadachowski, Matej Klas, Ondrej Štuller, Tibor Óbert for interest in my work and interesting discussions regarding physics. Many thanks to all my friends and also to those who were not interested in physics, but supported me.

And finally, special thanks to all my family, my parents, my sister Zuzana and of course to Katka Kraliková for their support and patience.

Kurzfassung

Die Anwendung der Kernfusion zur Energieerzeugung ist gegenwärtig eine der größten technischen Herausforderungen. Die leistungsstarke zweite Generation von Hochtemperatursupraleitenden Bandleitern (sogenannte Coated Conductors), die auf dem Kuprat Yttrium-Barium-Kupfer-Oxid ($\text{YBa}_2\text{Cu}_3\text{O}_{7-\delta}$) basieren, sind dabei mögliche Kandidaten für den Einsatz in den Magnetspulen künftiger Fusionskraftwerke und müssen hohe Fluenzen von schnellen Neutronen überstehen, die während der Fusionsreaktion erzeugt werden. Deshalb wird in dieser Arbeit eine detaillierte Studie über den Einfluss der Bestrahlung mit schnellen Neutronen auf Bandsupraleiter durchgeführt. Als Proben wurden die besten kommerziell verfügbaren Coated Conductors verwendet. Die Bestrahlung wurde im TRIGA Mark II Reaktor am Atominstitut in Wien durchgeführt.

Die Proben wurden in mehreren Stufen bestrahlt und nach jedem Schritt wurden Transportstrom und Magnetisierungsmessungen durchgeführt. Da schnelle Neutronen zusätzliche Verankerungszentren im Supraleiter erzeugen, verändert sich dessen Leistung deutlich. Die Bestrahlung erhöht die kritischen Stromdichte, kann aber nach einer gewissen Stärke auch zu einer Erniedrigung führen.

Die Diskussion der Ergebnisse ist durch die zwei Hauptaspekte der Arbeit bestimmt. Vorrangig ist dabei die Untersuchung der Leistungsfähigkeit im Hinblick auf Fusion. Die Proben wurden auf eine Fluenz von über $1 \times 10^{22} \text{ m}^{-2}$ bestrahlt, was dem gesamten Fluss entspricht, der auf den Magnetpositionen während der ITER-Lebensdauer auftritt. Die Leistung der Bandsupraleiter wird dann mit den Anforderungen eines Fusionskraftwerks verglichen. Da die Bestrahlungsbedingungen in Kernspaltungsreaktoren unterschiedlich von jenen eines Kernfusionreaktors sind, wird eine Studie durchgeführt, um die Verwendbarkeit des TRIGA Mark II Reaktors zu bestätigen. Die Bandleiter bestehen aus chemischen Elementen, die sich während der Bestrahlung aktivieren. Deshalb werden die Konsequenzen auf die Anwendbarkeit in der Fusion diskutiert.

Der zweite Teil der Arbeit behandelt das Phänomen der Flusslinienverankerung durch die Defekte, die durch die Bestrahlung mit schnellen Neutronen entstehen. Die zahlreichen Messungen bieten genug Information für eine umfangreiche Studie mit Schwerpunkt auf dem Mechanismus der Flusslinienverankerung. Die winkelabhängigen Transportmessungen sind dabei besonders interessant. Spezielle Merkmale der Winkelabhängigkeit vor

und nach der Bestrahlung mit den schnellen Neutronen werden definiert, analysiert und erklärt. Die Wirkung der durch die schnellen Neutronen erzeugten Defekte auf die Fluslinienverankerung wird mit den Ergebnissen anderer Autoren verglichen. Zum Schluss wird ein komplexer Pinningmechanismus vorgeschlagen.

Abstract

Thermonuclear fusion is one of the main challenges of current scientific research. High temperature superconductors are considered to be the most likely candidates to be applied in future fusion power plants. The second generation of high temperature superconducting wires (coated conductors) are the most powerful high temperature superconducting wires. They are usually based on a cuprate structure of yttrium-barium-copper-oxide ($\text{YBa}_2\text{Cu}_3\text{O}_{7-\delta}$), which has a critical temperature of 92 K. The superconducting wires applied in the coils of a fusion reactor have to withstand significant fast neutron fluences. The neutrons are produced directly by the fusion reaction. Therefore, a detailed investigation of fast neutron irradiation on coated conductors was performed in this thesis. The best available commercial coated conductors from the world leading manufacturers (SuperPower, EHTS - Bruker, American Superconductor - AMSC) were chosen as samples. TRIGA Mark II reactor in Vienna was employed as the irradiation facility. The samples were sequentially irradiated and, after each step, fully characterized by direct transport and magnetization measurements. The most complex characterization has been performed on the unirradiated samples.

The fast neutrons introduce additional pinning centres into the superconductor, which can significantly change the performance of the superconductor. The critical current densities are often enhanced, but can also be reduced after a certain irradiation level is reached. The discussion and analysis of the results can be divided into two goals: The first is studying the performance with regard to fusion requirements. The samples will be irradiated beyond a fast neutron fluence of $1 \times 10^{22} \text{ m}^{-2}$, which corresponds to the ITER lifetime fluence at the magnet area. The performance of the coated conductors will be then compared with the fusion requirements. The irradiation conditions in fission and fusion reactors are very different. Therefore, a detailed study approving the employment of the TRIGA Mark II reactor as an irradiation source simulating the fluences of fusion machines will be presented. The coated conductors consist of chemical elements, which are activated and transmuted during the irradiation procedure. Thus the superconducting wire becomes a radiation emitter. The consequences resulting from this activation and transmutation for the coated conductors regarding the performance and the fusion applications will be also investigated and discussed.

The second goal deals directly with the phenomena of the flux pinning enhancement caused by fast neutron irradiation. The numerous measurements performed for fusion studies offer enough data to perform a study with focus on the flux pinning mechanism in coated conductors. The angular resolved transport measurements will be especially interesting for this purpose. The coated conductor from SuperPower exhibits unique critical current dependence of its angle as a function of the applied external magnetic field. Therefore, the unique features in the dependence will be defined, analyzed and explained before and after irradiation by fast neutrons. The effect caused by the pinning centres introduced by fast neutrons will be connected with other phenomena studied by various authors. It will be presented as a complex pinning mechanism.

Contents

1	Introduction	1
1.1	Thermonuclear fusion and superconductivity	1
1.2	Introduction to neutron irradiation of superconductors	3
2	High Temperature Superconductors (HTS)	5
2.1	Supercurrent flow and flux pinning	5
2.2	Fabrication methods of HTS wires	8
2.2.1	First generation of HTS wires	8
2.2.2	Second generation of HTS wires	9
2.3	Samples	12
2.3.1	SuperPower	12
2.3.2	European High Temperature Superconductors	13
2.3.3	American Superconductor	14
2.4	Superconductors for fusion magnets	16
3	Irradiation	19
3.1	TRIGA Mark II Reactor	19
3.2	Neutron interaction with matter	21
3.2.1	Elastic scattering	21
3.2.2	Nuclear reactions	22
3.3	Coated conductors in fission and fusion reactors	23
3.3.1	Isotope effect	23
3.3.2	Lattice defects	24
3.3.3	Secondary radiation from created isotopes	26
3.4	Irradiation in a fission reactor for fusion applications	28
3.5	Irradiation procedure and analysis	29
4	Methods and Instrumentation	32
4.1	Transport Measurements	32
4.1.1	Critical currents (I_c), Critical current densities (J_c)	33

4.1.2	Critical Temperature	34
4.1.3	The electromagnet set-up	35
4.1.4	6 T set-up	36
4.1.5	17 T set-up	37
4.1.6	2-axis high current goniometer	38
4.2	Magnetization measurements	40
4.2.1	The Bean model	40
4.2.2	Vibrating Sample Magnetometer (VSM)	41
5	Measurements	43
5.1	Angular resolved measurements - anisotropy studies	43
5.1.1	Maximal Lorentz force characterization	43
5.1.2	Anisotropy at 77 K	44
5.1.3	Anisotropy of the SuperPower CC	49
5.1.3.1	X-ray diffraction (XRD)	50
5.1.3.2	Anisotropy measurements	51
5.1.3.3	Other features of asymmetry	54
5.2	Characterization in a 2-axis goniometer	57
5.2.1	Standard 2-axis measurements	57
5.2.2	Additional asymmetry measurements on the SuperPower CC	60
5.2.3	Isocurrent investigations	64
5.3	Measurements after irradiation	65
5.3.1	SuperPower	65
5.3.1.1	Angular resolved transport measurements up to fields of 6 T	68
5.3.1.2	Transport measurements in the 17 T set-up	73
5.3.1.3	The influence of fast neutron irradiation on T_c and the irreversibility fields	75
5.3.1.4	VSM measurements	77
5.3.2	EHTS	79
6	Impact of Neutron Irradiation on Coated Conductors	85
6.1	Pinning mechanism	85
6.1.1	Blatter scaling of the SuperPower CC	87
6.1.2	Strong and weak pinning	89
6.1.3	$J_c(\varphi)$ before and after irradiation	93
6.2	Thermonuclear fusion	95
6.2.1	Requirements for fusion magnets	95

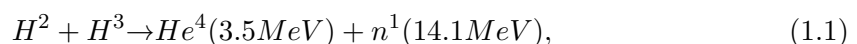
Contents

6.2.2	Critical superconducting design parameters	97
6.2.3	Results and fusion requirements	100
7	Summary	101

1 Introduction

1.1 Thermonuclear fusion and superconductivity

Over the last few decades, non-renewable resources are consumed much faster than ever before. Pollution and coupled global warming begin to influence our lives in negative ways. The world population is reaching enormous numbers and it is starting to be very hard to satisfy even basic nutritive and material needs of everyone. The situation with energy production is very similar. As the non-renewable resources are getting used up, the production of electricity will be increasingly difficult and expensive. New technologies and developments allow us to manufacture devices with much better energy efficiency, but it might be still not enough, as the demand is continuously increasing. Countries such as India and China, which cover about one-third of the world population, are being massively industrialized. A similar process is happening also in the third world countries. Fast industrialization is connected with a huge pressure on the environment. This is one of the reasons, why most developed countries in the world are trying to promote science and make legal regulations to use only the best and the cleanest technologies for electricity production. The European Union especially is very active in this area and supports many relevant projects and programs. It strongly supports renewable energy sources, which are very important because of their accessibility. However, we will probably never be able to gain all the needed energy from them due to their low efficiency or reliability. At present, these sources are considered to be more a secondary energy source. Nowadays, the most promising solution for the energy problem seems to be nuclear fusion. Thousands of researchers and engineers all around the world are working on national and international projects related to fusion. The biggest project is ITER, an international project, in which basically every developed country takes part. ITER will be a TOKAMAK (from russian abbreviation: toroidal chamber with axial magnetic field) type of the reactor. TOKAMAK is a machine producing a toroidal magnetic field to confine a plasma. It was invented in the 1950s by the Soviet scientists Igor Yevgenyevich Tamm and Andrei Sakharov, inspired by an original idea of Oleg Lavrentyev [1]. ITER will be based on the fusion reaction



which runs under ~ 150 mil. $^{\circ}\text{C}$ in a TOKAMAK reactor. At these temperatures, the plasma must be confined so that it does not touch the vacuum vessel. It is the reason, why the strong magnetic fields are necessary. In ITER all the magnets and coils will be made of low temperature superconductors (NbTi, Nb₃Sn). The employment of superconductors in the reactor was chosen, because the required magnetic fields are beyond the performance available from conventional magnets. The second reason is a better energy efficiency of superconducting devices than of conventional ones. Superconductors do not lose any energy by ohmic heating and once the magnet reaches a certain magnetic field with corresponding current, the magnet will keep the field constant without any additional energy source, as long as the wires in the magnet are in the superconducting state; it could be seconds, minutes, but even years. Some energy dissipation occurs by ramping a current up or down into the coil (AC-losses). Some energy is also needed for cooling to keep the temperature in the area of superconductivity. But the sum of these losses means much lower energy demand than the ohmic loss in conventional conductors. These superconductors will be cooled by supercritical helium to the target temperature of about 4 K in ITER. High temperature superconductors, which this thesis deals with, should be employed in the next generation of a fusion reactor (DEMO), which is meant to produce electricity for the grid. Therefore the highest efficiency is needed. The latest ITER reports show that high temperature superconductors will be employed even in ITER. It will be only a small employment - current leads [2], which will supply the current to the other superconducting parts within the main cryostat. High temperature superconductors were discovered by Alex Müller and J. Georg Bednorz in the Ba-La-Cu-O system in 1986 [3]. From this point a massive development in the cuprate high temperature superconductors (HTS) has been started. The critical temperature was increased from ~ 40 K in Ba-La-Cu-O up to 153 K in Hg-Ba-Ca-Cu-O under high pressure. (Even a critical temperature of ~ 255 K was reported in Tl-Ba-Ca-Cu-O under the very high pressure of 5 Gpa [4].) In 2008, a new family of iron based superconductors was discovered by the group of Hideo Hosono [5]. This opened new directions of the HTS research. Currently the most preferred material suitable for various applications is Y-Ba-Cu-O (YBCO) or more general (RE)BCO, where (RE) means a rare earth element, e.g. Y-Yttrium, Sm -Samarium. Both bulks and wires are fabricated from this material. The wires are coated conductors (CCs) or second generation superconducting wires. The first generation of superconducting wire was based on Bi-Sr-Ca-Cu-O (BISCCO or Bi-2212 and Bi-2223 - the numbers mean the quantities of Bi, Sr, Ca and Cu in the crystal). The critical temperatures of these materials are quite high, 94 K and 110 K, but the performance in higher magnetic fields is rather low at 77 K. The main advantage of these first generation superconductors is the easier

and cheaper fabrication process than in the case of the second generation. But in the last years, the fabrication methods of coated conductors have made a massive progress and it is not a problem to fabricate top quality tape with very high critical current densities and homogeneous distribution in scale of hundreds meters. These tapes are strong candidates to be employed in future fusion reactors (DEMO), but before it happens, a lot of scientific research and testing needs to be done. This thesis is also part of that research and hopefully will be a small step forward in the research of superconductors for fusion magnets.

1.2 Introduction to neutron irradiation of superconductors

The main part of this thesis deals with the irradiation of the second generation of the high temperature superconducting wires. The irradiation has been provided for two purposes: The first purpose concerns the thermonuclear fusion and the possible future application of CCs in fusion machines. The second purpose is rather theoretical and includes studying flux pinning and its changes after fast neutron irradiation.

The CCs, which will be employed in future fusion power plants have to withstand significant fluences of fast neutrons. The neutron is the main energy carrier in the fusion reaction from Eq. 1.1. An ideal case would be that all the energy transported by the neutron is absorbed in the wall of the vacuum vessel (blanket) and then transformed into electrical energy. However, some fraction of neutrons penetrates into the magnet system in a real thermonuclear machine. These fluxes are significantly lower, than the fluxes impinging on the blanket elements. The neutron energy is also lower than 14.1 MeV. The neutron energy distribution at the magnet position in a fusion reactor will be presented and discussed later (Sec. 3.4, Figure 3.5). It is well known, that some types of irradiation can improve some superconducting properties of conventional and high temperature superconductors [6, 7], which is very good news for fusion. Mainly neutron irradiation, but also other irradiation types, change the material composition resulting in activation of elements. The superconductor becomes radioactive, which prohibits its employment in any possible applications with the exception of thermonuclear fusion. However, irradiated superconductors enjoy a great attention from scientists, mainly in the physics of pinning. They are an interesting research material with numerous unanswered and unexplained questions. Due to rather small neutron fluxes at the magnet location in fusion machines (compared to the fluxes impinging on the blanket), the TRIGA Mark reactor II in Vienna was employed as an irradiation facility. The neutron fluxes in the middle of the reactor core are high enough to reach in couple of days fluences of fast neutrons, which corre-

spond to the estimated ITER whole lifetime fluence. This topic will be more described in Chapter 3. Moreover, this thesis will present results important for the future employment of high temperature superconductors in fusion and it will try to explain some aspects of the physics of pinning. This thesis practically continues the work of R. Fuger [8]. The measurement techniques and a part of the samples remain the same. However, additional measurements, straight focusing into particular goals and measurements after different levels of irradiation have been performed. In addition, characterization of newer types of CCs has been done either. This thesis is less focused on the description of experimental techniques and instruments but rather on the relevant problems concerning neutron irradiation in a fission reactor for thermonuclear fusion.

2 High Temperature Superconductors (HTS)

2.1 Supercurrent flow and flux pinning

The discovery of high temperature superconductors launched an intensive development in the physics of pinning. All the HTS are type II superconductors, which means that they stay in the superconducting state up to a magnetic field $B_{c2} = \kappa\sqrt{2}B_c$, where B_c is the thermodynamic critical field. However, it still does not mean that they are able to transport high transport currents without any resistance. The Lorentz force causes a movement of the penetrated magnetic flux, which creates a voltage (according to the Maxwell-Faraday equation). If any voltage is detected, currents are no longer loss free. The introduction of “small” defects into the crystal lattice reduces the mean free path of charge carriers, which increases the Ginzburg-Landau (GL) parameter κ and B_{c2} as well. However, it is not still clear if this mechanism remains the same for the high temperature superconductors. The “small” defects are called pinning centres or pinning sites and are responsible for high supercurrent flow in the type II superconductors. The flux lines are attracted by any defects, which are either not superconducting or have a large GL parameter κ . Around the flux lines, as the superconductor tries to shield the penetrated magnetic field, supercurrent vortices, Abrikosov vortices, are created. The vortex field B_v can be approximated by [9]:

$$B_v = \frac{\phi_0}{2\pi\lambda^2} \begin{cases} \ln\left(\frac{\lambda}{r}\right) & \text{if } \xi < r \ll \lambda \\ \left(\frac{\pi\lambda}{2r}\right)^{\frac{1}{2}} e^{-\frac{r}{\lambda}} & \text{if } r \gg \lambda \end{cases} .$$

A sketch of a pinning centre together with the Abrikosov vortex is shown in Figure 2.1.

Here, it is important to note that the superconductor can transport current without resistance, until the vortices begin to move. The movement is initialized at the moment the pinning force is lower than the Lorentz force. The volume pinning force usually does not come from single pinned flux lines. The flux lines interact with each other. If the defects in a superconductor are very small and distributed randomly, they are unable to pin a flux

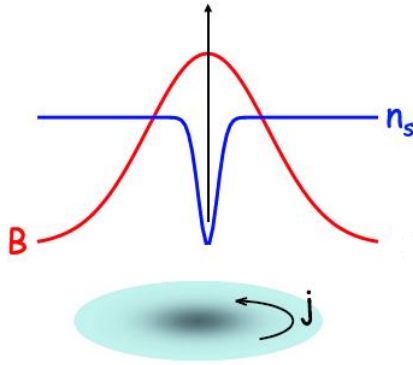


Figure 2.1: Abrikosov vortex, n_s -Cooper pairs density, B - penetrating magnetic field.

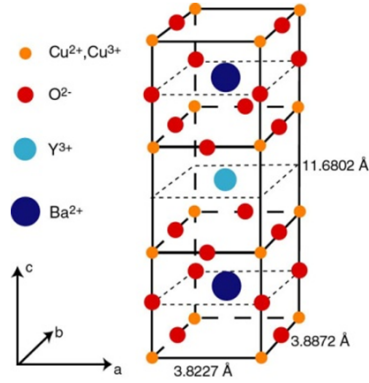


Figure 2.2: Layered structure of an YBCO crystal.

line lattice effectively. What they can do, at least in low temperature superconductors, is to affect the secondary superconducting parameters through the charge carrier main free path reduction. However, bigger defects such as dislocations, stacking faults, second phase precipitates etc. can pin the flux line lattice.

Coated conductors are the second generation of HTS wires and are designed for high current transport at high magnetic fields. They have a layered structure consisting of several buffer layers with various functions. YBCO creates crystals, which belong to a perovskite structure (Figure 2.2). It is a layered structure with the best supercurrent transport properties within the ab plane. Low angle grain boundaries are also crucial for high supercurrent transport. As a consequence, the crystals have to be biaxially textured in a film. Only by the biaxial texture of the crystals, optimal conditions for the highest supercurrent transport can be achieved. Therefore, special manufacturing techniques are employed to ensure the right texture of the YBCO thin film. These techniques will be presented later in more detail (Sec. 2.2). The fabrication process is one of the crucial points defining the pinning in YBCO and the resulting tape properties. The pinning mechanism of YBCO coated conductors or thin films is one of the main interests of this work. YBCO thin films are some kind of “scientific” coated conductors, because they do not consist of additional buffer layers. They are widely used for research on pinning, because the superconducting layer can be traced by transmission electron microscopy (TEM). Indeed, their production is easier than in the case of coated conductors due to missing protecting shunts and layers. Untypically, the studies on pinning will be done on coated conductors in this thesis. This is a consequence of the main purpose of the neutron irradiation, which

is fusion. A complex study focused on types of pinning centres and possibilities to enhance the performance of HTS wires has been done by S.R. Foltyn et al. [10]. To achieve ideal pinning and the required performance by the manufacturing of a CC, several parameters have to be tuned.

- **Ideal YBCO thickness.** The maximal critical current of a tape is not proportional to the thickness of the YBCO layer, since the critical current density of a superconductor is usually lowered with increasing layer thickness. Therefore, finding the highest thickness with still high values of critical current densities can be crucial for applications.
- **Substrate surface decoration.** This is a procedure, where metal particles such as Ag, Ir or oxides e.g. Y_2O_3 , are processed on a substrate before the YBCO grows. The flux pinning can be enhanced in this way. The lattice planes are disordered or abrupt and pinning centres such as antiphase boundaries or dislocations are created.
- **Impurity addition.** Adding impurities into the YBCO crystallographic structure can have similar effect as the surface decoration. An yttria-stabilized zirconia (YSZ) addition is widely used. Vertical nanocolumns of $BaZrO_3$ particles can be created in the YBCO lattice, which can be effective pinning centres.
- **Rare earth elements addition or substitution** Probably the most complex pinning enhancement mechanism arises from a replacement of yttrium from the YBCO with other rare-earth elements, e.g. Ga, Pr, La, Sm. Although it has been known for a long time that the (RE)BCO compounds exhibit different and sometimes enhanced critical current densities J_c s, the mechanism is still not well understood up to now. One of the possible explanations emerges from a spatial variation of T_c .

The types of the defects present in YBCO thin films are illustrated in Figure 2.3. It is important to notice, that all those illustrated defects are responsible for extrinsic pinning. The intrinsic pinning is caused by the natural structure of YBCO, e.g. a layered structure. The critical current density (J_c) is not necessarily improved by a simple addition of new pinning centres. The J_c drops after a certain level of defect concentration is exceeded or if a special combination of the defect types is present. Some of the defects affect the J_c only in a particular magnetic field orientation. As a result, various shapes of the $J_c(\varphi)$ curve can be created, which will be investigated later on.

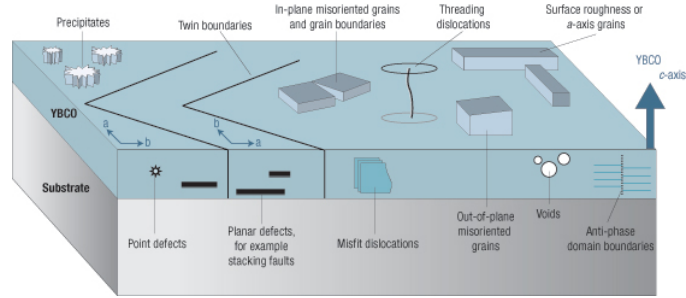


Figure 2.3: YBCO thin film defects as possible pinning centres [10].

2.2 Fabrication methods of HTS wires

2.2.1 First generation of HTS wires

Bismuth based superconductors are multifilamentary tapes, where many thin superconducting filaments are stacked together into a conducting matrix (Figure 2.4). The preferred types of superconductors for this architecture are: BSCCO-2212 ($\text{Bi}_2\text{Sr}_2\text{Ca}_1\text{Cu}_2\text{O}_8$) with a critical temperature of 95 K and BSCCO-2223 ($\text{Bi}_2\text{Sr}_2\text{Ca}_2\text{Cu}_3\text{O}_{10}$) with 108 K [11].

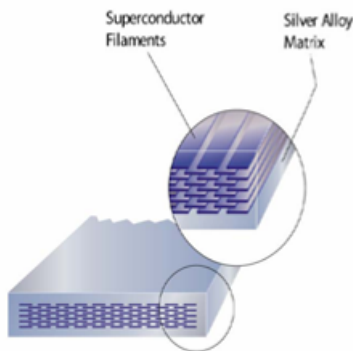


Figure 2.4: Multifilamentary BSCCO tape.

A great effort is currently being put into forming this kind of superconducting tape by the "powder in tube" method. This simple method ensures uniaxial texture of the HTS material. Tapes over a kilometer long have been made from the Bi-2223 material. The achieved critical current densities are above 10^4 A/cm^2 at 77 K. The Bi-2212 material must be kept below 20 K. However, its superconducting properties are superior at those temperatures. The "Powder in tube forming" is a rather easy and economical method to produce BSCCO tapes. BSCCO in powder form

can be heat treated and then packed tightly into a cylindrical silver billet. Cylinders of about 1 mm diameter are formed by repeated drawing of the filled tubes. A group of such cylinders - filaments are rolled together and deformed into a tape with a width of about 4 mm and a thickness less than 0.2 mm. Finally, the tape is sintered. The main problem of this type of superconductor is silver. Silver is used because of its outstanding conductive properties and softness which allows to form the tapes. However, silver is very expensive

and the softness causes rather bad mechanical properties of the tapes. Moreover, the Bi-2223 superconductor at 77 K significantly loses the superconducting properties even in lower fields. Although the world leading manufacturers up-scaled the production lengths up to kilometers of homogeneous tape, the industry with all the possible applications is focused more to the second generation of HTS tapes because of their superior properties.

2.2.2 Second generation of HTS wires

The second generation of the HTS tapes is well-known as coated conductors. In the last few years, most of the manufactures transferred the main focus into these perspective HTS tapes. The biaxial grain arrangement plays a crucial role in the manufacturing process. Although the production process is far more difficult than in case of the first tape generation, the superconducting as well as the mechanical properties are better. The production process consists of more steps because several different buffer layers have to be deposited. Each buffer layer requires a special sophisticated method of deposition, which demands high investments to the fabrication equipment. Although the absence of the massive silver shunt from the case of the first generation of HTS can save some material costs, employment of rare elements such as Y, increases the price again. Moreover, the tape must be produced fast enough, in long lengths and with certain performance and homogeneity to be commercially competitive. Therefore, the world leading manufacturers invest a lot of finances to improve manufacturing techniques. A short time after the introduction of the second generation of HTS to the market, the research was mainly focused on the J_c enhancement and the homogeneity of tapes. Later on, the main focus moved to up-scaling the tape lengths up to kilometers and the speed of the production. Here, the most common manufacturing techniques of CCs are presented. A general simplified sketch of a CC is plotted in Figure 5.21, where all the crucial buffer layers are shown. Commercial CCs have usually even more buffer layers, which improve grain arrangement, electrical contact, electrical stabilization or mechanical properties. However, every additional buffer layer increases the production cost.

Substrate The substrate is the core of every CC. It is usually a non-magnetic alloy, but some manufacturers use also magnetic materials due to lower costs. However, the magnetic substrate increases AC losses. During the fabrication process, the substrate is usually electropolished to achieve a smooth and clean surface as a prerequisite for successful addition of other buffer layers.

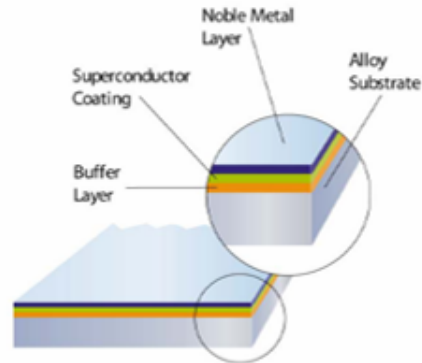


Figure 2.5: Sketch of a coated conductor.

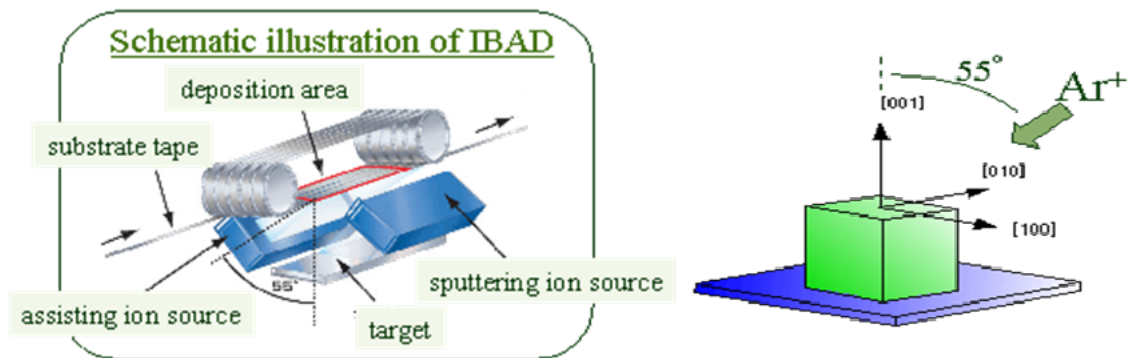


Figure 2.6: Illustration of IBAD process.

Template buffer layer The template buffer layer plays a crucial role in introducing the biaxial texture for the superconducting crystals. One of the most preferred production techniques is Ion Beam Assisted Deposition (IBAD). A simplified sketch is plotted in Figure 2.6. A highly in-plane oriented template is done by deposition of yttria stabilized zirconia (YSZ) - (EHTS, Sec. 2.3.2) or MgO (SuperPower, Sec. 2.3.1) in the presence of a well-collimated assisting ion beam. The beam is directed to the substrate at a certain angle. Then, a cap layer (often CeO_2) is epitaxially deposited. This procedure was modified and improved by Bruker (before EHTS) and denoted as ABAD (Alternating Ion Beam Assisted Deposition) [12].

The most spread alternative to the IBAD method is RABiTS (Rolling Assisted Biaxially

Textured Substrate). RABiTS is used, e.g. by American Superconductor for second generation HTS fabrication [13] (Sec. 2.3.3), due to its relative low costs and high reliability. The template is highly cube-textured as high-purity nickel and certain alloys are thermo-mechanically processed and recrystallized. The cap buffer layers are then deposited epitaxially on the RABiTS template. Other possible options are E-beam deposition, Pulsed Laser Deposition (PLD), sputtering, sol-gel, ink-jet printing etc.

Superconducting layer The superconducting layer is apparently the crucial part of every CC. Usually, an $\text{YBa}_2\text{Cu}_3\text{O}_{7-\delta}$ (YBCO) compound is used, but it can be replaced by a (RE)BCO. Still, all of them are perovskite structures (Figure 2.2). In the last few years, many different methods for the deposition of the superconducting layer were developed. A very common method is above mentioned PLD, which is schematically shown in Figure 2.7. It is a physical deposition method. Other physical deposition methods are vapor plating, Molecular Beam Epitaxy (MBE), magnetron sputtering (single direction, alternating, high frequency). The other commonly used methods are chemical methods: Metal Organic Deposition (MOD) or Metal Organic Chemical Vapor Deposition (MOCVD), spray method, plasma-spray method, salt-gel method, spray – pyrolysis, ink-jet printing. The preferred methods by world leading producers are MOD/MOCVD and PLD, because of low cost, high speed, efficiency and reliability. However, other methods may become more important after certain technical improvements, for example, where big surfaces of YBCO are needed. Ink-jet printing looks very promising in this way [14], although further development is needed. In addition, it is also possible to create other buffer layers by this method.

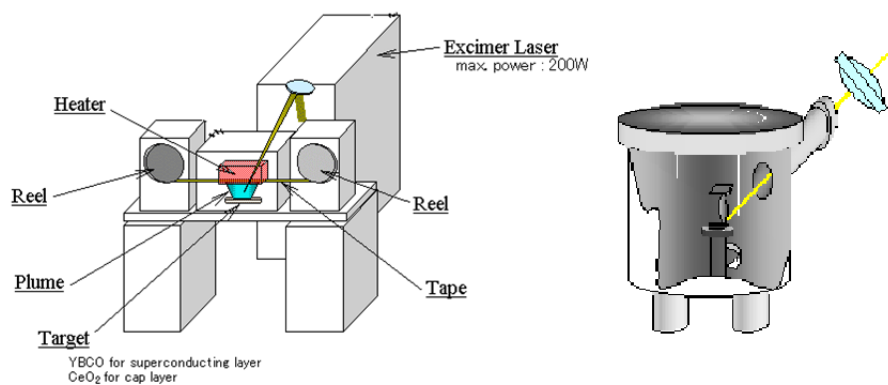


Figure 2.7: Illustration of a PLD process.

Covering layer The covering layer is supposed to provide an electrical contact and act as a tape stabilization too. Pure silver is commonly used due to its outstanding electrical properties. In comparison to the first generation HTS only a very thin layer (few μm) is used. This layer does not radically increase the production cost. Silver is usually sputtered onto the superconducting layer.

Coating layer The coating layer protects the inner layers from mechanical and also chemical damage, it works as an electrical stabilization and also provides the electrical contact. Some producers use completely surrounding coatings and the others deposit only a robust layer on the top of the tape. Depending on application, copper or stainless steel are usually used as the coating material. The thickness of the coating can be very different for different types of CCs.

2.3 Samples

All the studied coated conductors (CCs) were commercially available products from the world leading manufacturers. All the samples were characterized without any changes in structure, cross section or composition. The largest part of this thesis deals with a coated conductor from SuperPower. The other studied samples were: CC from European High Temperature Superconductor EHTS (recently Bruker), 344 CC from American Superconductor. American Superconductor CC was fully and EHTS CC partially characterized in the PhD. thesis from R. Fuger [8]. In this thesis, some results from his work will be used. Also other kinds of characterization employing different measurement techniques were done in this thesis.

2.3.1 SuperPower

SuperPower developed one of the most powerful and reliable coated conductors on the market [15]. The second generation of coated conductors is denominated as: “2G HTS SCS 4050” [16]. The tape is fully surrounded by a copper stabilizer. The substrate is non magnetic, made of high-strength Hastelloy® C-276, which results in lower ferromagnetism, AC and eddy current losses. Several MgO buffer layers made by Ion Beam Assisted Deposition (IBAD) serve as template layers to introduce the biaxial texture for the superconducting film. The YBCO layer is 1 μm thick and made of the unique Metal Organic Vapor Deposition technique (MOCVD). A thin, 2 μm thick silver layer made by a sputtering technique provides an outstanding electrical contact. The tape is 0.089 mm thick and 4 mm wide.

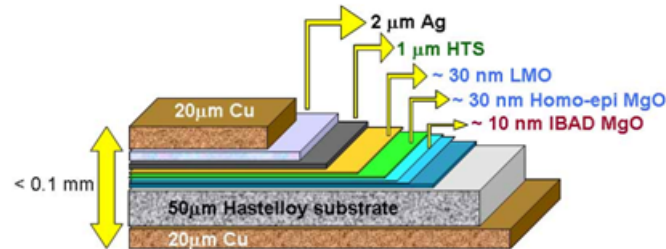


Figure 2.8: Sketch of the coated conductor from SuperPower.

Improved manufacturing methods allow to produce long lengths (kilometer class) of the conductor with very homogeneous critical currents. The parameters of the particular tape used in this work are presented in Table 2.1.

Table 2.1: Parameters of SuperPower CC.

Tape no.	SCS 4050
Width	4 mm
Length	2.2 m
Cu thickness	20+20 μm
Total thickness	89 μm
YBCO thickness	1 μm
I_c @77 K, self field (1 $\mu\text{V}/\text{cm}$)	102 A

The chemical composition of the SuperPower CC: Cobalt (Co) – 1.3% ; Chromium (Cr) – 8.2%; Copper (Cu) – 44%; Iron (Fe) – 3%; Manganese (Mn) – 0.5%; Molybdenum (Mo) – 8.2 %; Nickel (Ni) – 29%; Silicon (Si) -0.1%; Silver (Ag) - 4.3%; Tungsten (W) – 2%; Vanadium (V) -0.2%; YBCO – 1%.

2.3.2 European High Temperature Superconductors

The coated conductors consist of a stainless steel substrate, several buffer layers, an YBCO layer and a protecting layer. The substrate is highly resistant against oxygenation and is non-magnetic. The tape is stabilized by a copper layer. The excellent bonding to the coated conductor reduces the interface resistance between the Cu-layer and the HTS film. Therefore, the Cu-layer efficiently plays the role of a shunt that protects the YBCO superconductor during current overloads. The yttria-stabilized zirconia (YSZ) buffer layer

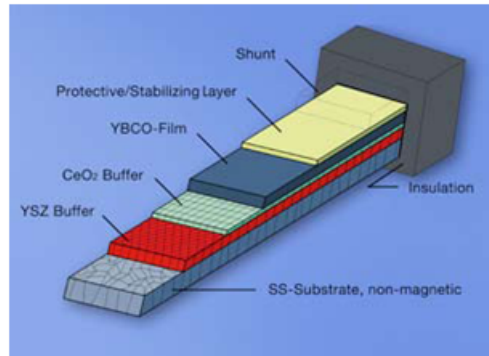


Figure 2.9: Architecture of the EHTS coated conductor.

Table 2.2: Parameters of EHTS CC.

Tape no.	555
Width	4 mm
Length	1 m
Cu thickness	17 μm
Total thickness	120 μm
YBCO thickness	2.5 μm
I_c @77 K, self field (1 $\mu\text{V}/\text{cm}$)	171 A

is deposited by an Ion Beam Assisted Deposition (IBAD) technique with a typical in-plane alignment (ϕ - scan) of 10-12° (FWHM)). An interlayer of 20-80 nm thick CeO_2 is deposited between the YSZ and the superconductor by in-situ high-rate pulsed laser deposition (HR-PLD) in order to improve the homogeneity. The same technique is used for the superconducting YBCO layer deposition. A high-rate-deposition (HR-PLD) technique increases the deposition rate and improves the homogeneity of the superconductor resulting in higher critical current densities. It was developed by EHTS (Bruker) [12]. The data sheet of the sample is shown in Table 2.2.

2.3.3 American Superconductor

American Superconductor (AMSC) is the producer of the 344 (2G) coated conductor [13]. The AMSC coated conductor also has a multi-layer architecture (Figure 2.10). This CC is based on the RABiTS™ template. This template is the basis for the textured substrate along with the metal organic deposited (MOD) YBCO layer. The substrate consists of a textured nickel tungsten alloy, then followed by three additional epitaxial buffer layers: an yttrium oxide (Y_2O_3) layer, a layer of yttrium-stabilized zirconia (YSZ)

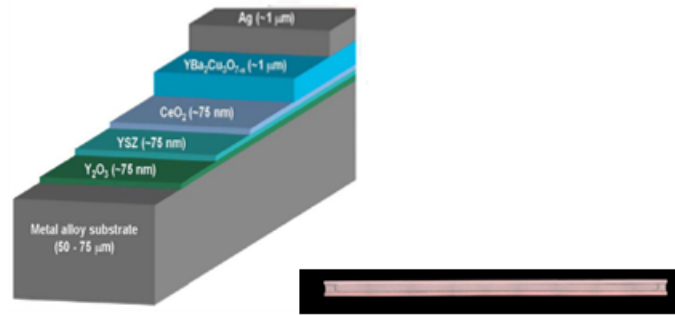


Figure 2.10: Architecture of the AMSC coated conductor (left). View on the tape with visible protection edges (right).

and a layer of ceria (CeO_2). The Ni-W alloy has a thickness of $75\ \mu\text{m}$ and forms a magnetic substrate for the tape. A $75\ \text{nm}$ thick Y_2O_3 seed layer was deposited by electron beam evaporation. Both, the YSZ barrier and the CeO_2 cap layer were subsequently deposited by rf-sputtering. Both these layers are again $75\ \text{nm}$ thick and deposited by a continuous reel-to-reel process. The superconducting layer is formed by a decomposition of chemically deposited metal-organic precursors (MOD). The resulting YBCO thickness is estimated to be $1.2\ \mu\text{m}$, measured by SEM cross-section analysis. However, Rutherford backscattering (RBS) data have shown that the mass of the film corresponds only a $1.0\ \mu\text{m}$ thick fully dense, stoichiometric film. A $3\ \mu\text{m}$ thick silver cap layer provides the electrical contact and also protects the superconductor. The tape is fully coated by a $50\ \mu\text{m}$ thick copper strip, which ensures electrical, mechanical and environmental stabilization. Since the total width of the tape is $4.4\ \text{mm}$ and the superconducting layer is only $4\ \text{mm}$ wide, the remaining $\sim 0.2\ \text{mm}$ on the edges work like a corrosion protection and electrical stabilization. Due to the relatively low number of buffer layers and easier manufacturing techniques this tape has lower production costs and hence a much more competitive market price. The sample parameters are listed in Table 2.3.

Table 2.3: Parameters of AMSC CC.

Tape no.	344
Width	4.4 mm
Length	20 m pieces
Cu thickness	50 μm
Total thickness	0.18- 0.22 mm
YBCO thickness	$\sim 1 \mu\text{m}$
I_c @77 K, self field ($1\mu\text{V}/\text{cm}$)	70 A

2.4 Superconductors for fusion magnets

The applicability of HTS as a primary material in fusion magnets is presently not possible although it would be desirable to use HTS in future fusion reactors, e.g. DEMO and beyond. The main purpose of the HTS is to use them either at high magnetic fields, e.g. 20 T, or at high operation temperatures e.g. 64 - 77 K. The second option would drastically reduce the requirements for cooling and, therefore, a huge amount of energy could be saved. A suitable HTS wire for fusion should be selected according to these properties [17]:

1. High engineering current density in the conductor at a specific temperature and magnetic field.
2. Sufficient mechanical strength or option for reinforcement.
3. Tolerable hotspot and quench behavior.
4. Optimized current distribution, i.e. feasibility of good joints and optimized inter-strand resistance and inductance.
5. Possibilities to limit the AC losses.
6. Compatibility of coolant choice, e.g., nitrogen, helium, neon or hydrogen.
7. Tolerable activation due to neutron irradiation.

High engineering current density in the conductor at a specific temperature and magnetic field. A high performance of the HTS wires is an essential condition for fusion applications. Since high neutron fluences are present during operation, the issue of their influence on the critical current density in the HTS wires must be taken into account.

Detailed studies on selected CCs dealing with this topic are one of the issues of this work and will be presented later. Regarding the fusion applications, an even more important parameter than the critical current density is the overall engineering critical current density of the wire, which is indeed influenced by the neutron fluxes. The engineering critical current density depends on the amount of the electrical stabilizer, the architecture of the wire, the space for coolant within the cable and also other materials used in all the buffer layers of the conductor. The engineering critical current density has to be high enough to generate the desired field with a tolerable number of windings. The number of windings is important for the magnet inductance: in case of a fast discharge, a high voltage, which might be critical, arises.

Sufficient mechanical strength or option for reinforcement. The performance of the superconductor is reduced under a high mechanical strain. In the case of a high field operation, the Lorentz force may cause massive problems for the materials. In the YBCO or BISCO wires, cracks or other hot spots, which will drastically limit the current density could be created.

Tolerable hotspot and quench behavior. In case of a quench, where superconductivity is locally lost, the coil current will deposit a large amount of energy due to ohmic heating at this place. If a fast discharge of the coil is triggered, the conductor has to withstand the energy deposition until the coil is discharged completely. Therefore, good stabilization is essential.

Optimized current distribution, e.g. feasibility of good joints and optimized inter-strand resistance and inductance. Very good joints of superconductor-superconductor in the scale of few nOhm are essential. Otherwise the generated heat at the joint might create a hot spot under high currents.

Possibilities to limit the AC losses AC losses in HTS conductors are presently one of the most discussed topics. AC losses are present in all type II superconductors during changes in the transport current. Especially, they are critical for the classical Tokamak design that uses the field ramping of the central solenoid to drive the plasma current. A great achievement would be to limit the coupling and eddy current losses to the level of the hysteresis losses. A great and simple solution to reduce the AC losses is twisting of the parallel superconducting wires. However, it is not a simple problem with unflexible HTS materials as coated conductors. A promising solution lies in the ROEBEL cable [18] (Figure 2.11).

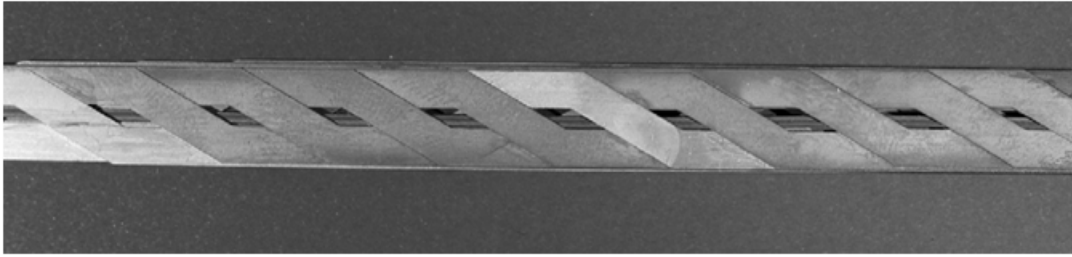


Figure 2.11: View of the 16 strand ROEBEL assembled coated conductor [17].

Compatibility of coolant choice, e.g., nitrogen, helium, neon or hydrogen. Usually, there are no difficulties in this point. The most important is the chemical stability of all the conductor components to the coolant. Therefore, rare gasses such as helium and neon are very desirable.

Tolerable degradation and activation of materials due to neutron flux. In the ideal case, the assembled superconducting devices should remain in operation without any limitation during the whole life time of the fusion reactor. For this reason, it is necessary to test superconductors up to neutron fluences corresponding to the whole reactor lifetime and beyond. Another important issue is the activation of the materials. A too high activation and corresponding high level of radiation might make it impossible to make even small services on the superconducting and any devices close to them. Therefore, the preferred materials are those, which produce mainly short lived nuclides.

3 Irradiation

3.1 TRIGA Mark II Reactor

The TRIGA Mark II reactor in Vienna is a pool type research reactor that is used for training, research and isotope production (TRIGA - Training, Research, Isotope production, General Atomic) [19]. The reactor has a maximum continuous thermal power of 250 kW, though the power can be increased up to 250 MW for about 40 ms in the pulse regime. The center fuel temperature is about 200 °C. The reactor core consists of 80 fuel elements (3.75 cm in diameter and 72.24 cm in length), which are arranged in an annular lattice (Figure 3.1). The fuel is in the form of a uniform mixture of 8 wt% uranium, 1 wt% hydrogen and 91 wt% zirconium, where the zirconium-hydride is being the main moderator. This fuel mixture is covered by a fuel rod cladding. The maximum neutron flux density of $10^{17} \text{ m}^{-2}\text{s}^{-1}$ at 250 kW is reached in the ZBR (Central Irradiation Facility).

The reactor is controlled by three control rods which contain boron carbide as absorber material. When these rods are fully inserted into the reactor core, the reactor remains sub-critical. For the chain reaction initialization, a start-up neutron source (Sb-Be photoneutron source) is present in the reactor core. If the absorber rods are withdrawn from the core, the number of fissions in the core and the power level are sequentially increasing. The reactor can be shut-down either manually or automatically by the safety system. It takes about 0.1 s for the control rods to fall into the core. In accordance with its purpose as a research reactor, the TRIGA Mark II is equipped with a number of irradiation devices: 5 reflector irradiation tubes, 1 central irradiation tube, 1 pneumatic transfer system (transfer time 3 s), 1 fast pneumatic transfer system (transfer time 20 ms), 4 neutron beam holes, 1 thermal column, 1 neutron radiography facility. In this thesis, the central irradiation facility was used for most of the irradiation procedures. The reflector irradiation tube was employed for some experiments as well. The sample temperature in both cases is estimated to remain below 50 °C during the irradiation process. The neutron fluxes at maximal reactor power in both irradiation facilities are shown in Table 3.1.

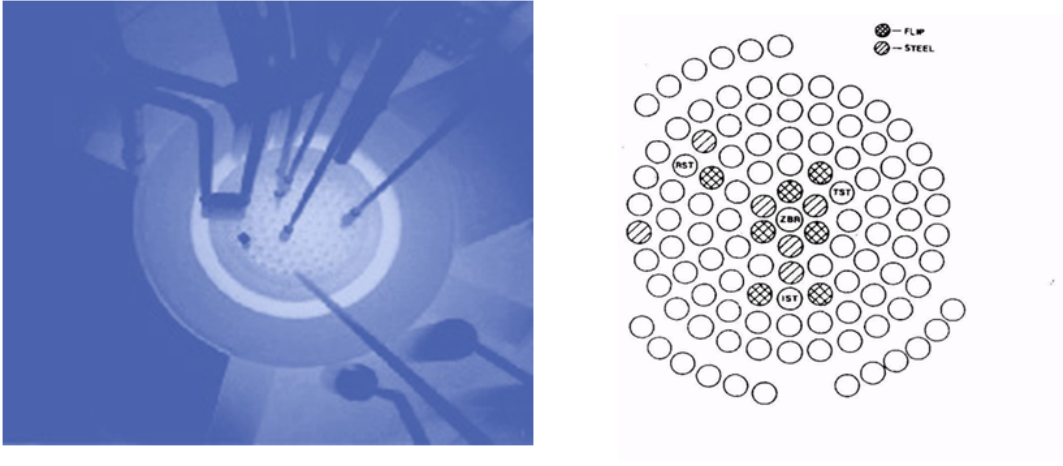


Figure 3.1: Reactor core and the core configuration of the TRIGA Mark II reactor.

Table 3.1: Neutron fluxes in the TRIGA Mark II reactor.

250 kW	Thermal neutrons $E < 0.55 \text{ eV}$	Fast neutrons $E > 0.1 \text{ MeV}$
ZBR [19]	$6.1 \times 10^{16} \text{ m}^{-2} \cdot \text{s}^{-1}$	$7.6 \times 10^{16} \text{ m}^{-2} \cdot \text{s}^{-1}$
Ref. irr. tube [20]	$1.73 \times 10^{16} \text{ m}^{-2} \cdot \text{s}^{-1}$	$4 \times 10^{15} \text{ m}^{-2} \cdot \text{s}^{-1}$

3.2 Neutron interaction with matter

Neutrons cannot interact by electromagnetic interactions. Therefore, the only one way of an effective interaction occurring is with a nucleus. The classification of neutron interactions with matter is not unified. Different literature sources present different classifications. In the next sections, the classification taken from [23] is presented, where the elastic scattering was not considered as a nuclear reaction. It is the only case, where the nucleus remains unchanged and unexcited. Inelastic scattering is considered as a kind of nuclear reaction. The nuclear reactions are classified in Sec. 3.2.2.

In solids, the effect of elastic or inelastic collisions is emphasized. If the target nucleus receives a momentum from the incident neutron, it is able to produce further displacements before being slowed down. The target nucleus composition remains unchanged in this process (except (n; 2n) reactions, Sec. 3.2.2). If the nucleus is excited, it can be de-excited either during deceleration or when it stops. In superconductors, elastic and inelastic scattering are the most interesting, as they mainly influence the changes of the superconducting properties. In the case of the other nuclear reactions, the neutron is captured by the target nucleus and a subsequent interaction occurs. If the reaction is exothermic and the cross section high enough for low energy neutrons, atomic displacements can be made, even by thermal neutrons, which usually do not have enough energy to generate defects in direct collisions [22]. An example of such an exothermic reaction is the fusion blanket reaction: ${}^6\text{Li} (n; \alpha) {}^3\text{H}$. In this case, the cross section increases as $1/\sqrt{E_n}$ with decreasing neutron energy.

3.2.1 Elastic scattering

A sketch of an elastic scattering is shown in Figure 3.2.

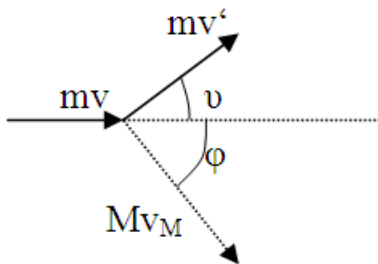


Figure 3.2: Sketch of elastic scattering, m - particle mass, M - nucleus mass, ν - scattering angle.

The laws of kinetic energy and momentum conservation are valid in the case of elastic scattering:

$$\frac{1}{2}mv^2 = \frac{1}{2}mv'^2 + \frac{1}{2}Mv_M^2 \quad (3.1)$$

$$m\vec{v} = mv'\vec{v}' + Mv_M\vec{v}_M. \quad (3.2)$$

All parameters are described in Figure 3.2. In superconductors, the kinetic energy $\frac{1}{2}Mv_M^2$ is the source for lattice defects formation.

3.2.2 Nuclear reactions



Eq. 3.3 is a general formula for nuclear reactions, where $a = n$ - neutron, A - target nucleus with $b+B...$ being the products. The nuclear reactions cause changes within the nucleus of the atom, but do not influence directly the crystal lattice. They cause changes in the isotope and element composition of the superconducting layer and other buffer layers in CCs. The radioactivity of a neutron irradiated sample is a clear evidence of this kind of interactions.

The capture of neutrons proceeds through a compound nucleus, A^* , which is an isotope of the element A : $n + A \rightarrow A^* \rightarrow b + B...$. The excitation energy of the compound nucleus, A^* , is equivalent to the kinetic energy of the absorbed neutron. The lifetime of A^* is usually in a range of $10^{-20} - 10^{-12}$ s. Metastable states of A^* , so called isomers, are special cases and their lifetime can be even a couple of years.

The classification of nuclear reactions with respect to the b particle:

Inelastic scattering ((n; n'), (n; n, γ), (n; 2n)) The law of kinetic energy conservation is not valid. The nucleus A is after the collision in an excited and unstable state A^* , which is a strong argument to consider inelastic scattering as a nuclear reaction. The classification of the (n; 2n) reactions in this group is debatable, however it is often reported in literature [23].

Radioactive capture (n; γ) By probability one of the most common nuclear reactions, present also at low and very low energy neutrons (thermal neutrons). The formed compound nucleus, A^* , emits only a gamma photon. In other words, the product nucleus is

an isotope of the same element as the original nucleus. The mass number is increased by one.

Transmutation ((n; p), (n; d), (n; α)) A nucleus may absorb a neutron forming a compound nucleus, A^* , which is later de-energized by emitting a charged particle, either a proton (p) or a deuteron (d) or an alpha particle (α). This produces nuclei of different elements.

Fission (n; f) This is a type of reaction, where the compound nucleus is separated into two or more fission products, $B...$, and the escaping particle, b , (Eq. 3.3).

Nucleus collapse The nucleus collapses into elementary particles or several different structures. This type of reaction may occur at very high energies of the primary neutrons ($E_n > 100$ MeV).

3.3 Coated conductors in fission and fusion reactors

If coated conductors are irradiated, all parts of the wire have to withstand the same neutron fluences, which occurs across the sample. The neutron spectrum in the ZBR irradiation facility of the TRIGA Mark II reactor is rather vast (Table 3.1). Therefore almost all of the presented neutron interactions from Sec. 3.2.2 are possible (although nucleus collapse is probably very sparse). It is important to notice that apart from single crystals where pure YBCO was irradiated, coated conductors consist of several additional layers which irradiation may influence. The main influence will be probably the mechanical weakening of the material, although detailed studies have not yet been done on this topic. However the impact of neutron irradiation on the superconducting properties coming from other buffer layers in the CC are investigated in this thesis.

3.3.1 Isotope effect

The superconducting properties may be changed by the substitution of another isotope in the lattice. This dependence is a consequence of BCS theory and has been proven by many experiments. The equation

$$T_c \sim M^{1/2} \tag{3.4}$$

describes the change of the critical temperature of the superconductor with the mass of the lattice atom. The isotope effect has also been studied in YBCO. It is already well established, that the oxygen isotope effect is rather small in optimally doped cuprates

(highest T_c), but larger in the underdoped ones [21]. ^{16}O was replaced by ^{18}O in those experiments. Studies on the copper isotope effect were also performed and the conclusions are very similar to the oxygen ones. The ^{63}Cu was replaced by the heavier isotope ^{65}Cu . The isotope effect was pronounced again in the underdoped samples by a reduction of T_c of up to 0.7 K [24]. Although this effect disappeared or was even reversed in the optimally doped YBCO. For future applications of coated conductors in fusion power plants, the T_c of the superconductors operating in the coils might be reduced because of the isotope effect. However, the isotope effect is rather weak even by complete replacement of one isotope for the other [21, 24]. By irradiation, only a very small amount of different isotopes will be produced ($\ll 1\%$), which cannot have any effect on the T_c . Therefore, the isotope effect is negligible and does not need to be considered.

3.3.2 Lattice defects

Lattice defects are the most important effect caused by any type of irradiation on superconductors. Introduced lattice defects can locally depress the superconducting order parameter and pin the magnetic flux vortices. During the irradiation process, an incoming particle of certain energy collides with a target atom (Y, Ba, Cu or O) producing primary knock-on atoms (PKA). A PKA is able to produce defects, if its energy exceeds the threshold energy for a permanent displacement (E_d). Typical values of E_d for solids are 15 - 40 eV [6]. The primary defect is usually considered to be a vacant lattice and an interstitial atom. The final defect can consist of clusters of point defects, if the vacancy or the interstitial atom are mobile enough. In the case of high energy particles, mainly heavier ones such as neutrons or protons, the primary displacement atom can produce even several hundreds of secondary displacements together with a certain amount of energy, which is released as heat. The energy of the primary atoms is uniformly distributed from zero to the maximum, which occurs in a head-on collision. As reported by many authors in numerous publications, the defects caused by fast neutrons ($E > 0.1$ MeV) are big enough to be effective pinning centres and can enhance J_c of superconductors [7, 25]. Defects in the nanometer range are usually effective pinning centres in HTS at higher temperatures, although in the HTS material also smaller point - pinning centres can be effective [7]. Fast neutrons can cause defects in the HTS lattice of up to few nm in size. Penetrating neutrons interact with atoms in the lattice and create a cascade. Due to the emerged heat, the surrounding material melts and creates a spherical defect object of amorphous material of up to a few nanometers (usually 1- 5 nm) in size. Later on a recrystallization may occur, however the new crystal grows in different conditions, which results in a different GL parameter = pinning centre. The GL parameter is decreased also

due to possible high angle grain boundaries or an ab plane misalignment of the crystal. Point - defects can be introduced by less energetic neutrons as well and usually these are able to move within the superconductor. Thermal neutrons do not have enough energy to displace atoms from the lattice.

As was presented above in Sec. 3.1, the temperatures at the irradiation facilities of the TRIGA reactor are about 50°C. Therefore, all the irradiations were performed at those temperatures, despite the fact that in a fusion machine the superconductors must withstand fluences at the operating temperature of the superconducting magnets. It is well known that irradiation at higher temperatures causes less defects than at lower temperatures. The main reason for this is due to lattice recovery caused by temperature oscillations. Most of the literature from this area deals with solid materials, e.g. semiconductors and metals, and not with superconductors. Therefore, the major part of these published results deal with temperature ranges from 400 K and above, e.g. H. Ohyama et al. [26], which is far from the operating temperature of any superconductor. Nevertheless, for any solid material the difference in the neutron induced damage is interesting mainly close to the melting point. More accurately, the “differential of the neutron damage function” is steep close to, but almost flat far below the melting point. The melting point of YBCO is >1000 °C, which is high enough to assume no significant changes between ~323 K (~50 °C) and 77 K or 64 K (~-196°C, ~-209 °C). Despite significant technical difficulties, some neutron irradiation experiments at low temperatures have been performed. H. P. Wiesinger et al. [27] irradiated an YBCO single crystal in the low-temperature irradiation facility (TTB) of the FRM reactor in Munich. The results of this experiment demonstrate that the irradiation leads to a large enhancement of the critical current densities in YBCO, which are comparable to results obtained under standard irradiation conditions (~50 °C). The main differences were found in the T_c . The annealing to room temperature led to a recovery of T_c by 1 K of the radiation-induced depression, which was estimated to be 3 K. This behavior is attributed to oxygen reordering. However, the superconducting parts of a fusion reactor will be also heated up to room temperature at some points during the reactor life time.

The experiment of Wiesinger brought also another important outcome. The radiation-induced enhancement of the J_c , which amounted up to 2500% (at 5 K and 4 T), decreased by only ~20% after annealing. Thus the majority of the defects responsible for pinning remain stable during the annealing treatment. It is an evidence, that the collision cascades and the larger point defect clusters play the most important role for the radiation-induced flux pinning enhancements.

3.3.3 Secondary radiation from created isotopes

It is well known that only neutrons above a certain energy will lead to defects, which can be effective pinning centres. Nevertheless, most of the studies were done on single crystals [7]. The important difference between single crystals and CCs lies in the layered structure of the CCs (2.3). These buffer layers can be activated by (mainly thermal) neutrons and emit secondary α , β and γ radiation. As was mentioned in Sec. 3.3.2, any particle of certain energy can displace an atom from the crystal lattice. Neutrons are very effective due to the absence of energy loss by ionization. However, other types of radiation (e.g. deuterons, protons [28]) can be also effective in the production of pinning sites. An exemplary comparison of the displacement pairs produced by different types of radiation is presented in Figure 3.3. The figure shows, that electrons of energies close to E_d produce only the simplest vacancy pattern consisting of isolated, randomly distributed vacancy-interstitial pairs. Heavy charged particles as deuterons produce small groups of pairs, whereas fast neutrons can produce large groups containing several hundreds of pairs (clusters of point defects). Indeed, fast neutrons can produce also large defects as was described in Sec. 3.3.2. The γ radiation is not relevant, since only very small changes in the superconducting properties were observed [29]. The situation is different for β radiation, which was studied on YBCO single crystals and reported by J. Giapintzakis et al. [30]. According to their studies, the threshold minimal energy of the β particles for producing pinning centres is between 400 and 600 keV. These values can be derived, if the threshold energy (E_d) of 20 eV is considered for Y, Ba, Cu or O atoms and assuming a simple relativistic version of the particle scattering equation (from Eq. 3.1, Eq. 3.2):

$$E_M = \frac{2ME_m(E_m + 2mc^2)}{(m + M)^2c^2 + 2ME_m} \quad (3.5)$$

Thus the calculated threshold electron energies needed for Y, Ba, Cu, O displacement are: 532 , 730, 413, 129 keV, respectively. The secondary electrons do not have problems to penetrate the superconducting layer, since the direct contact is present between the other buffer layers with the YBCO layer.

Thermal neutron irradiation of the SuperPower coated conductor To demonstrate the relevance of β radiation for the introduction of pinning centres, the following experiment has been performed. A sample from SuperPower was irradiated in the reflector irradiation facility to a thermal neutron fluence of $7 \times 10^{20} \text{ m}^{-2}$. Potential β emitters in the tape are listed in Table 3.2. Angular resolved transport measurements were performed. These will be discussed in detail in Sec. 5.1. The resulting $J_c(\varphi)$ curve is compared to the $J_c(\varphi)$

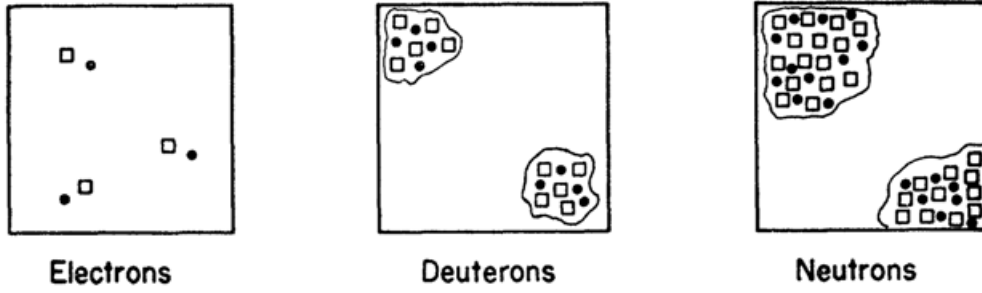


Figure 3.3: Diagram showing the displacement pairs caused by electrons near E_d , deuterons well above E_d and neutrons [6].

Table 3.2: Maximum energy of β particles of selected isotopes.

Isotope	Max. Energy (keV)	Probability per decay
Ag 110m	530	0.305
W 187	626.7	0.587
	1312.5	0.251
	687	0.055
	694.1	0.035
Co 58	475 (positron)	0.201

measured on the pristine sample and to the $J_c(\varphi)$ measured on a sample irradiated to a fast neutron fluence of $2 \times 10^{21} \text{ m}^{-2}$ (Figure 3.4). No real influence on the sample irradiated by thermal neutrons is observed comparing to the pristine sample. However the influence of fast neutrons is remarkable.

Based on calculations, the fluence of β radiation in the SuperPower sample (26 mm long) is estimated to be $10^{13} \text{ m}^{-2} - 10^{15} \text{ m}^{-2}$ (resulting from a thermal neutrons fluence of $7 \times 10^{20} \text{ m}^{-2}$). At the same time, the fast neutron fluence in the reflector irradiation tube corresponds to $1.63 \times 10^{20} \text{ m}^{-2}$. This rather small fast neutron fluence is significantly higher than the expected β fluence, which would make it hard to distinguish contributions from these two influences. Moreover, due to the β decay character (neutrino with variable energy emission), many β particles have even lower energies than is shown in Table 3.2. Thus the expected effective fluence of β particles is too low to create enough effective pinning centres. Later on (Chapter 6) will be also shown that the point defects do not influence the critical current densities in CC. As a conclusion, the final effect of the secondary radiation in the SuperPower CC was evaluated as negligible.

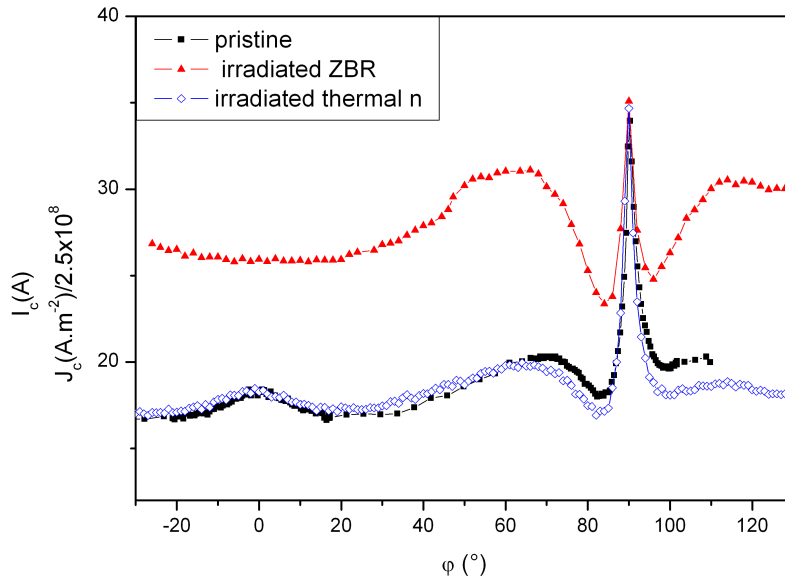


Figure 3.4: J_c of a SuperPower tape at 64 K, 6 T, unirradiated, irradiated by fast neutrons, irradiated by thermal neutrons.

3.4 Irradiation in a fission reactor for fusion applications

As was mentioned before, fast neutrons are not the only particles present in the irradiation facilities of the TRIGA Mark II reactor. However, the situation is different in fusion power plants where the slow or thermal neutrons are present only in very small amounts, where the superconducting magnets are located. Estimated neutron energy spectra of fusion reactors (magnet location) in comparison with spectra in the TRIGA Mark II reactor (ZBR) and in the Intense Pulsed Neutron Source (IPNS, Chicago) are presented in Figure 3.5. It is not clear from the figure, that the TRIGA Mark II reactor is suitable as an irradiation facility for testing superconductors for fusion magnets. The average fluence is about 4 orders of magnitude higher and this difference is considerably enlarged at lower energies. However, higher fluences can be a great advantage in irradiation experiments because of shorter irradiation times. The whole ITER lifetime fluence at the magnet location is estimated to be $1 \times 10^{22} \text{ m}^{-2}$ fast neutrons [31]. This fluence can be reached in the ZBR irradiation facility in 36.55 hours. The inhomogeneous distribution of neutrons with different energies may pose a more serious problem due to the presence of high fluences of thermal neutrons. However, resulting from the work of F.M. Sauerzopf et al. [7] and the

conclusions presented in the previous section (Sec. 3.3.3), thermal neutrons do not affect the J_c of CCs. Another issue concerning different temperatures during the irradiation in the fission reactor and during actual operation in the fusion device was discussed in Sec. 3.3.2. The observed difference was considered to be negligible as well and not affecting the properties of the CCs. Finally, it can be concluded that the Central Irradiation Facility (ZBR) of the TRIGA Mark II reactor in Vienna is suitable for test irradiation of CCs as possible candidates for fusion magnet applications.

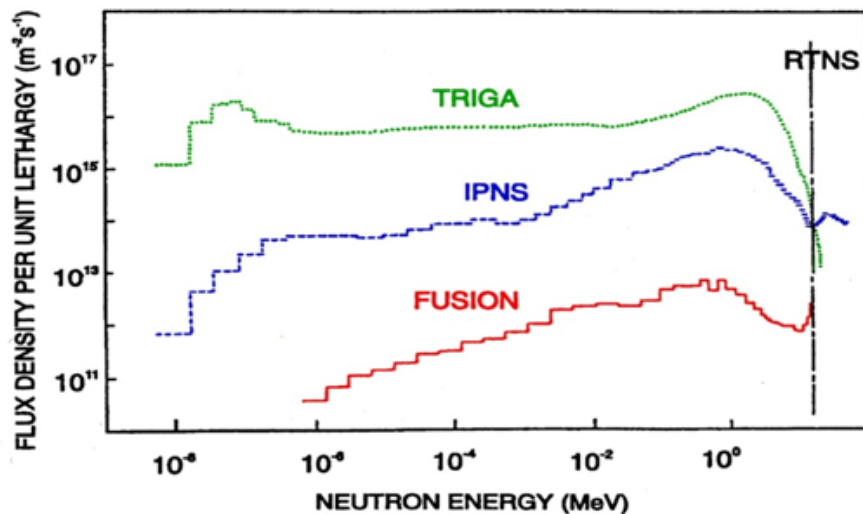


Figure 3.5: Comparison of neutron energy spectra from different sources.

3.5 Irradiation procedure and analysis

Beside the positive effect of neutron irradiation on CCs - introduction of additional pinning centres - a negative effect is also present, which is the activation of elements. Studies on the flux pinning enhancement are presented in the next chapters. As was already mentioned, the activation of the elements is an inconvenient side effect that completely disqualifies the use of this otherwise effective way of pinning enhancement for most real applications. The only real use of irradiation is connected to academic research on pinning or application in facilities such as fusion reactors. The irradiation of CCs in this work has been done for both those reasons.

The irradiation procedure started by sealing samples into quartz glass. The sealed quartz glass tube with the samples inside was inserted into an aluminum capsule, which had been designed to be plugged into the ZBR. The irradiation took between 7.31 and 36.55 hours, which corresponds to fast neutron fluences of $2 \times 10^{21} \text{ m}^{-2}$ and $1 \times 10^{22} \text{ m}^{-2}$.

The samples were irradiated and measured after reaching fluences of: $2 \times 10^{21} \text{ m}^{-2}$, $4 \times 10^{21} \text{ m}^{-2}$, $1 \times 10^{22} \text{ m}^{-2}$ and $1.3 \times 10^{22} \text{ m}^{-2}$ with respective irradiation times: 7.31 h, 14.62 h, 36.55 h and 47.51 h. The usual activity of the samples just after the irradiation is up to several mSv/h. Fortunately, most of the radiation comes from short and very short lived nuclides whose activity is significantly reduced after a couple of days. During the decay time, the capsule with the samples was kept in the reactor pool, though out of the core. As the maximum allowed radioactivity for the sample handling was set to 1 mSv/h (close geometry - distance less than 1 cm), it was necessary to wait a certain time until the activity decreased below this value. Expected activities, which had been calculated before the irradiation procedure, were in a good agreement with the values obtained by measuring the samples after irradiation. Gamma spectra of both sample types irradiated for the purpose of this work (EHTS, SuperPower) are shown in Figure 3.6.

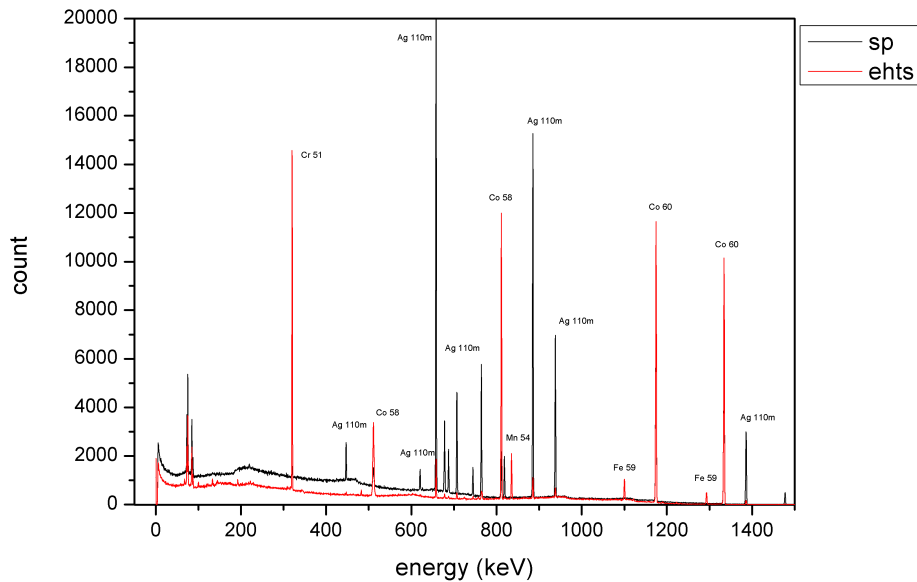


Figure 3.6: Gama spectra of SuperPower and EHTS CCs measured about 6 months after irradiation.

The SuperPower sample with removed copper coating and the silver shunt shows a very different gamma spectrum than the regular one (Figure 3.7). The irradiation time was 30 min in the reflector irradiation tube and the gamma spectrum was measured about 24 h later. Irradiation doses from both previous samples are not comparable with this one due to different irradiation times and irradiation facilities used. However, the major radiation

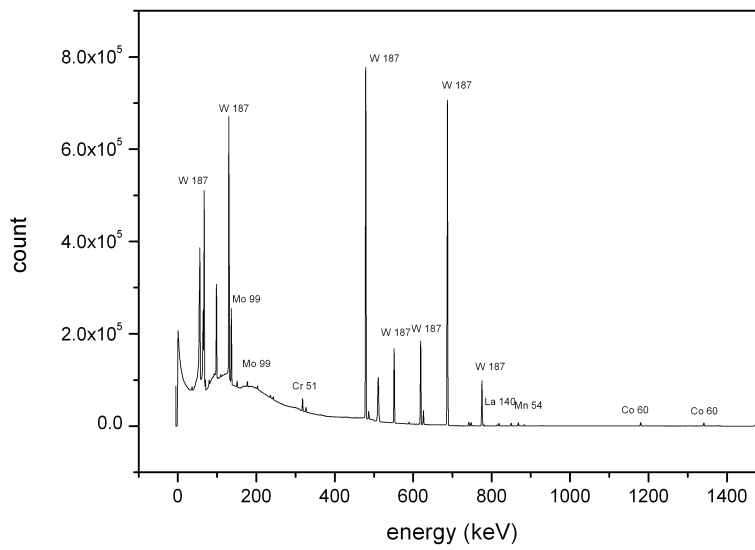


Figure 3.7: Gamma spectrum of the SuperPower CC with removed copper coating and silver layer.

is coming from ^{137}W , which is not present in Figure 3.6. It is a clear evidence, that the main part of the radiation is coming from the silver shunt and the radiation of the YBCO and buffer layers of the SuperPower CC is very small.

4 Methods and Instrumentation

4.1 Transport Measurements

A direct transport measurement is the simplest method of investigation of superconducting wires. Three different set-ups in Vienna and one in the laboratory of Applied Superconductivity and Cryoscience Group at the University of Cambridge were used. All devices were adjusted to measure CCs without any special sample preparation methods such as etching or patterning. All measurement devices can measure samples of uniform size, which usually was ~ 4 mm width and 26 mm long. The standard 4 - point technique (Figure 4.1) was employed. The samples were mounted on special sample holders and connected according to Figure 4.1. Special sample holders for each device will be introduced in the next sections. Indium press current contacts proved to be most suitable. A thin indium foil was pressed between the sample and the current leads to reduce the mechanical load on the sample and to achieve minimal resistance. The soldered contacts have generally very good electrical properties. However, the heat generated by soldering can degrade the HTS in the tape and cleaning the sample is rather complicated, which could cause problems in the subsequent irradiation process. The wires of the voltage contacts (C, D) were connected to the tape with a special silver paste. The default distance L between the contacts was 3 mm. The voltage wires must be twisted and shielded to reduce possible noise. Small resistivity of the wire is vital as the measured voltages are usually in the nano - to millivolt range.

Cernox temperature sensors were used for temperature measurements in helium gas flow cryostats. A temperature measurement is crucial due to the temperature variations

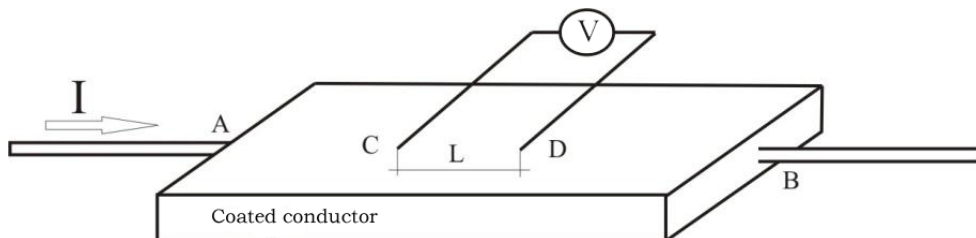


Figure 4.1: Experimental arrangement for the standard 4 - point technique.

in the VTI (Variable Temperature Insert). A good thermal contact was ensured between the sample and the sensor temperature. Therefore, the temperature was monitored very carefully and longer holding times after temperature changes were kept. While measuring under ramping temperatures, the ramp rate was chosen to be small enough to ensure minimal gradients and the sample was always close to the thermal equilibrium. In cases of measurements in a liquid coolant, e.g. liquid nitrogen, a very precise temperature measurement is not necessary. Therefore, another cheaper and less precise type of temperature sensor was used.

4.1.1 Critical currents (I_c), Critical current densities (J_c)

The main output from a characterization of superconductors are these two quantities. The macroscopic critical current I_c (end-to-end critical current) is most relevant for applications of superconducting wires and cables. The critical current of the entire conductor is defined by the smallest local critical current along the whole tape. The critical current density J_c is usually used in theoretical studies, because it represents a general property of the superconducting substance. The relation between those two quantities is defined by:

$$J_c = \frac{I_c}{A_{sup}} \quad (4.1)$$

$$J_e = \frac{I_c}{A_w} \quad (4.2)$$

where A_{sup} denotes the cross-section of the superconducting layer and A_w the cross section of the whole wire. J_e is the engineering critical current density, which is an important parameter of every cable or tape. Measurements are executed by a continuous ramping of the current until an abort criterion (defined voltage) is reached. The criterion must be chosen very carefully. If the criterion is too low, the current-voltage curve (I-V curve) will not contain enough information. On the other hand, if the criterion is too high, the sample can be damaged or completely destroyed. This criterion has never been chosen above 6 mV, which corresponds to ~ 0.2 mV/cm between the C, D contacts (Figure 4.1).

Many criteria are used for I_c . A voltage criterion was used in this work and it was set to 1 μ V/cm for all the measurements. This criterion has no real theoretical background. It was chosen purely empirically for the convenience in the evaluation. An important attribute of the criterion is a value well above the noise, but not too far from the zero resistance phase. The I-V curve close to the transition to the normal phase obeys the law:

$$E = E_c \left(\frac{I}{I_c} \right)^n \propto I^n \quad (4.3)$$

Every measured I-V curve was interpolated by Eq. 4.3. Thus, I_c was determined from this interpolation. The exponent n , which is a free parameter in the iterations, is an important characteristic value of superconductors denoted simply as *n-value*. The interpolated I-V curve is shown in Figure 4.2. The figure shows that Eq. 4.3 describes well the I-V characteristic close to the transition.

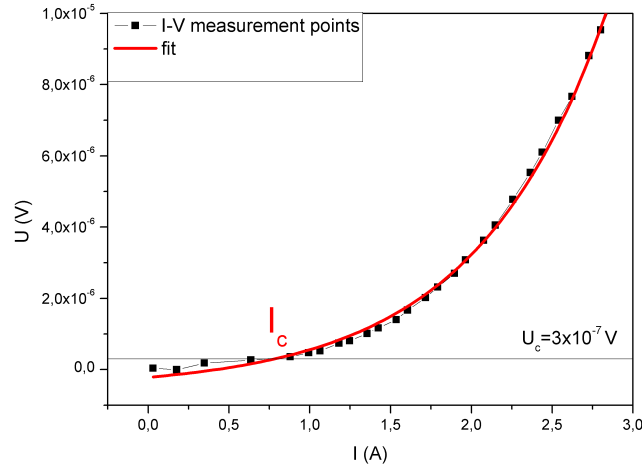


Figure 4.2: Example of I-V curve of transport measurements together with the fit. The measurements are done at high field close to B_{c2} . The *n-value* is rather low.

4.1.2 Critical Temperature

The critical temperature was determined by the resistivity method. The same setting, as shown in Figure 4.1, was employed. The transport current was not ramped up, but a stable very small current was constantly flowing through the sample when the temperature was slowly decreased. The current was chosen very small (10 mA) in order to avoid heat production. The transition occurred, when zero (offset) voltage was measured. The voltage was constantly measured in fixed intervals. A relay was employed in the current circuit, which allowed to change the polarity of the current. Then every experimental point was evaluated on the basis of two voltage measurements with different current polarities. Thus the voltage with the offset correction

$$V = \frac{V^+ - V^-}{2} \quad (4.4)$$

was easy to calculate.

A generally used critical temperature criterion does not exist. This is the reason why it

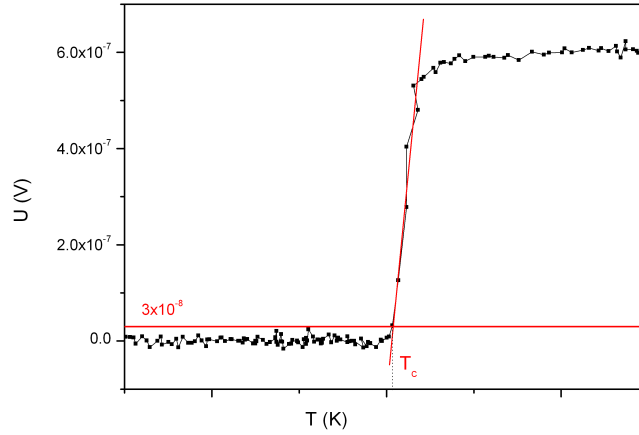


Figure 4.3: Critical temperature criterion.

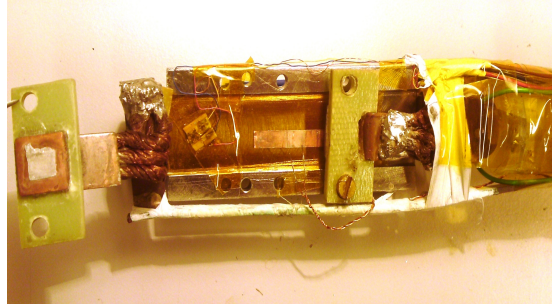
is important to define a special criterion for each paper. This thesis deals with superconductors for applications, where it is important to keep wires in the zero resistance mode. Therefore the criterion that was used is rather strict, $V_c = 0.1 \mu\text{V}/\text{cm}$. Figure 4.3 shows the critical temperature criterion definition.

4.1.3 The electromagnet set-up

The electromagnet set-up was employed for angular resolved transport measurements. This set-up disposes of a 1.4 T water cooled electromagnet. As a cryostat, a simple tube-shaped vacuum vessel (flask) is used. The sample holder is statically mounted between the magnet poles. A change of magnetic field direction is then caused by the rotation of the magnet poles. The whole magnet body is then placed on a cross band with a precise rotation mechanism. The maximal rotation range is up to 200° and the maximal angular resolution is 0.5° . The angular resolved transport measurements using a regular sample holder are possible only in the maximal Lorentz force configuration (Sec. 5.1.1). The sample holder is equipped with a temperature sensor and also a Hall probe was added for some special measurements. The standard indium press contacts were used to transport the current through the sample. Voltage contacts are glued to the sample surface by a conductive silver glue.



(a) View on the rotating magnet and the cryostat.



(b) Detail on the sample holder.

Figure 4.4: Electromagnet set-up.

4.1.4 6 T set-up

The 6 T set-up (Figure 4.5a) is a gas flow cryostat equipped with a 6 T split coil. Horizontal magnetic fields allow to provide angular resolved transport measurements with a rotating sample holder so that the principle of measurement is identical to that in the electromagnet set-up. The simple rotating sample holder (Figure 4.5b) can be replaced by a 2-axis probe sample holder which is equipped with an additional stepper motor and the sample can also be tilted. However, the 2-axis probe is not suitable for characterization of CCs as it is built for low transport currents up to 5 A.

The single axis rotating sample holder is equipped with a sensitive Hall probe, a Cernox temperature sensor and with a rotating mechanism with the stepper motor. Current contacts are typically indium press contacts and the conductive silver glue is used for the voltage contacts as before. The maximal possible angular resolution of measurements is below 0.05° . The mounted CC sample is presented in Figure 4.5b. The standard 26 mm long and 4 mm wide samples of the CCs were used. A 170 A current source is available in this set-up.



(a) View on the 6 T measurement set-up



(b) Mounted sample on the single axis sample holder.

Figure 4.5: 6 T measurement set up and the sample holder used

4.1.5 17 T set-up

The 17 T set-up is a helium flow cryostat. This machine is equipped with a 17 T superconducting coil, which generates a magnetic field in vertical direction. The VTI has a radius of about 3 cm and the magnetic field is homogeneous in a vertical length of about 3 cm. These parameters limit the maximum samples lengths to 26 mm. The sample holders, built specially for the CCs, allowed to provide transport measurements in the field parallel to the ab plane or the c -axis (Figure 4.6). Both sample holders were adapted for indium press current contacts and the voltage wires were mounted by conductive silver glue. A Cernox temperature sensor was employed. A powerful 300 A current source was available for the transport characterization.



(a) $H//c$.



(b) $H//ab$.

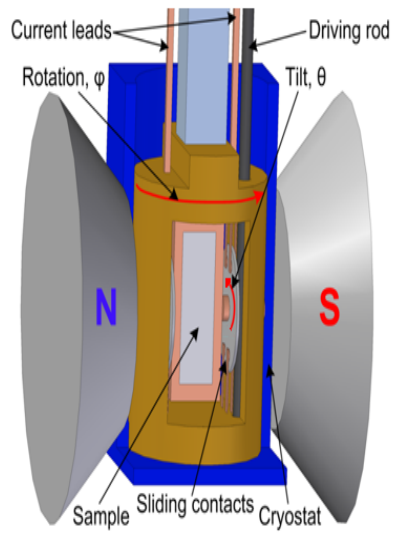
Figure 4.6: Sample holders used in 17 T set-up.

4.1.6 2-axis high current goniometer

Since parts of the construction and the initial measurements of this set-up have been performed as a part of this PhD work, special attention will be paid for a detailed description of this set-up. The 2-axis high current goniometer (ASCG Cambridge, Figure 4.7) is designed for the characterization of superconducting tapes - CCs of up to 14 mm wide with sample lengths of up to 30 mm. The standard 4 - point technique is employed for transport measurements. This device is equipped with a sample holder with multiple sprung current contacts (Figures 4.7b, 4.8b) and large - diameter current leads allowing transport currents up to ~ 200 A to be applied routinely, which are significantly higher than in commonly used goniometers [32, 33]. The connections were developed especially for the characterization of CCs with very high critical currents. The sample holder body is massive in order to provide better temperature stability. High currents in this range are needed for characterization of full - width commercial tapes without etching or other destructive sample preparation. The sample current contacts are soldered with indium at temperatures below 250 °C to minimize possible degradations of the superconducting layer of CCs. The sample holder is equipped with 2 perpendicular Hall probes, allowing the direction of the magnetic field to be verified for every sample orientation in rotation and tilt. The orientation is controlled using stepper motors (Figure 4.8b), geared to achieve a step size of $\sim 0.005^\circ$ and delivering a positional accuracy of $\sim 0.1^\circ$ with zero position repeatability of $\sim 0.5^\circ$. For the work reported here, a full 360° rotational scan range was available and 110° in tilt. All measurements were made in liquid nitrogen with a maximum external magnetic field of 0.5 T generated by a water-cooled electromagnet. The simple cryostat for liquid nitrogen used here can readily be replaced by a helium flow cryostat if required.



(a) Experimental set-up in the ASCG laboratory.

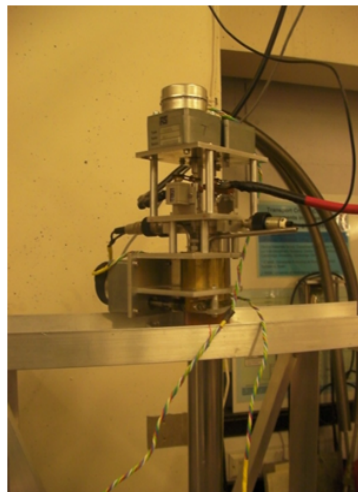


(b) Schematic sketch.

Figure 4.7: 2-axis high current goniometer (ASCG Cambridge).



(a) Detailed view on the massive sample holder .



(b) Detailed view on the stepper mechanism.

Figure 4.8: Parts of the 2-axis high current goniometer.

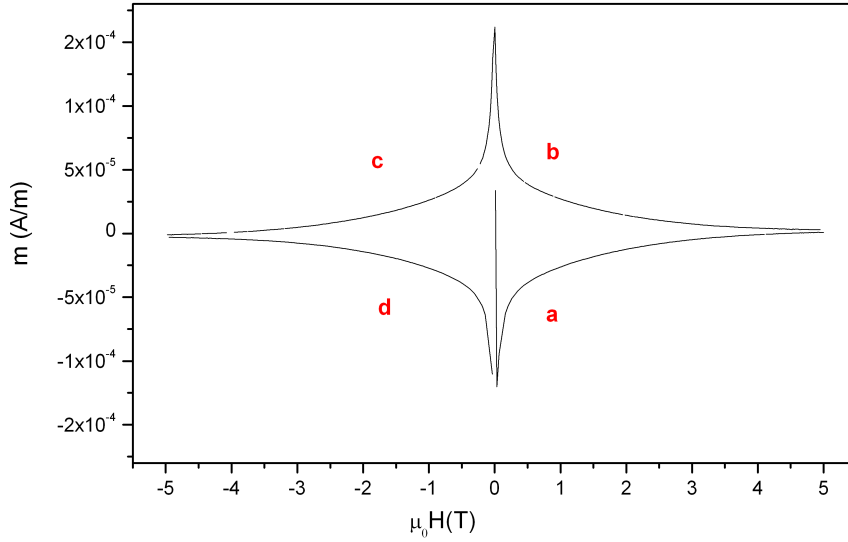


Figure 4.9: Magnetisation loop from VSM.

4.2 Magnetization measurements

4.2.1 The Bean model

To derive a critical current density J_c from the irreversible magnetization the Bean model [35] is widely used due to its simplicity and good approximation to the real J_c . The expression

$$J_c(B) = \frac{J_{c,0}}{(B + B_0)^\eta} \quad (4.5)$$

is widely used to express the relation between three parameters $(J_{c,0}, B_0, \eta)$. In the Bean model, η is equal to zero, which means

$$J_c(B) = \text{constant}. \quad (4.6)$$

Eq. 4.6 describes the particular properties of the irreversible magnetisation for an infinitely long cylinder. Boundary conditions must be considered for real samples. An example of the irreversible magnetisation dependence is shown in Figure 4.9. The irreversible magnetic moment m_i can be calculated from any two neighboring lines.

$$m_i = \frac{-m(a) + m(b)}{2} = \frac{m(b) + m(c)}{2} = \frac{m(c) - m(d)}{2} = \frac{-m(d) - m(a)}{2} \quad (4.7)$$

The Bean model assumes a constant J_c in the whole sample. This can be a good approximation for CCs, when the field is in the c direction and the currents are within ab planes. Then the total magnetic moment is a result of simple integration:

$$\vec{m}_i = \frac{1}{2} \int d^3r \vec{r} \times \vec{J}_c. \quad (4.8)$$

The result for a rectangular sample with a volume $\Omega = a \times b \times c$, ($a \geq b$) is

$$J_c(H) = \frac{|m_i(H)|}{\Omega} \cdot \frac{4}{b(1 - \frac{b}{3a})}. \quad (4.9)$$

However, one is rather interested in $J_c(B)$ than $J_c(H)$. The procedure is done by numerical integration and successive iterations and is fully described in [36]. The $J_c(B)$ evaluation has always been done along the b and c curves (Figure 4.9) in this work. For integration and the transformation of $J_c(H)$ to $J_c(B)$, a special software has been used.

4.2.2 Vibrating Sample Magnetometer (VSM)

The MagLab VSM from Oxford Instruments [34] was employed for all magnetic measurements. The set-up allows magnetization measurements at up to 5 T in the temperature range from 1.5 K to 350 K. The set-up is equipped with a measurement head (vibrator, amplifier and position motor), pick-up coils and the 5 T coil with horizontal field. The cryostat itself consists of a helium reservoir, nitrogen reservoir, vacuum chambers and the VTI. The VTI controls the temperature in the sample space by heating the helium gas coming from the helium bath regulated by a needle valve. A schematic sketch of the set-up is shown in Figure 4.10. The sample oscillates typically with an amplitude between 0.1 – 1.5 mm at a frequency of 55 Hz. The samples are mounted on a rigid rod, made of a material which produces negligible background signal. This sample holding rod can be rotated over 720 ° and moved vertically to find the central position between the pick-up coils. The magnet consists of several coaxial solenoid sections made from NbTi wire. The maximum sweep ramp of the magnet is 0.6 T/min. The oscillation of a sample with a magnetic moment induces a voltage in the pick up coils. This voltage is defined by $U = \partial_t \phi$, which is derived from the Maxwell–Faraday equation. The resulting voltage is a function of the the magnetic moment of the sample. The induced voltage is used to determine the magnetic moment of the sample as a function of the applied magnetic field. The Bean model is used to determine the J_c s.

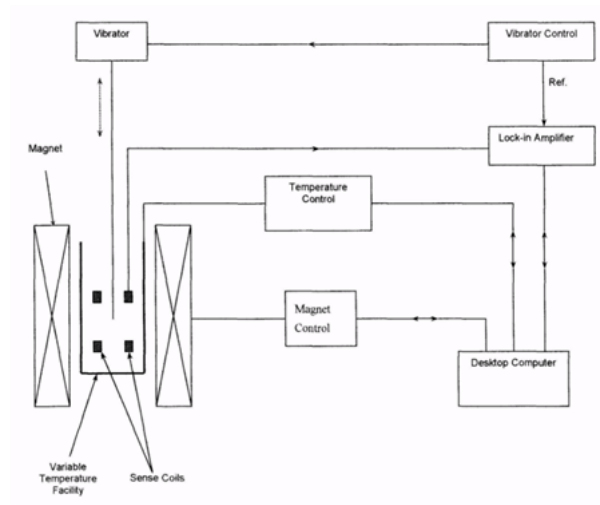


Figure 4.10: Sketch of the VSM set-up [34].

5 Measurements

5.1 Angular resolved measurements - anisotropy studies

The J_c anisotropy at varying orientations of the external magnetic field is a typical property of high temperature superconductors. This interesting phenomenon is caused by the perovskite crystallographic structure. This structure is layered and the supercurrent flows in the ab planes (Figure 2.2). Although the material is superconducting in the c -axis direction as well, the critical current densities are higher within ab planes. The spaces between particular ab planes act as effective pinning centres in the case, where the external magnetic field is parallel to the ab planes. Therefore, the ideal high temperature superconductor without any defects would have a significantly higher critical current in the case of this magnetic field orientation. Fortunately, all thin films contain numerous lattice or other defects, which may be effective pinning sites. Understanding the microscopic mechanisms behind the flux pinning in the HTS tapes is essential for the design of optimal superconducting wires suitable for various applications, it is also interesting from the scientific - theoretical point of view. The angular dependence of the critical current density - $J_c(\varphi)$ is an important parameter describing the pinning landscape of thin films. Therefore, this kind of measurements was an issue of great interest in the last few years.

5.1.1 Maximal Lorentz force characterization

In the context of the angular resolved measurements on HTS tapes, one usually understands angular measurements at the maximal Lorentz force configuration (Figure 5.1). A simple goniometer with a single rotational axis in a magnetic field can be used for this type of measurements. The resulting output is the critical current density J_c (or critical current I_c) as a function of the angle φ of the applied external magnetic field, $J_c(\varphi)$. A typical $J_c(\varphi)$ dependence of the YBCO tape is presented in Figure 5.2. Two peaks can be recognized on the $J_c(\varphi)$ curve: c -axis peak (about $\varphi = 0^\circ$) and an ab peak (at about $\varphi = 90^\circ$). The ab peak is more pronounced and is partially caused by intrinsic pinning. The c -axis peak is caused by extrinsic pinning, probably by columnar defects in the c -axis direction. The electronic mass anisotropy of YBCO together with random pinning is de-

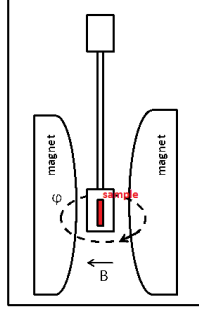


Figure 5.1: Sketch of measurements at maximal Lorentz force configuration.

scribed by the red line in the figure. This line is a result of the anisotropic scaling approach [37] and will be discussed together with the pinning character of the samples later on (Sec. 6.1.1). It has been observed, that the shape of the $J_c(\varphi)$ curve strongly depends on the film microstructure. Every type of engineering defects adds one or several features to the $J_c(\varphi)$ dependence. For example: adding a non-superconducting second phase like BZO nanorods aligned along the c -axis direction can induce a broad c -axis peak [38] which can be even higher than the ab peak; replacing the Y atoms in the crystallographic structure by other rare earth elements changes the shape of the $J_c(\varphi)$ (Figure 5.3); the shape of $J_c(\varphi)$ for undoped samples varies with the density of the columnar pinning sites [39], different types of irradiation, e.g. irradiation by heavy ions leads to columnar pinning centres enhancing the $J_c(\varphi)$ in a certain field direction [40], adding BaMO_3 ($M = \text{Zr}, \text{Sn}, \text{Ir}, \text{etc.}$) inclusions form film penetrating rods with a diameter of a few nm [38]. Numerous other studies have been done on the topics of pinning (or the J_c) enhancement and the results were often reported as angular resolved measurements in the maximal Lorentz force configuration. Looking at Figure 5.2, the important message is that strong columnar pinning centres in the c -axis direction produce a broad c -axis peak. Then the isotropic pinning sites, e.g. BZO nanoparticles, change the overall shape of the $J_c(\varphi)$ curve, but do not produce a c -axis peak.

5.1.2 Anisotropy at 77 K

Although the angular resolved measurements show J_c values in wide angular ranges, the main attention is always paid to the two main orientations of the external magnetic field. The main positions are: $H//c$ and $H//ab$ and their angular positions are $\varphi = 0^\circ$, $\varphi = 90^\circ$. However, those positions are not always correct. Sometimes, as will be presented in the next sections, the ab planes are misaligned from the tape surface, resulting in a shift in

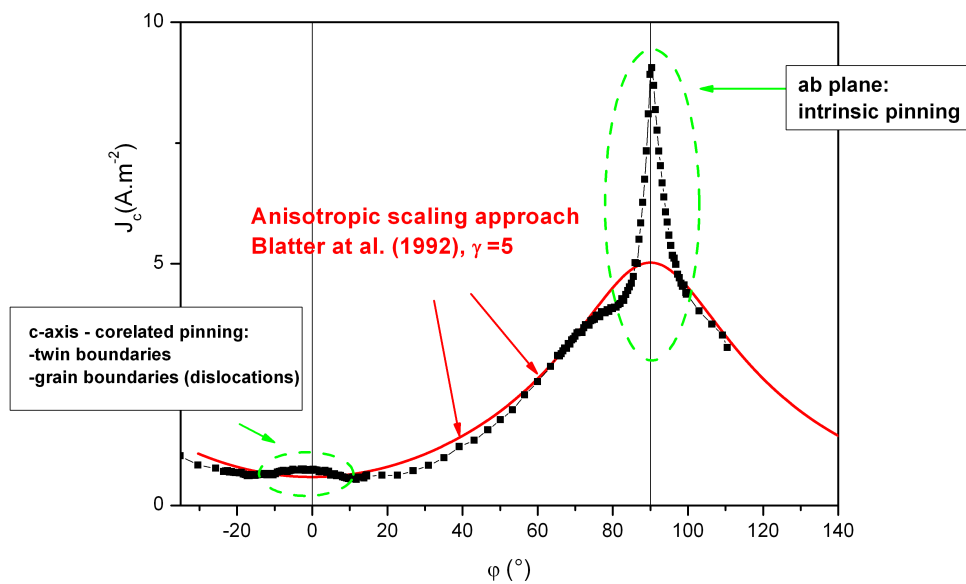


Figure 5.2: $J_c(\phi)$ of a real sample – black dots, electronic mass anisotropy of YBCO- red line.

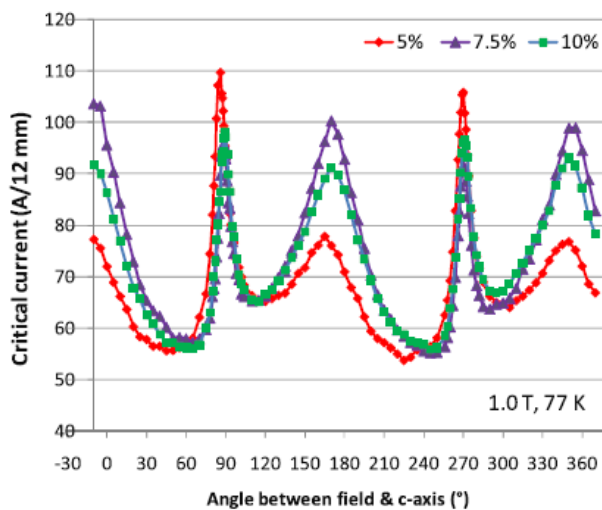


Figure 5.3: Angular dependence of the critical current at 77 K, 1 T of (Gd,Y)BCO tapes with 5%, 7.5%, and 10% Zr [41].

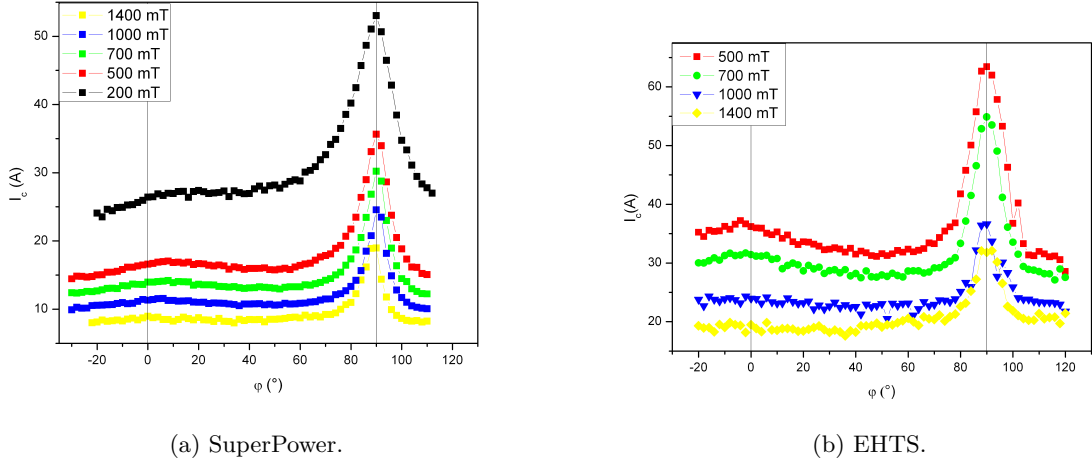


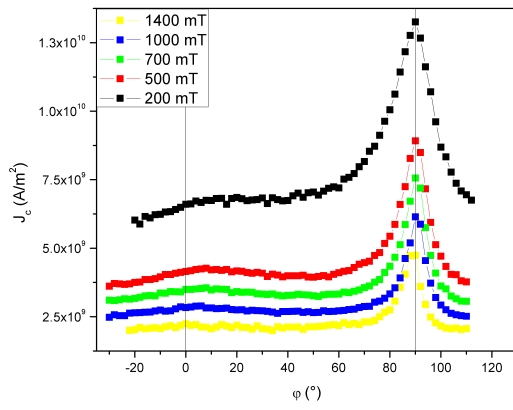
Figure 5.4: $I_c(\varphi)$ - Angular resolved measurements in liquid nitrogen – 77 K, a) SuperPower b) EHTS.

Table 5.1: Anisotropy factors from Figure 5.4.

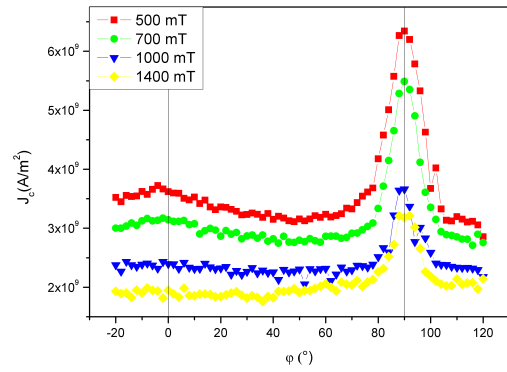
	200mT		500mT		700mT		1000mT		1400mT	
	$\frac{J_c(H\parallel ab)}{J_c(H\parallel c)}$	$\frac{J_c^{max}}{J_c^{min}}$								
SuperPower	2.01	2.01	2.15	2.26	2.16	2.32	2.17	2.34	2.11	2.37
EHTS	N/A	N/A	1.76	2.04	1.75	1.97	1.53	1.65	1.64	1.73

the $H\parallel c$ and $H\parallel ab$ positions by a few degrees backwards or forwards (usually 2° - 3°). For simplicity, the measurements at $\varphi = 0^\circ$, $\varphi = 90^\circ$ will further be denoted by $H\parallel c$ and $H\parallel ab$ if the precise position is not important to the content.

The results of this thesis will be plotted for two different physical quantities: current in Amperes, current density in A/m^2 . These two options alternate depending on the plot message, though both are often present. In Figure 5.4 the $I_c(\varphi)$ s measured on two different CCs are shown. A Hall probe was not employed in these measurements. Hence the reference angle $\varphi = 90^\circ$ was defined by the top of the ab peak. The differences in the critical currents of the CCs are caused by the different thickness of the YBCO layer. The next figure (Figure 5.5) shows the same measurement in critical current densities. The comparison together with the AMSC CC is presented in the next series of plots (Figure 5.6). The anisotropy factor is an important attribute of a tape. It can be understood as a quantity of anisotropy for the YBCO CCs. They were determined from the ratio of the measured currents between the fields parallel to the ab plane and parallel to the c -axis and between the maximum current and the minimum current. (Table 5.1)

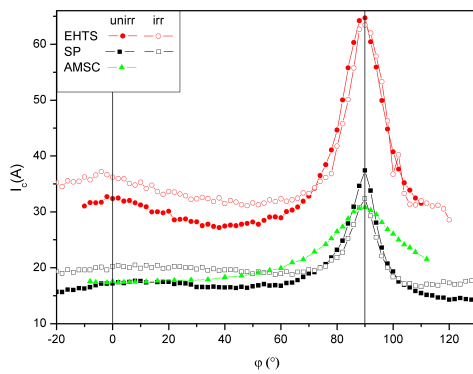


(a) SuperPower.

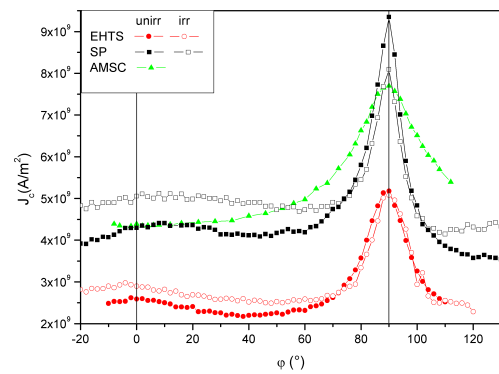


(b) EHTS.

Figure 5.5: $J_c(\varphi)$ - Angular resolved measurements in liquid nitrogen – 77 K.



(a) $I_c(\varphi)$.



(b) $J_c(\varphi)$.

Figure 5.6: Coated conductors, comparisons of the $I_c(\varphi)$ and $J_c(\varphi)$.

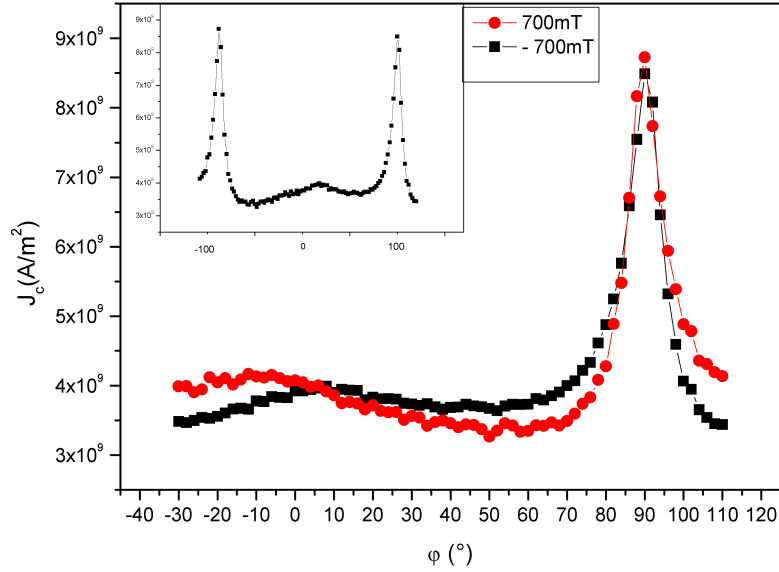


Figure 5.7: Angular dependence of $J_c(\varphi)$. The angular scale refers to the sample surface. The tape was measured twice, once in field of 700 mT and then in the reversed field. The insert represents both measurements on a single angular scale covering 220°.

The SuperPower tape shows no $J_c(\varphi)$ symmetry with respect to any vertical axis (both peaks are asymmetric). The evidence of this asymmetry is presented Figure 5.7, where the same tape was measured in two opposite directions of the magnetic field and the resulting curves are not uniform. It means the period of the $J_c(\varphi)$ function is not 90° but 180°. Similar measurements on the EHTS tape show the same effects, but they are much reduced. The AMSC CC is symmetric. Table 5.2 shows the comparison of the anisotropy factors from the measurements at reversed magnetic fields of +/- 700 mT.

The biggest advantage of the measurements in a liquid coolant such as liquid nitrogen is the possibility of measurements at low external magnetic fields, where the critical currents

Table 5.2: Anisotropy factors from Figure 5.7.

	$\frac{J_c(H ab)}{J_c(H c)}$	$\frac{J_c^{max}}{J_c^{min}}$
700mT	2.15	2.67
-700mT	2.16	2.32

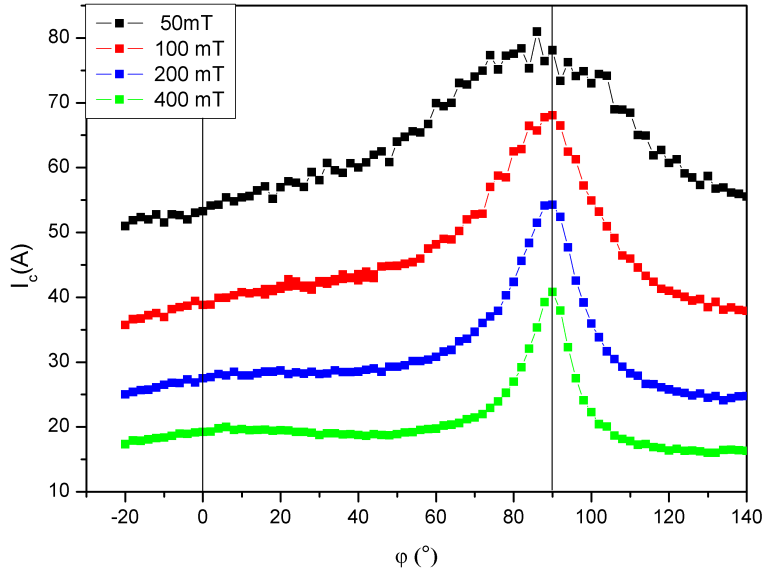


Figure 5.8: Angular resolved measurements at low fields, 77 K, Super Power.

are high. The liquid nitrogen is a very effective coolant, which assures powerful cooling also when high transport currents are measured. The measurements at low fields (from 50 mT up to 400 mT) on the SuperPower CC are plotted in Figure 5.8. The low fields are interesting mainly for transformer applications. The changes in the shape are quite noticeable. The anisotropy at 50 mT is considerably decreased (coefficient $(J_c(H//ab))/(J_c(H//c)) = 1.56$) compared to that at 400 mT (coefficient $(J_c(H//ab))/(J_c(H//c)) = 2.13$). At lower fields the c -axis peak is less and less pronounced and at 50 mT completely absent. The ab peak seems to be moving towards the c -axis, but the angular resolution at this measurement is too low to observe this change precisely. However, this shift is the motivation for the investigations in the next sections.

5.1.3 Anisotropy of the SuperPower CC

As described in the previous section (Sec. 5.1.2), the angular resolved measurements on the Super Power tape do not show the expected $\phi = 0^\circ$ - axis symmetry (Figure 5.7). The same behavior was observed by Y. Chen et al. [42] or B. Maiorov et al. [43], where doping by BZO nanoparticles or tilting the YBCO ab plane off from the tape surface can cause a similar effect. In Z. Chen's work [44], the ab planes were slightly tilted and additionally the second phase precipitates were tilted from the MgO template too. The resulting effect,

beside the already mentioned asymmetry, was that the ab peak was placed a few degrees off from $\varphi = 90^\circ$. The other observed phenomenon was a “shift” of this ab peak by the varying magnetic field. At higher magnetic fields ($> \sim 400$ mT), the ab peak was situated at the position corresponding to the misalignment angle between the tape surface and the ab planes. However, the ab peak was changing its location at low fields and was moving towards the c -axis peak. When the field was increased, this effect disappeared and the peak stayed stable. This field was rather low (200 mT - 400 mT) and possibly, it is a threshold field from grain limited current to grain boundary limited current. A possible explanation of this ab peak shift was given by Silhanek et al. [45]: it is caused by a misalignment between the externally applied magnetic field H and the internal field B . The effective correlated pinning centres might be tilted either. Granularity effects may be considered as a cause too [46, 47].

In the next experiments, the origin of the $J_c(\varphi)$ angular asymmetry was investigated. The mentioned tilt between the YBCO ab planes and the other buffer layers of the CC is the strongest candidate for the observed effect. The investigation was performed in 2 ways: first, regular anisotropy measurements were done, however the angular resolution was assessed and the angular position was interpreted by a sensitive Hall probe, which was mounted on the sample holder parallel to the sample surface. Second, X-Ray Diffraction (XRD) investigations were performed.

5.1.3.1 X-ray diffraction (XRD)

The possible misalignment angle between the ab planes of the YBCO layer and the other buffer layers was investigated in Cambridge by XRD ¹. The XRD is a method of determining the arrangement of atoms within crystals, in which a beam of X-rays strikes a crystal and diffracts into specific directions. The X-rays are then detected and from the intensity it is possible to determine the positions of the atoms in the lattice, their chemical bonds, disorder and other information. It is possible to investigate the alignment of the YBCO grains in thin films with this method as well. Therefore, the following experiments were performed to investigate the ab plane alignment within the YBCO layer of the SuperPower CC. The Figure 5.9 is a simple schematic plot of a XRD measurement set – up. The sample is mounted on the sample table, which can be rotated in Φ and also Ψ direction. Two different methods were employed to investigate the vicinality of the tape: rocking curves (Figure 5.11) were done in $\Phi = 0^\circ, 90^\circ, 180^\circ, 270^\circ$ (the sample is parallel to the X-ray beam at 0°). If we know the source angle position ω , for example for the 005 reflection $\omega = 38.42^\circ$, the maximal intensity should be detected at an angle of $\omega/2$, when

¹special thanks to Marcus Weigand

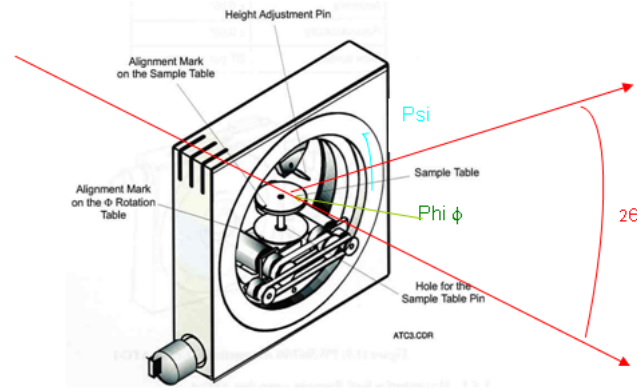


Figure 5.9: XRD measurement set-up.

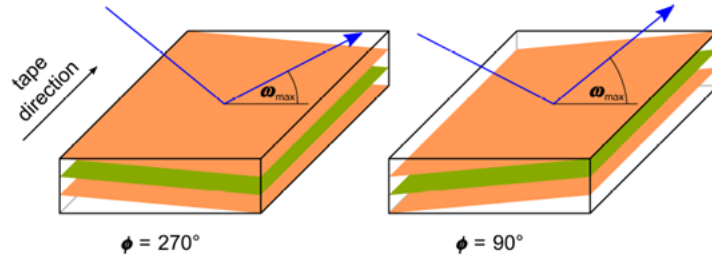


Figure 5.10: Difference of the X-ray diffraction for different sample misalignment angles.

the ab planes are well aligned. If the sample is vicinal (Figure 5.10), the maximum will be shifted to higher or lower values. The vicinal angle will then be estimated as half of the offsets measured at $\Phi = 90^\circ$ together with $\Phi = 270^\circ$ (Figure 5.11). The second method is a Ψ angular scan at $\Phi = 90^\circ$. The result is shown in Figure 5.12. A well aligned sample should show the maximum intensity at $\Psi = 0^\circ$, which is not the case. The peak is fitted by the Gauss interpolation (Figure 5.12– red line) and the maximum is estimated at $\Psi = -1.9^\circ$, which corresponds to the misalignment angle between the YBCO ab planes and the sample surface. This result is consistent with the first experiment of rocking curves, where the resulting misalignment angle $\alpha \sim 1.8^\circ$. Both experiments show a misalignment angle $\alpha = 1.8^\circ$ - 1.9° between the YBCO ab planes and the sample surface.

5.1.3.2 Anisotropy measurements

In the previous section (Sec. 5.1.3.1), the vicinity of the SuperPower tape was investigated by the XRD method. The angular resolved transport measurements were performed

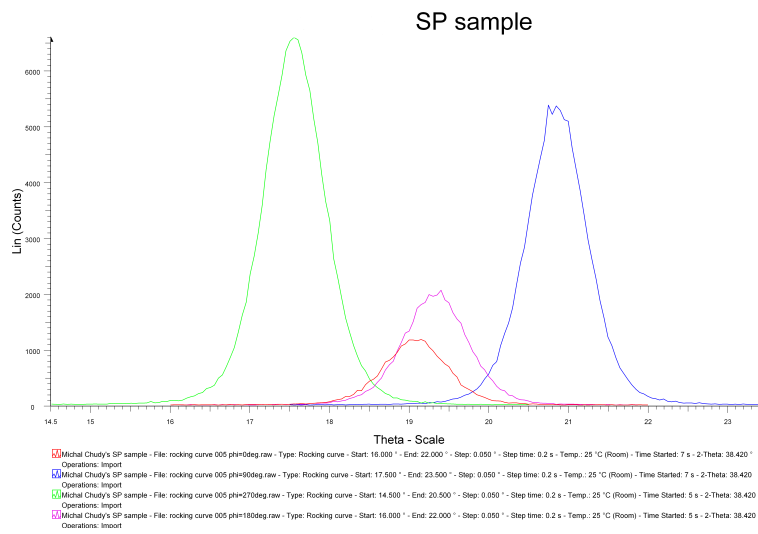


Figure 5.11: Rocking curves for the 005 diffraction (0°, 90°, 180°, 270°).

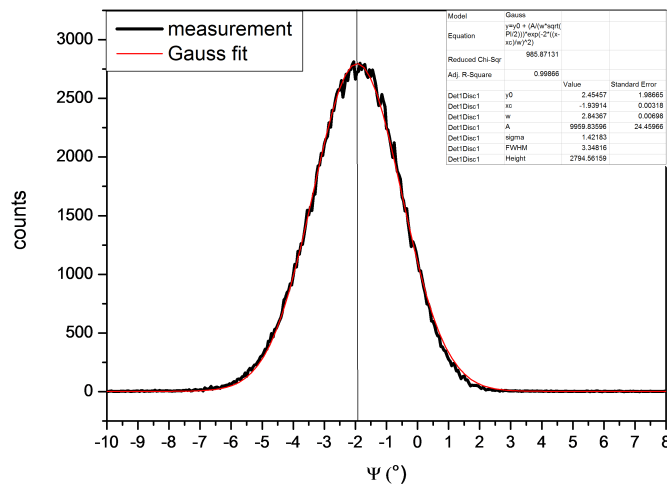


Figure 5.12: Ψ angular scan measurement with a Gauss fit (red line).

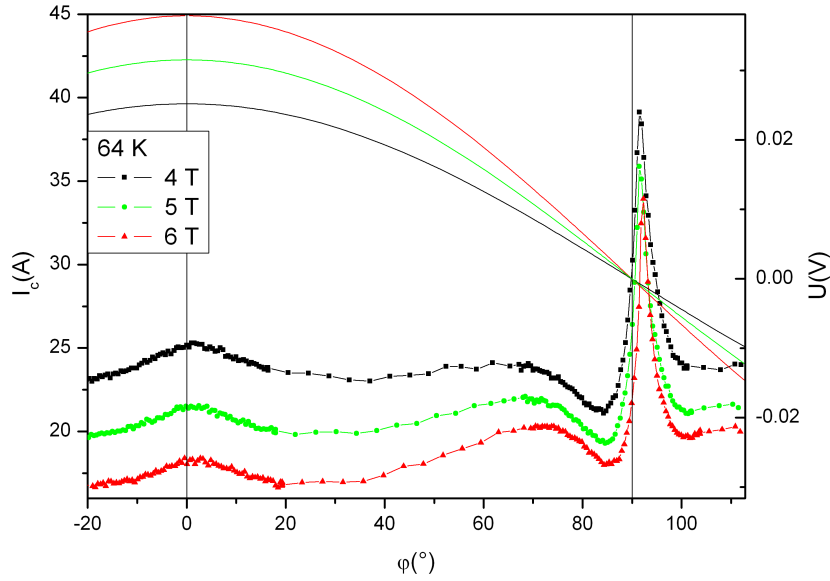
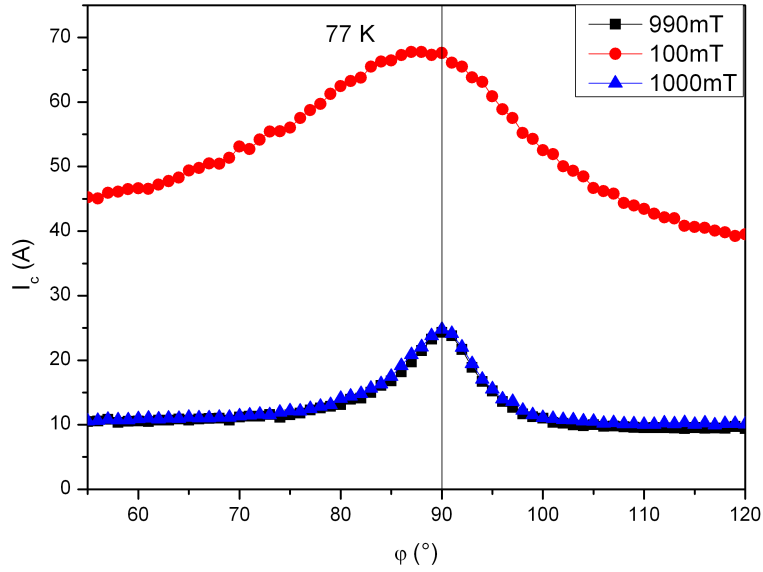


Figure 5.13: Measurements at 64 K, Hall probe employed.

for the same purpose. The measurements were focused on the following goals: first is the position of the ab peak at higher magnetic fields and the second is the ab peak “shift” at varying low magnetic fields. The measurements were performed in the 6 T set-up, a single rotating sample holder equipped with a sensitive Hall probe was used (Figure 4.5b). For better precision, the angular position was assessed via the Hall probe voltage in these measurements. The Hall probe was tested for offset and linearity before the experiment. The output positions from the stepper motor were only for information. The results at 64 K are shown in Figure 5.13.

The ab peak is remarkably off from the $\varphi = 90^\circ$ axis. The misalignment of the peak is estimated to $\Delta\varphi = 2^\circ \pm 0.25^\circ$. The measurements were performed at rather high external magnetic fields $B > 4$ T, where the ab peak is already locked in the stable position. The shift could be pronounced at fields lower than 1 T. However, it is rather problematic to measure at such low fields in the gas flow cryostat due to high heat produced by transport currents. A similar situation with high heat is present also at other temperatures, such as 50 K and 77 K. Nevertheless, the measurements at ~ 77 K could be performed in the electromagnet set-up in liquid nitrogen. The high cooling power of liquid nitrogen allows to measure at very low fields or even without field without any dangerous sample heating. In the electromagnet set-up, the angular resolved measurement was done at 1 T and the

Figure 5.14: Electromagnet set-up - shift of the ab peak.

position of the ab peak was estimated. Since the Hall probe was not employed in this measurement, the relative angular position was estimated only from the stepper $\rightarrow \varphi = 90^\circ$ at the top of the ab peak. The following measurement was done at $\mu_0 H = 0.1$ T and finally the last measurement again at $\mu_0 H = 1$ T (990 mT). The ab peak at 0.1 T changed the position, whereas the reproducibility of the curve at 1 T (990 mT) was demonstrated. The resulting $I_c(\varphi)$ curves are shown in Figure 5.14.

A similar ab peak shift was observed also at 85 K (Figure 5.15). The measurement was again performed in the 6 T measurement set-up at low magnetic fields which were not problematic at such high temperatures.

5.1.3.3 Other features of asymmetry

The main attention will be focused to the second or c -axis peak in this section. This peak was fixed at the same position and rather symmetric at lower temperatures (64 K, 50 K), where the magnetic field was always above 3 T. According to the Hall probe investigation, the real position of the c -axis peak (discussed in Sec. 5.1.3.1, 5.1.3.2) is at $\varphi = 2^\circ$. However, to avoid confusion with the previous sections from the ab planes misalignment, the position of the ab peak was set to $\varphi = 90^\circ$, which results the position of the c -axis peak at $\varphi = 0^\circ$. This approximation is feasible, since no shift of the ab

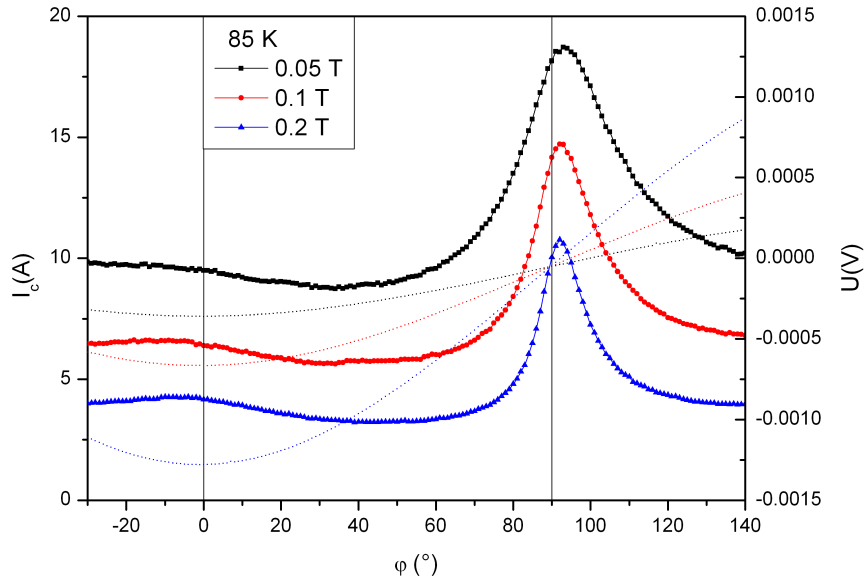


Figure 5.15: Low field anisotropy measurements at 85 K.

peak is observed in the resulting $J_c(\varphi)$ curves (Figure 5.16). The c -axis peak at 77 K is asymmetric and its maximum occurs out of the tape normal ($\varphi = 0^\circ$), e.g. at 1 T the peak is at $\varphi = -5^\circ$. At lower fields, the peak shift is even more pronounced (Figure 5.7), whereas at high fields is almost aligned at $\varphi = 0^\circ$ ($\mu_0 H > 5$ T). Thus it is again at the same position as at lower temperatures. The H and B competition [45], mentioned already by the ab peak shift, must be considered as a possible explanation. However, this effect in the case of the c -axis peak occurs at higher magnetic fields where the critical currents are higher. Therefore a shift of the c -axis peak was unexpected at those fields. In addition, the c -axis peak shapes differ: symmetric and well pronounced at 64 K (eventually 50 K), asymmetric and unclear at 77 K. It indicates different c -axis peak origins at the selected temperatures. This assumption is clarified from the n -value investigation, presented in Figure 5.17, where the n -values exhibit very different behavior at 77 K and 64 K. The pinning properties are possibly changed due to magnetic flux thermal activation and the loss of the pinning efficiency at high temperatures [72]. However, any assumptions do not satisfactory clarify the observed features without microstructural knowledge of the tape. It can be only announced that the c -axis peak arises from natural and also artificial pinning centers. The possible natural candidates are twin planes [48, 49, 50], edge and screw dislocations [51, 52], artificial centres can be e.g. BZO nanorods. The c -axis peak

probably results from a combination of them.

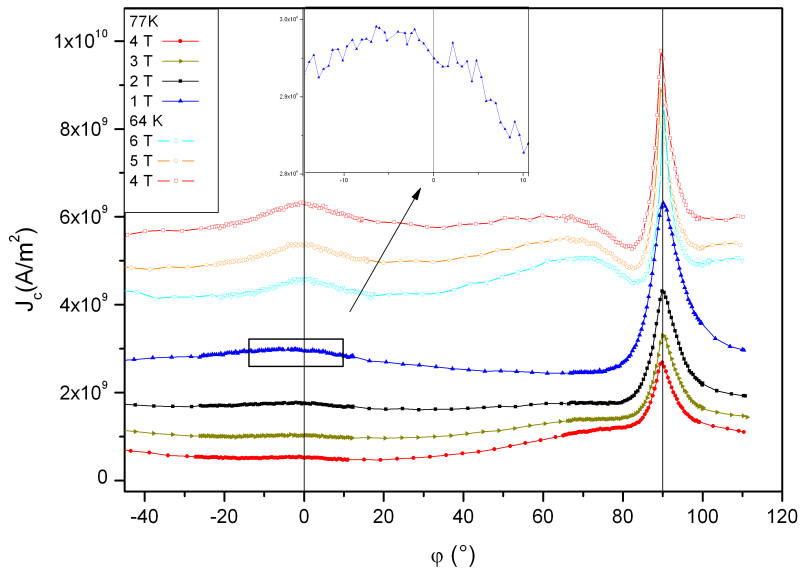


Figure 5.16: $J_c(\phi)$ at 77 K and 64 K in fields up to 6 T.

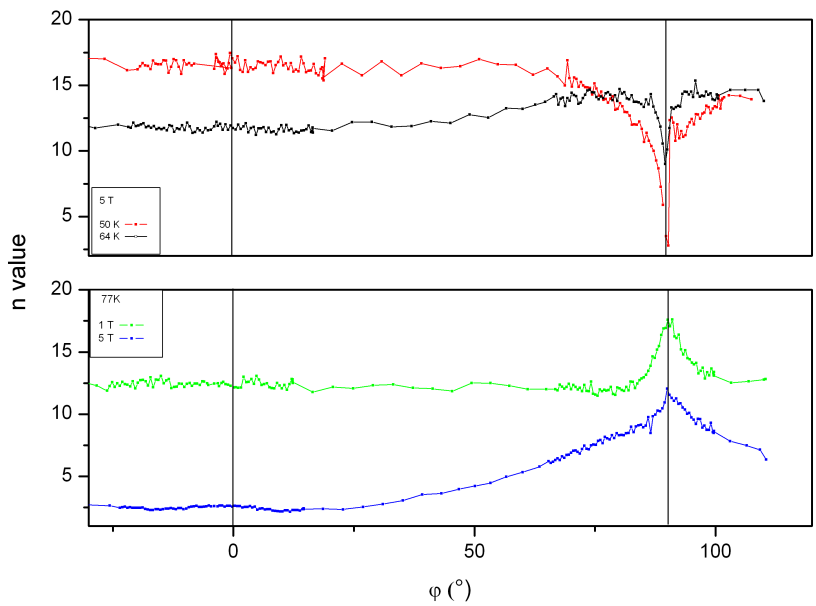


Figure 5.17: n -values of angular resolved transport measurements.

5.2 Characterization in a 2-axis goniometer

After performing the simple angular resolved measurements, the interest was focused on advanced 2 axis angular resolved measurements. These measurements were provided by the high current 2-axis goniometer (Sec. 4.1.6). The $J_c(\varphi)$ characterizations at different “tilt” angles could be valuable for the further investigation of the flux pinning mechanism, e.g. misaligned pinning sites, but also for various applications (fault current limiters, transformers and high field coils). Concerning fusion, the stellator [77] machines may need HTS with highest performance in exotic magnetic field orientations, therefore the 3D $J_c(\varphi, \theta)$ maps could be valuable.

5.2.1 Standard 2-axis measurements

The transport measurements were performed in the full circle angular range $\varphi \langle 0^\circ, 360^\circ \rangle$ and tilt angles of $\vartheta \langle -10^\circ, 100^\circ \rangle$, usually at a magnetic field of 500 mT. All measurements were performed in liquid nitrogen at a temperature of 77 - 78 K. The default φ scan resolution was set to 2° . However, the most interesting areas (around the peaks) were measured also by very fine 0.5° angular resolution. The step size of the tilt angle θ was changed irregularly and usually only after finished a φ scan. The angular position of the sample to the magnetic field was controlled by two stepper motors and two Hall probes. The transport measurements were performed employing the standard 4 - point technique with a voltage criterion of $1\mu\text{V}/\text{cm}$. The resulting $J_c(\varphi)$ resp. $I_c(\varphi)$ curves at field of 500 mT for the SuperPower CC, the EHTS CC and the AMSC CC are presented in Figures 5.18, 5.19, 5.20. All plots show only very small differences between the φ scans at maximal Lorentz force ($\theta = 0^\circ$) and at a tilt angle $\theta = 45^\circ$. Then the differences were enlarged and J_c s emphasized approaching to a tilt $\theta = 90^\circ$. In the case of the SuperPower CC (Figure 5.18), reaching the tilt angle of $\theta = 90^\circ$, both characteristic peaks (ab peak and c -axis peak) were sequentially approaching (from $\theta \sim 70^\circ$) each other. Finally, they collapsed into a single peak roughly at $\varphi = 0^\circ$ at a tilt angle of $\theta = 85^\circ$. This another evidence of the already reported asymmetry (Sec. 5.1.3.1, 5.1.3.2) of the SuperPower CC. The additional asymmetry measurements and theoretical assumption on this tape will be presented in the next section (Sec. 5.2.2). Moreover, the asymmetry of the tape is evident also from the other feature present in Figure 5.18. The c -axis peak is never at $\varphi = 0^\circ$ and the collapsed peak shifts with tilt angles θ from $85^\circ - 90^\circ - 95^\circ$.

The next figure shows (Figure 5.19), that almost all the asymmetry effects disappear in case of the EHTS tape. The measurement at $\theta = 0^\circ$ is not completed, due to a burnout of the sample at very high transport currents. All presented J_c curves meet at the point of

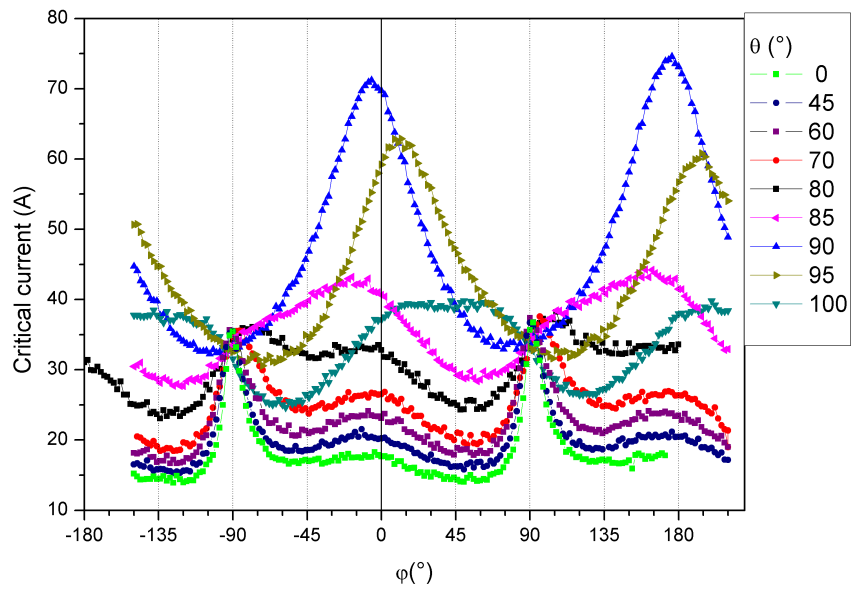


Figure 5.18: The 2-axis angular resolved measurements of the SuperPower CC at a field of 500 mT.

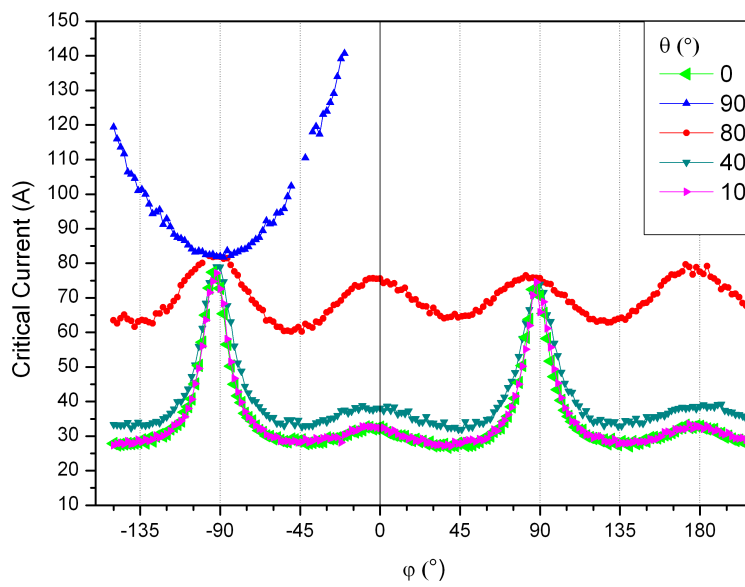


Figure 5.19: The 2-axis angular resolved measurements of the EHTS CC at a field of 500 mT.

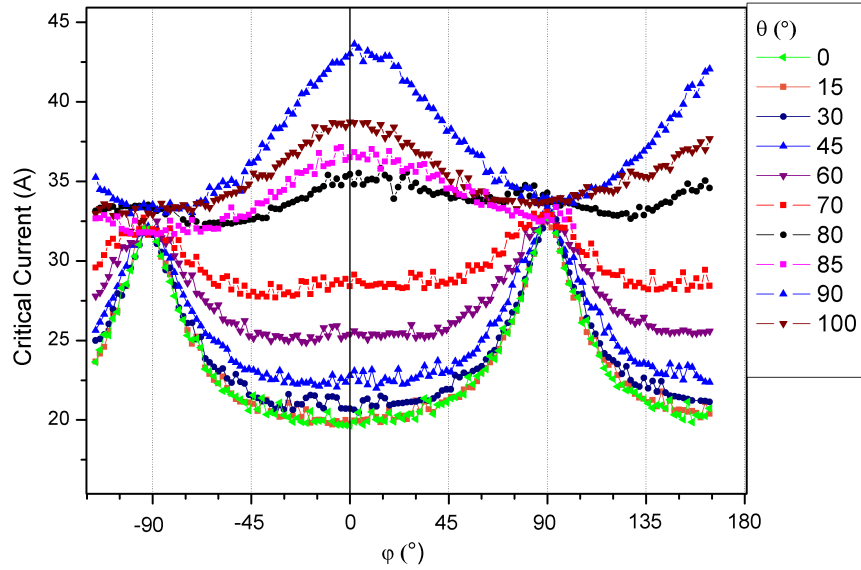


Figure 5.20: The 2-axis angular resolved measurements of the AMSC CC at a field of 500 mT.

the ab peak, which corresponds to the theoretical expectation that the ab planes are well aligned with the sample surface.

The last characterized CC is the 344 CC from AMSC (Figure 5.20). This CC shows a schoolbook symmetric behavior with missing c -axis peak. The crosssection of the $J_c(\varphi)$ for all θ angles meet at one point, $\varphi = 90^\circ$. The ab peak at $\varphi = -90^\circ$ is slightly deformed and the crossover misaligned. The possible reasons are Lorentz force forcing the sample out of the sample holder and surface pinning [53]. The curves at $\theta = 80^\circ$ and $\theta = 100^\circ$ are not identical, which one would expect only for asymmetric tapes. This disagreement is possibly not caused by any special pinning mechanism, as a slight - appx. 2° misalignment between the Hall probe and the sample holder has been found. The previous reasons must be also taken into account as well. The stepper is reset according to the Hall probe before the measurement campaign and therefore, all the presented tilt (θ) angles correspond to the real tilt minus two ($\theta = \theta - 2^\circ$). It is the same for the SuperPower CC in Figure 5.18 and for the EHTS CC in Figure 5.19.

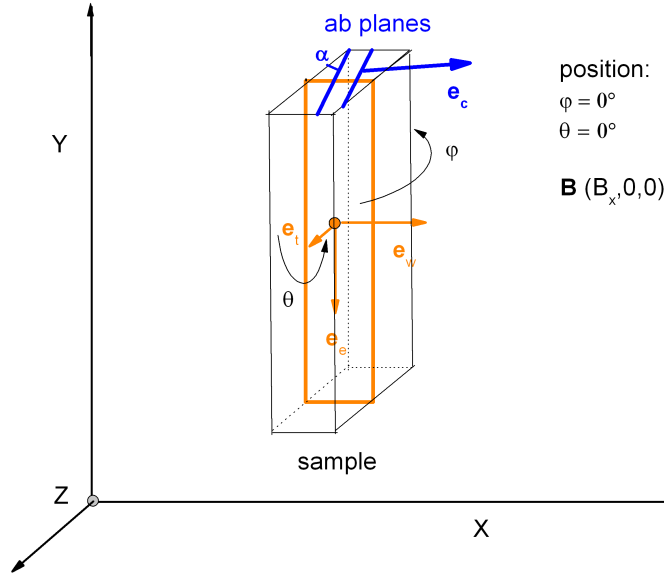


Figure 5.21: Sketch of a sample with tilted ab planes rotated in magnetic field \vec{B} .

5.2.2 Additional asymmetry measurements on the SuperPower CC

The 2-axis high current goniometer gives a special opportunity for additional investigations of the asymmetric J_c behavior of the SuperPower CC. The shift of the ab peak in different tilt angles θ can be easily calculated, if the misalignment angle α is known. The sample surface normals can be described according to Figure 5.21 :

$$\mathbf{e}_e = \begin{pmatrix} \sin \theta \cos \varphi \\ -\cos \theta \\ -\sin \theta \sin \varphi \end{pmatrix} \mathbf{e}_w = \begin{pmatrix} \cos \theta \cos \varphi \\ \sin \theta \\ -\cos \theta \sin \varphi \end{pmatrix} \mathbf{e}_t = \begin{pmatrix} \sin \varphi \\ 0 \\ \cos \varphi \end{pmatrix}.$$

The vector \mathbf{e}_c represents the c-axis of YBCO layer ($\mathbf{e}_c \perp ab$ planes). It can be derived from \mathbf{e}_w , \mathbf{e}_t and from the misalignment angle α :

$$\mathbf{e}_c = \mathbf{e}_w \cos \alpha - \mathbf{e}_t \sin \alpha$$

$$\mathbf{e}_c = \begin{pmatrix} \cos \theta \cos \varphi \cos \alpha - \sin \varphi \sin \alpha \\ \sin \theta \cos \alpha - 0 \\ -\sin \varphi \cos \theta \cos \alpha - \cos \varphi \sin \alpha \end{pmatrix}$$

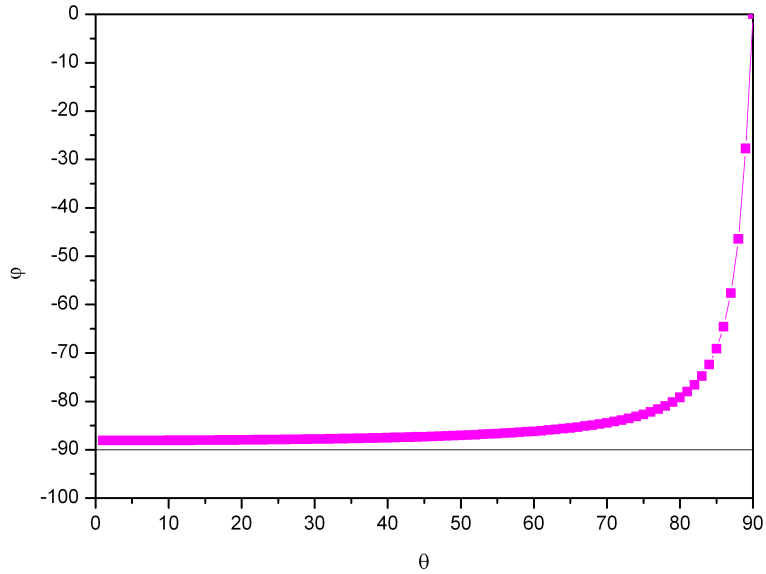


Figure 5.22: Calculated ab peak position dependency on the angle θ . The misalignment angle $\alpha = -1.9^\circ$.

The ab peak is placed at the angle φ , where the ab planes $\parallel B$:

$$\mathbf{e}_c \cdot \vec{B} = 0$$

$$\cos \theta \cos \varphi \cos \alpha - \sin \varphi \sin \alpha = 0$$

$$\varphi = \arctan\left(\cos \theta \frac{\cos \alpha}{\sin \alpha}\right). \quad (5.1)$$

The function in Eq. 5.1 for $\alpha = -1.9^\circ$ is plotted in Figure 5.22. It shows that the ab peak holds its position up to about 70° and then starts to move. This is in excellent agreements with Figure 5.18.

Additional very fine resolved angular measurements were performed to test Eq. 5.1. The ab peak shift was investigated at small tilt angles θ . The step of the each $J_c(\varphi)$ scan was set to 0.5° and the step of the tilt angle θ was 1° . The measurements were done in a tilt interval of $\theta = \langle -10, 10 \rangle$. The results from this measurements are shown in Figure 5.23. Hence no differences between the $J_c(\varphi)$ lines were noticed as expected. The ab peak holds its position which was expected. The ab peak is on the each $J_c(\varphi)$ curve placed

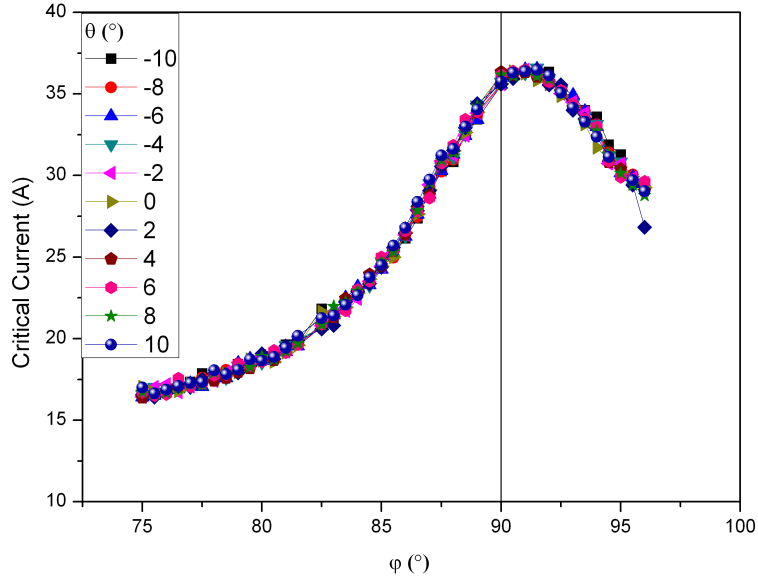


Figure 5.23: Investigation of a peak shift in the SuperPower tape at -500 mT.

about 2° off the axis (92°). An important outcome for applications is the J_c s of the CCs are not affected by small tilt angles at least up to $\sim 10^\circ$.

The next measurements were performed at various external magnetic fields (100 mT, 300 mT and 500 mT) and also at higher tilt angles (Figure 5.24). The situation at 300 mT and 500 mT is rather similar and the peak position stays at 92° and the movement starts from a tilt angle $\theta > 70^\circ$. At 100 mT, the movement has started at lower angles already and the explanation can be again the same as presented in Sec. 5.1.3, e.g. the H and B competition.

Finally, a tilt scan at $\varphi = 90^\circ$ was provided. (Figure 5.25). The I_c is not affected until $\theta = 70^\circ$ and then a noticeable drop is observed. The same $I_c(\theta)$ for a perfectly symmetric tape would be a horizontal line. This scenario perfectly corresponds to a vicinal tape and Eq. 5.1.

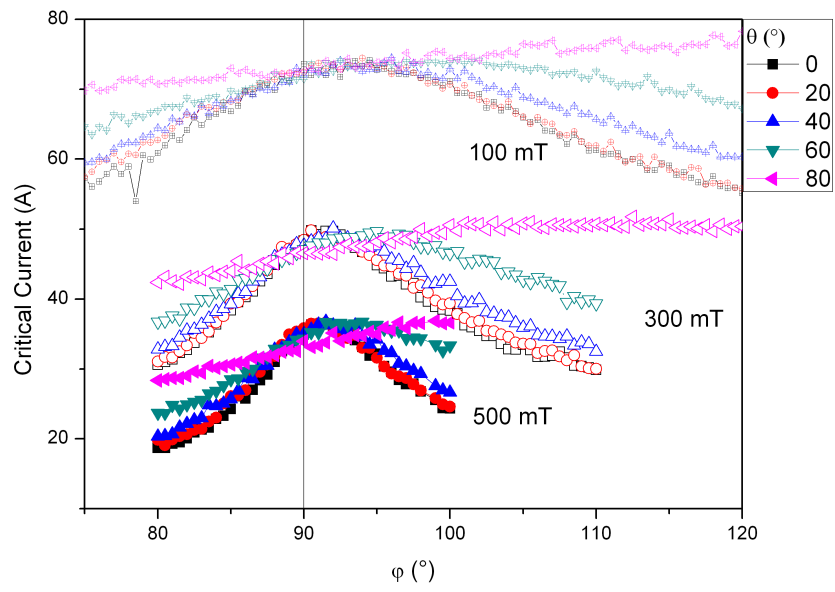


Figure 5.24: Detail of the *ab* peak at different magnetic fields and tilt angles.

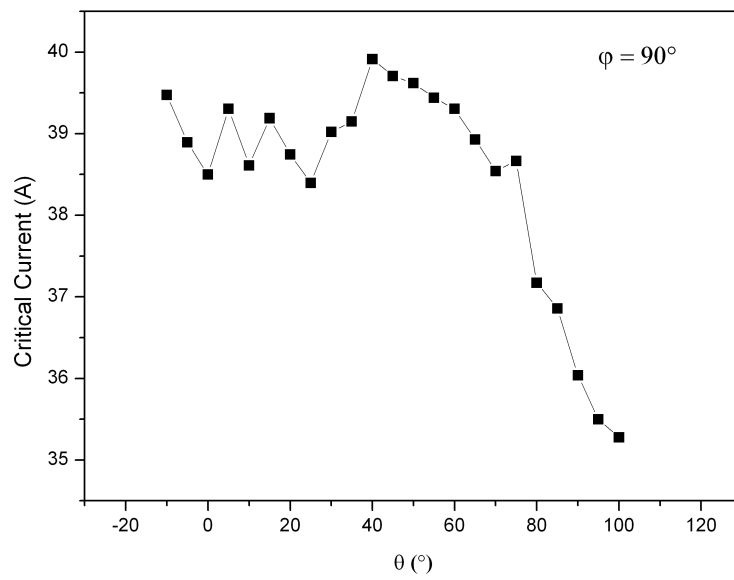


Figure 5.25: Tilt scan of the SuperPower CC at $\phi = 90^\circ$.

5.2.3 Isocurrent investigations

The 2-axis angular resolved measurements allow to spread the area of the J_c anisotropy investigation. The results from this kind of measurements can be presented as complex - 2D or 3D $J_c(\varphi, \theta)$ maps. An isocurrent area is understood as an area with equal I_{cs} , resp. J_{cs} . The next graph shows 3D and 2D isocurrent area maps of the SuperPower CC and the AMSC CC (Figures 5.26, 5.27). A large amount of I-V curves is needed to create a map with a reasonable resolution. Therefore, the 2-axis goniometer was constructed to measure with rather high speed and in long measurement campaigns. The data presented in Figures 5.26, 5.27 are the same data as presented in Figures 5.18, 5.19. The 2D and 3D maps show the areas with highest critical currents and the asymmetry of the SuperPower CC in contrast with the perfect symmetry of the AMSC CC.

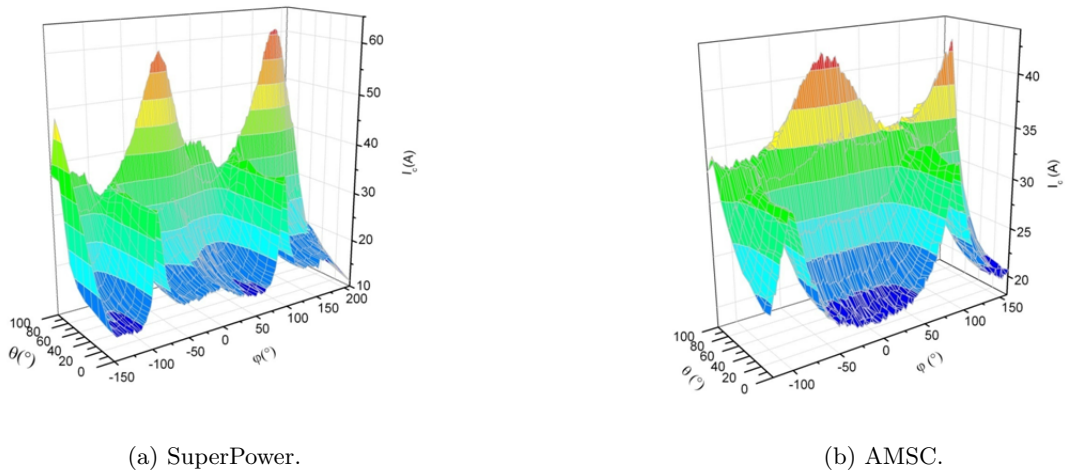
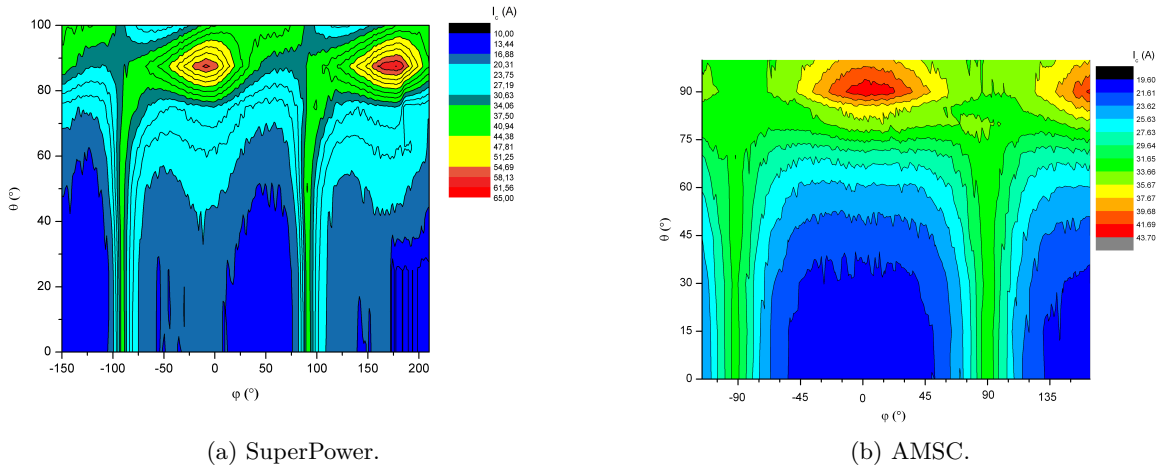


Figure 5.26: I_c 3D maps of CCs.

Figure 5.27: 2D I_c - contour diagrams.

5.3 Measurements after irradiation

The main goal of this thesis will be presented in the next sections. The transport and magnetization measurements were performed after various levels of the fast neutron irradiation. Several samples of CC from SuperPower and EHTS were selected and characterized. The samples for transport measurements were irradiated up to 3 different fast neutron fluences: $2 \times 10^{21} \text{ m}^{-2}$, $4 \times 10^{21} \text{ m}^{-2}$ and $1 \times 10^{22} \text{ m}^{-2}$. The samples suitable for magnetization measurements were irradiated up to fluences: $2 \times 10^{21} \text{ m}^{-2}$, $4 \times 10^{21} \text{ m}^{-2}$, $1 \times 10^{22} \text{ m}^{-2}$ and $1.3 \times 10^{22} \text{ m}^{-2}$. The irradiation procedure was described in Sec. 3.5. This procedure was repeated for each irradiation step.

5.3.1 SuperPower

Each sample was scanned by the magnetoscan scanning technique [54, 55] before the irradiation process. The initial measurement was performed on a longer piece of tape (about 22 cm). The tape was scanned to prove the homogeneity of the whole tape (Figure 5.28).

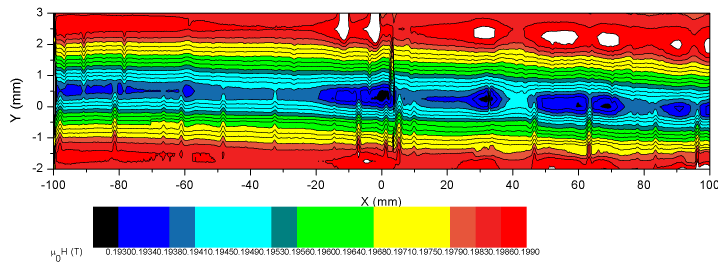


Figure 5.28: Magnetoscan of a 22 cm long piece of SuperPower CC.

This longer piece exhibits good homogeneity, though small rather regularly distributed cracks are still present. Some of the samples used for the characterization were cut from that 22 cm long piece. Magnetoscan maps - contour diagrams of the samples characterized by transport measurements are presented in Figure 5.29. Every sample has at least one or two smaller cracks. However, the magnetic moment of the central area is not significantly affected in none of the cases. All the contour diagrams shown in Figure 5.29 are very similar. Due to this positive information the samples do not need to be considered individually and the results obtained from each of them can be considered and processed together. The same conclusion was obtained from the later transport measurements, where the self field critical currents were compared. These I_{cs} were very similar and the differences between the measurements on a particular sample were often higher than differences in average I_{cs} between different samples. This proves that the results from every sample are very consistent and every sample represents the whole CC reel (Table 2.1). However, the samples can be easily damaged by handling, heat, high current or by the irradiation process. The magnetoscan scanning technique was frequently employed to discover any kind of degradation cracks in a suspicious sample. An example of a partially damaged sample during the characterization procedure is presented in Figure. 5.30

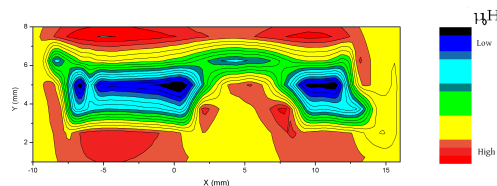


Figure 5.30: Partially damaged sample during characterization.

The samples were usually not scanned after each irradiation step due to problematic handling with a radioactive emitter in the open air cryostat. The scanning was usually

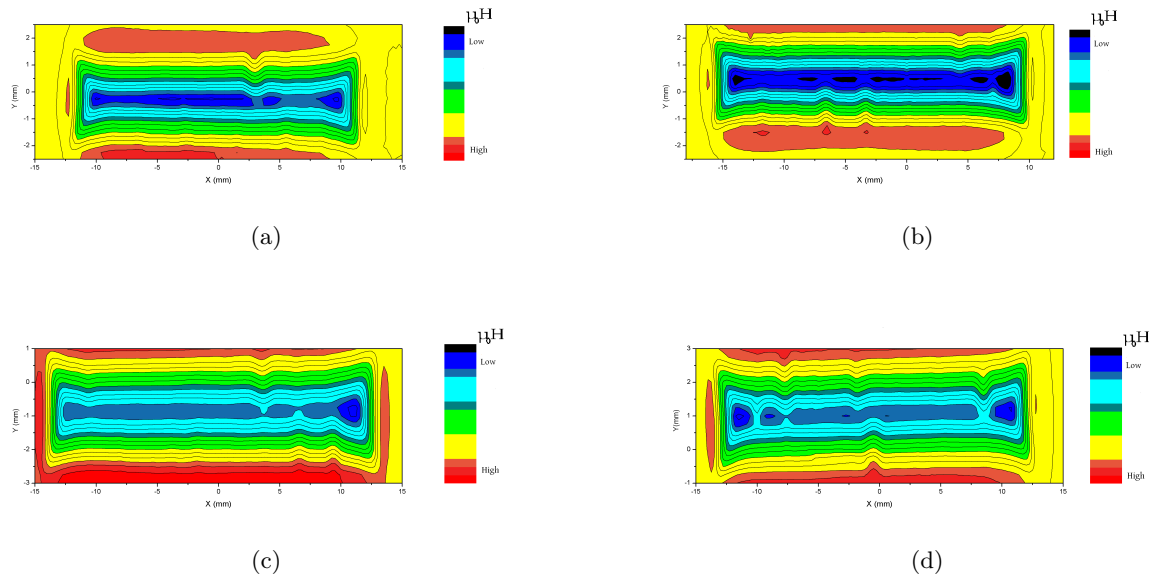


Figure 5.29: 26 mm long SuperPower samples for transport measurements.

provided in special cases, where the performance of the tape dropped. An example of the sample comparison before and after fast neutron irradiation up to a fluence $2 \times 10^{21} \text{ m}^{-2}$ is shown in Figure 5.32. It is important to notice that the magnetoscan of the unirradiated sample was done as a initial measurement, the other scan was performed after irradiation and following characterization. The new cracks are placed mainly, where the current press contacts were made. It clearly demonstrates that cracks in the irradiated tape are introduced by the transport measurements and not by the irradiation procedure. Moreover, in contour diagrams of the smaller, 4 mm long samples for magnetic characterization, noticeable (with respect of introducing new cracks) changes before and after irradiation have never been observed. An example of such a comparison is in Figure 5.32.

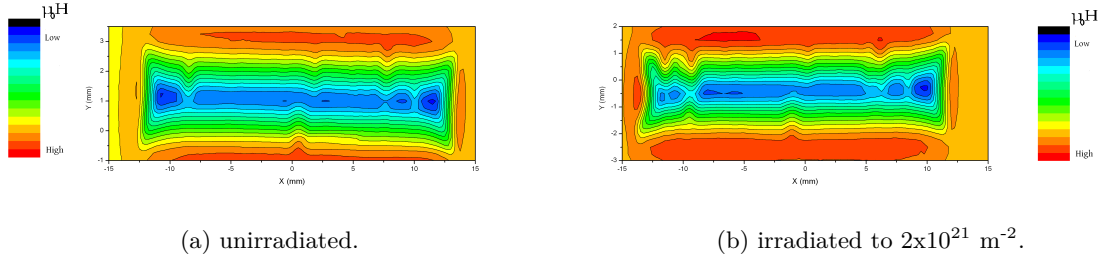


Figure 5.31: Magnetoscan comparison of a SuperPower sample before and after fast neutron irradiation

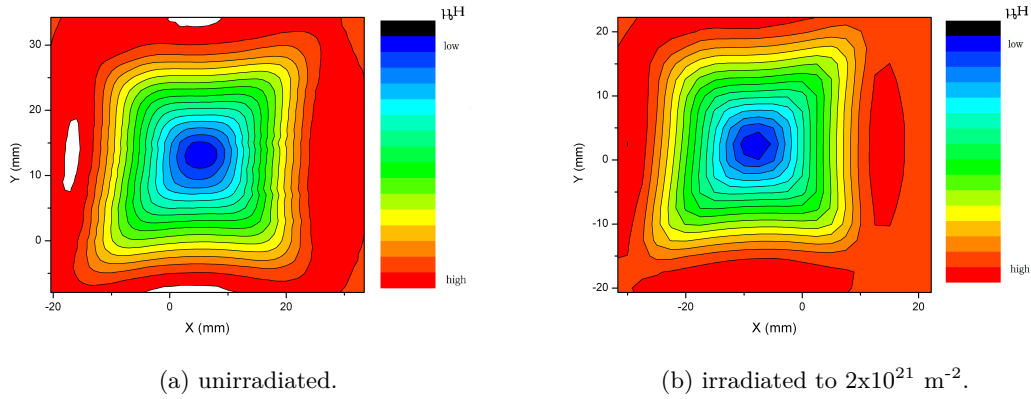


Figure 5.32: Magnetoscan comparison of the SuperPower sample for magnetization measurements.

5.3.1.1 Angular resolved transport measurements up to fields of 6 T

The angular resolved investigation before and after irradiation by fast neutrons was performed in the 6 T set-up (Sec. 4.1.4). The measurements were performed at three different temperatures: 50 K, 64 K and 77 K. The characterized samples were irradiated to three different levels of fast neutron fluences: $2 \times 10^{21} \text{ m}^{-2}$, $4 \times 10^{21} \text{ m}^{-2}$ and $1 \times 10^{22} \text{ m}^{-2}$. The graphs comparing an unirradiated sample and the samples after 3 different irradiation steps are presented in Figures 5.33, 5.34, 5.35. These figures offer the best description of the nature of the fast neutron irradiation on the SuperPower CC, because the overall effect on the angular anisotropy is shown. Beside a strong J_c - enhancement at most of the angular positions, a great reduction of anisotropy is reported. The corresponding anisotropy coefficients are listed in Table 5.5.

Table 5.3: Anisotropy coefficients of SuperPower CC.

50 K	unirr		irr $2 \times 10^{21} \text{m}^{-2}$		irr $4 \times 10^{21} \text{m}^{-2}$		irr $1 \times 10^{22} \text{m}^{-2}$	
	$\frac{J_c(H\parallel ab)}{J_c(H\parallel c)}$	$\frac{J_c^{max}}{J_c^{min}}$						
6 T	1.68	2.16	1.31	1.7	1.2	1.58	1	1.43
5 T	1.56	2.01	1.23	1.61	0.97	1.31	0.95	1.4

64 K	unirr		irr $2 \times 10^{21} \text{m}^{-2}$		irr $4 \times 10^{21} \text{m}^{-2}$		irr $1 \times 10^{22} \text{m}^{-2}$	
	$\frac{J_c(H\parallel ab)}{J_c(H\parallel c)}$	$\frac{J_c^{max}}{J_c^{min}}$						
6 T	1.84	2.02	1.35	1.5	1.25	1.41	1.1	1.37
5 T	1.67	1.85	1.2	1.48	1.09	1.33	0.95	1.37
4 T	1.55	1.86	1.14	1.54	1.03	1.35	0.89	1.42

77 K	unirr		irr $2 \times 10^{21} \text{m}^{-2}$		irr $4 \times 10^{21} \text{m}^{-2}$		irr $1 \times 10^{22} \text{m}^{-2}$	
	$\frac{J_c(H\parallel ab)}{J_c(H\parallel c)}$	$\frac{J_c^{max}}{J_c^{min}}$						
6 T	N/A	N/A	N/A	N/A	N/A	N/A	N/A	N/A
5 T	12.05	16.98	8.38	8.38	9.96	9.96	N/A	N/A
4 T	5.12	5.78	3.78	3.78	4.21	4.21	N/A	N/A
3 T	3.19	3.43	2.39	2.39	2.37	2.37	2.8	2.8
2 T	2.44	2.68	1.71	1.72	1.65	1.65	1.64	1.64
1 T	2.02	2.39	1.53	1.98	1.39	1.7	1.24	1.4

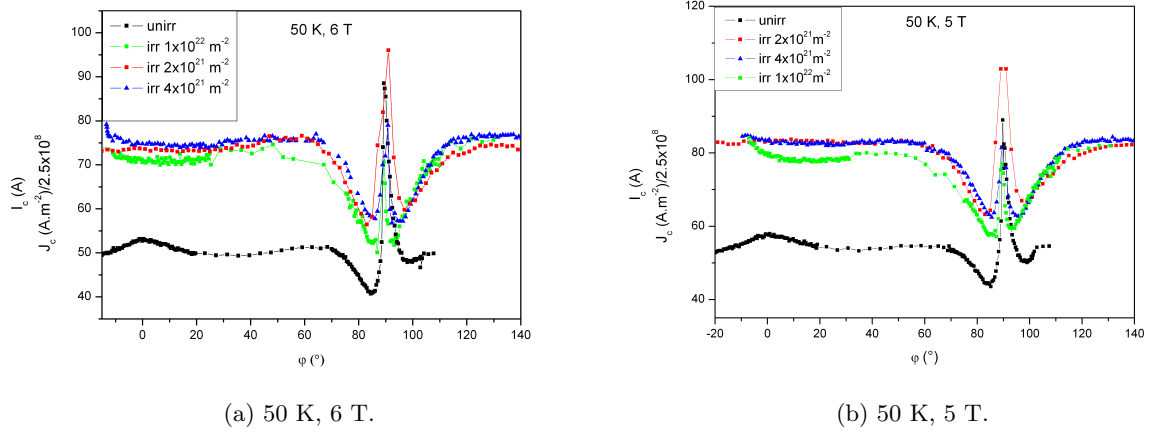
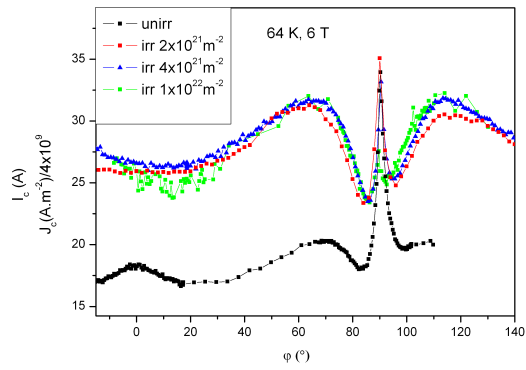


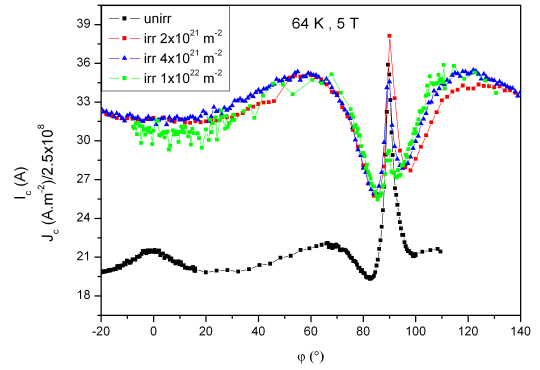
Figure 5.33: Angular resolved transport measurements in the 6 T set-up after different irradiation steps (50 K).

The obtained results show, that fast neutron irradiation can significantly change the properties of the CCs. The most important outputs from these angular investigations are:

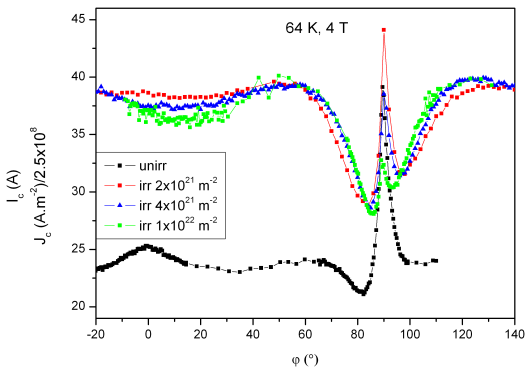
- Generally, the J_c after each irradiation is improved in a wide angular range compare to the pristine samples.
- The highest J_c s are found after a neutron fluence of $4 \times 10^{21} \text{ m}^{-2}$ (or $2 \times 10^{21} \text{ m}^{-2}$ in some cases). The irradiation up to a fluence of $1 \times 10^{22} \text{ m}^{-2}$ leads to reduction of the J_c s compared to lower irradiation levels. However, the obtained J_c s at this irradiation level are still higher than the J_c s of the pristine samples.
- The ab peak at a neutron fluence of $1 \times 10^{22} \text{ m}^{-2}$ is significantly smaller than at lower irradiation fluences or in the pristine samples.
- The c -axis peak disappeared completely after the first irradiation step.
- The J_c anisotropy is reduced after the irradiation. Every other additional irradiation step usually reduces the previous anisotropy coefficients (Table 5.5).
- Additional “shoulder-like” and “plateau-like” features close to $H//ab$ are created (most pronounced at 64 K and 50 K). The origin of these shoulders will be analyzed and described in Sec. 6.1.
- The asymmetry of the ab peak survived all irradiation steps.



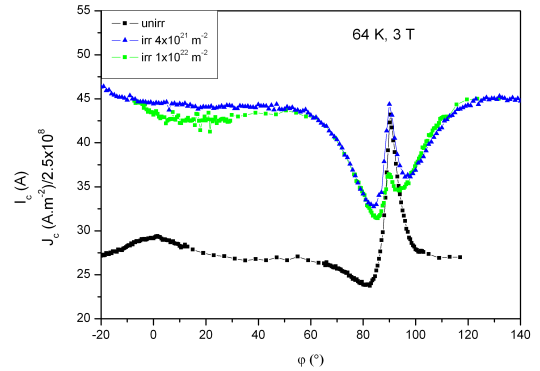
(a) 64 K, 6 T.



(b) 64 K, 5 T.



(c) 64 K, 4 T.



(d) 64 K, 3 T.

Figure 5.34: Angular resolved transport measurements in the 6 T set-up after different irradiation steps (64 K).

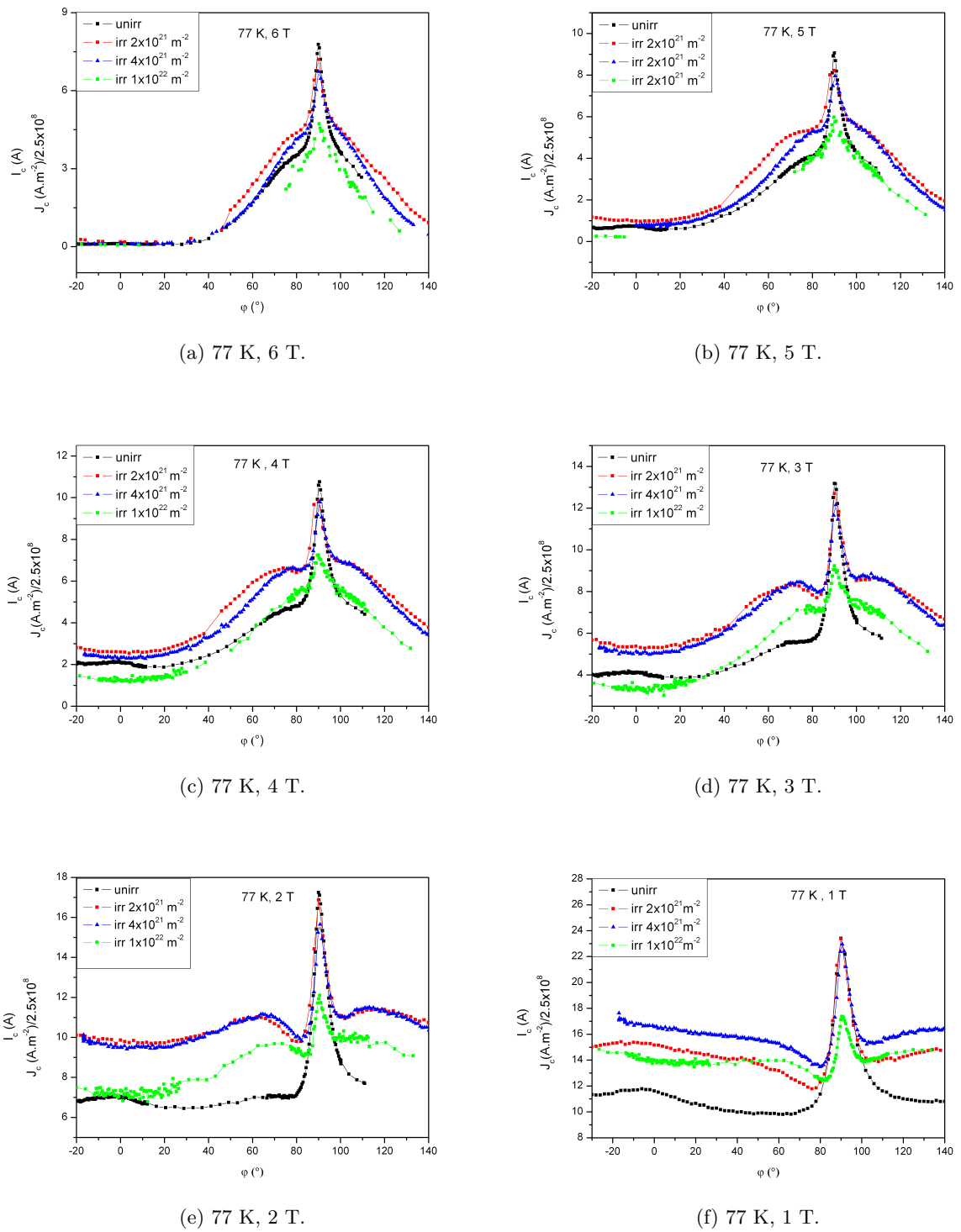


Figure 5.35: Angular resolved transport measurements in the 6 T set-up after different irradiation steps (77 K).

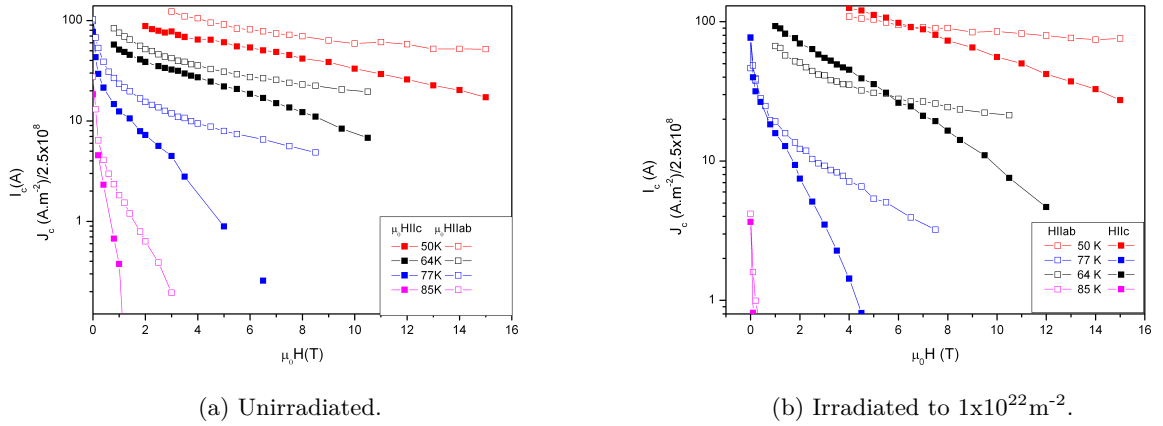


Figure 5.36: Super Power CC at high fields.

The measurements at 77 K and 64 K were made without any technical difficulties. Indeed, the minimal field measured at 64 K is 3 T. However, it must be mentioned that the results at 50 K are not 100 % reliable. Again, the high I_c causes heating and unstable sample temperatures during the transport measurement. In the case of a 4 mm wide CC, the sample temperature can increase by up to 2 K. However, the samples were mounted in the same way and the same measurement sequence was used over all the characterization procedures. It means that although the results are well comparable, the temperature value of 50 K is only approximate. Moreover, the results at 50 K with the “plateau-like” feature will play a crucial role in Sec. 6.1, where the pinning mechanism is discussed.

5.3.1.2 Transport measurements in the 17 T set-up

The next transport measurements were performed in the 17 T set-up (Sec. 4.1.5) at four different temperatures (50 K, 64 K, 77 K, 85 K). The available magnetic fields were up to 15 T. The same samples irradiated to the same fluences were characterized here. Typical results on the unirradiated sample and on that irradiated to a fast neutron fluence of $1 \times 10^{22} \text{m}^{-2}$ are shown in Figure 5.36. The same measurements were done on several samples at 3 different irradiation levels. For better comparison, the measurements are shown for each temperature and plotted together with the J_c s of a pristine- unirradiated sample (Figure 5.37).

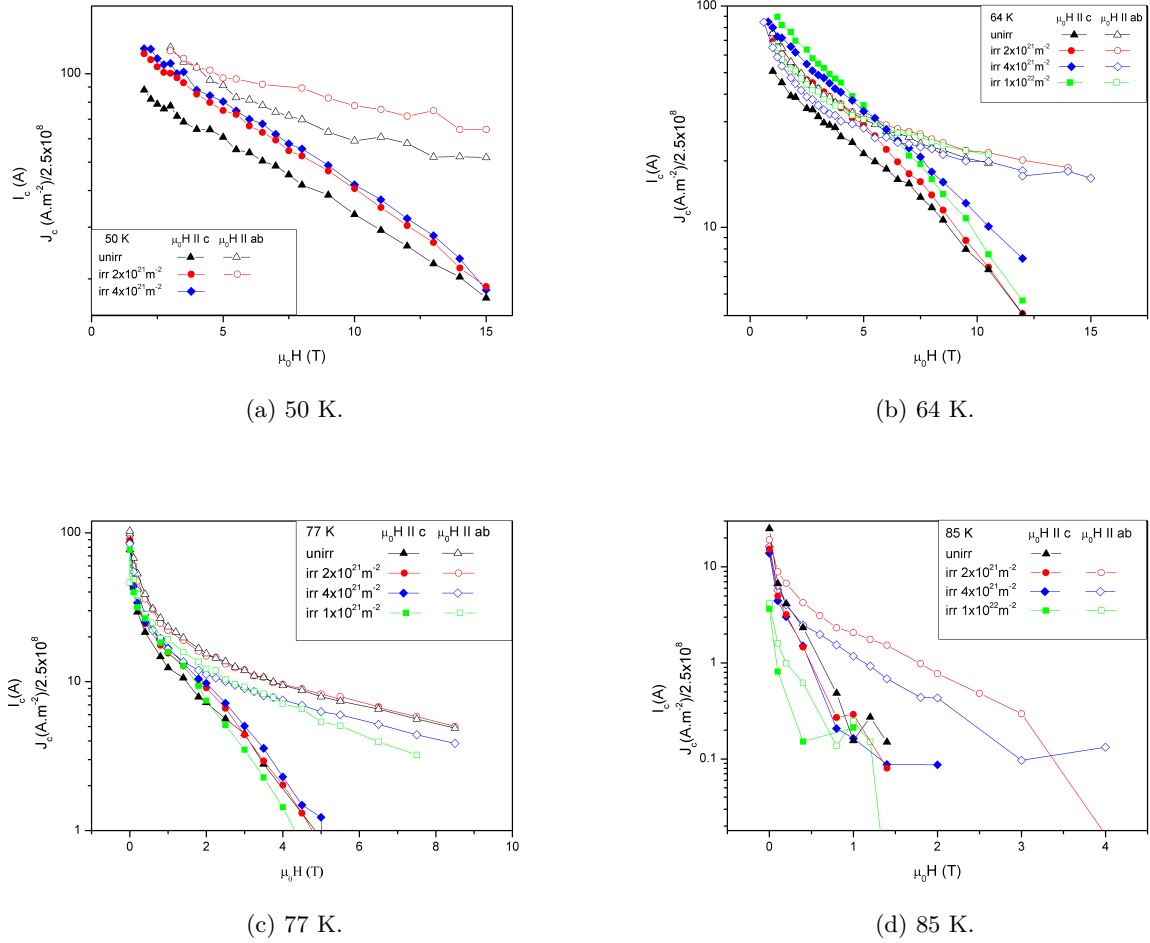


Figure 5.37: Characterization of SuperPower CC, in the 17 T set-up after different irradiation steps.

It is important to recall that the measurements at $H//c$ and at $H//ab$ are not really according to the ab planes, but according to the sample surface. As was presented in Sec. 5.1.3.1, 5.1.3.2, 5.1.3.3, the SuperPower CC has the ab planes about 2 degrees off to the sample surface. As a consequence, the transport measurements at $H//ab$ do not represent the peak value of J_c (from angular resolved measurements - Figures 5.33, 5.34, 5.35) but a value about 2° off the ab peak. Since the ab peak is not symmetric, the critical currents can be different with the orientation of the tape on the sample holder. The problem with the misaligned ab planes is negligible for measurements at $H//c$, as the c -axis peak is rather wide and blunt and the other possible shape features are also rather flat. Even if the results do not correspond to the $H//ab$ position, they have a great value for practical applications

e.g. in coils, where the tapes are possibly aligned due to sample surface and not to the ab planes. All results are in a good agreement with the results from angular resolved measurements performed in the 6 T set-up (Sec. 5.3.1.1). An unique crossover and higher J_c at $H//c$ than at $H//ab$ at low fields can be observed in Figure 5.36b. Focusing to Figure 5.37, the measurements show no real improvement of J_c at $H//ab$. At low fluences e.g. $2 \times 10^{21} \text{ m}^{-2}$, one might notice slight improvements, though they are still within the error of the measurement. The effect is rather opposite with increasing neutron fluence. J_c is reduced (85 K, 77 K). J_c is constant at 64 K and then improved at 50 K. The situation at $H//c$ is very clear. J_c increases with neutron fluences until the fluence exceeds $4 \times 10^{21} \text{ m}^{-2}$. Then, it is reduced at higher fluences. However, the situation at 85 K, which is very close to T_c , is different. Each irradiation causes a J_c reduction. The transport measurements provided at 50 K are always rather problematic and risky due to heating when very high currents are passing through the conductor. Therefore, the characterization at 50 K has not always been successful and some lines are missing.

5.3.1.3 The influence of fast neutron irradiation on T_c and the irreversibility fields

Several studies on neutron irradiated YBCO HTS reported a reduction in T_c [7, 58]. The T_c reduction is caused by the induced disorder in the YBCO lattice. From previous transport measurements, a drop of J_c after irradiation was found at 85 K. Since this temperature is very close to T_c , the T_c reduction is a good explanation of this J_c drop. Therefore, an important part of the characterization of the irradiated CCs are the T_c measurements at $\mu_0 H = 0$ and identical measurements at higher fields, which describe the irreversibility fields. The irreversibility lines were measured up to 15 T for several irradiation levels (Figure 6.10). It is evident from the figure, that T_c (defined at $\mu_0 H = 0$) and the irreversibility fields were reduced due to fast neutron irradiation. Table 5.4 contains the precise results from the T_c measurements. The irreversibility lines are affected at both directions of the magnetic field. Although all previous transport measurements (Sec. 5.3.1.1, 5.3.1.2) showed that J_c is affected by irradiation mainly at $H//c$, it is the other way round in this case (Figure 5.38). The main drop of the irreversible fields is observed at the $H//ab$ field direction and the changes at $H//c$ are smaller. This paradox is elucidated in the next figure (Figure 5.39), where the same irreversibility lines are rescaled by the reduced temperature T/T_c .

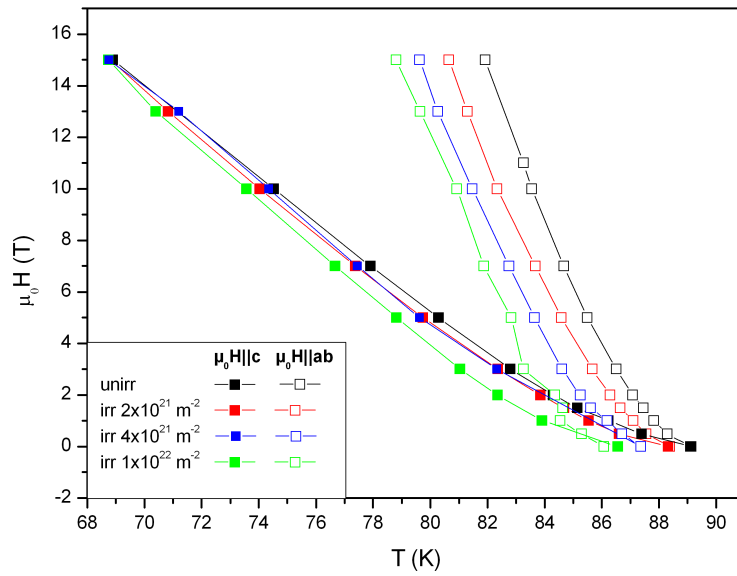
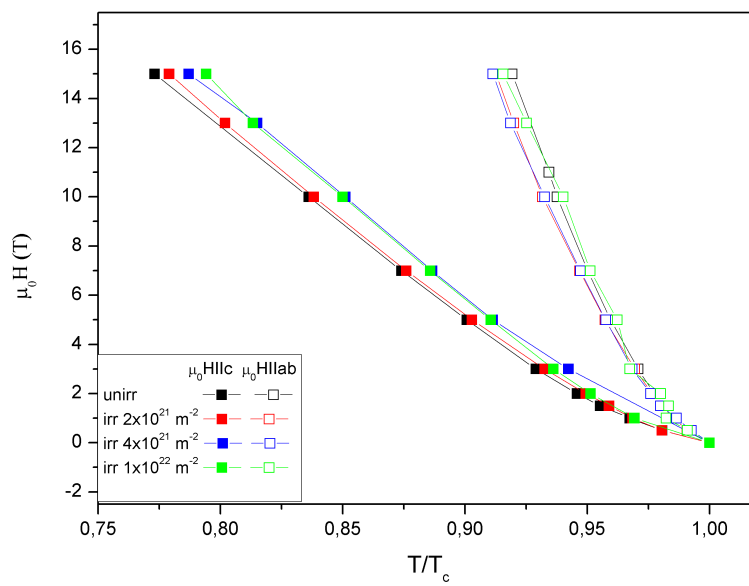


Figure 5.38: Irreversibility lines of the SuperPower CC .

Table 5.4: SuperPower T_c .

irr. level (m^{-2})	2×10^{21}	4×10^{21}	1×10^{22}	1×10^{22}
$T_c(K)$	89.1	88.35	87.36	86.2



76
Figure 5.39: SuperPower, Irreversibility lines on reduced temperature scale.

Thus the irreversibility lines are in agreement with the other results obtained from transport measurements.

5.3.1.4 VSM measurements

The magnetic measurements of critical current densities were performed in the VSM (Sec. 4.2.2). These measurements are fast, reliable and without an electrical contact. The samples used are much smaller – typical size 4x4 mm, due to the high induced signal. In addition, the smaller samples allow easier handling after high irradiation, as the activity is simply lower. The VSM measurements are valuable, as the J_c s could be measured at low temperatures, where direct transport measurements are not available anymore. The results on the SuperPower CC are presented in Figure 5.40. All measurements correspond to the $H//c$ magnetic field orientation. The irradiation enormously enhanced the J_c s at lower temperatures, such as 5 K or 20 K. The effect is rather weaker at higher temperatures (> 77 K). J_c is improved at temperatures, except 85 K.

A crossover in the $J_c(B)$ dependence between the pristine and the irradiated samples is observed at some temperatures (Figure 5.40). This feature is fully described by Eisterer et al. [57]. The crossover is present at low or very low fields, where a possible transition between the critical current density limited by grain boundaries ($J_{c,GB}$) and critical current density limited by grains ($J_{c,G}$) occurs. Two different mechanisms can explain this behavior. They are independent, do not exclude each other and may work together. First, the radiation induced defects are mobile during irradiation process. The grain boundaries are the natural barriers in this motion and accumulate the defects. This accumulation causes a deterioration of grain boundaries. Although the number of large defects induced by irradiation ($\sim 1 \times 10^{22} \text{ m}^{-2}$) is too low to significantly reduce the cross section for the current transport, J_c can be reduced if the current transport is limited by grain boundaries, which are damaged. The second mechanism is based on the field produced by intra-granular shielding currents on the grain boundaries. In general, irradiation by fast neutrons increases $J_{c,G}$. Evidence for this is the fact that J_c is always improved at high fields. If $J_{c,G} > J_{c,GB}$, additional magnetic flux remains trapped inside the grains. Afterwards, when the external field changes, the trapped circulating currents generate an additional field at the grain boundaries, which reduces the intergranular current transport. The enhancement of this mechanism after fast neutron irradiation is an effect of the $J_{c,G}$ improvement due to irradiation induced pinning.

Another interesting issue is to estimate the fluence, which enhanced J_c most. The investigation has been done at 77 K and 64 K at certain fields (Figures 5.40d, 5.40e - black vertical lines). The resulting graphs are presented in Figure 5.41. Figure 5.41a is

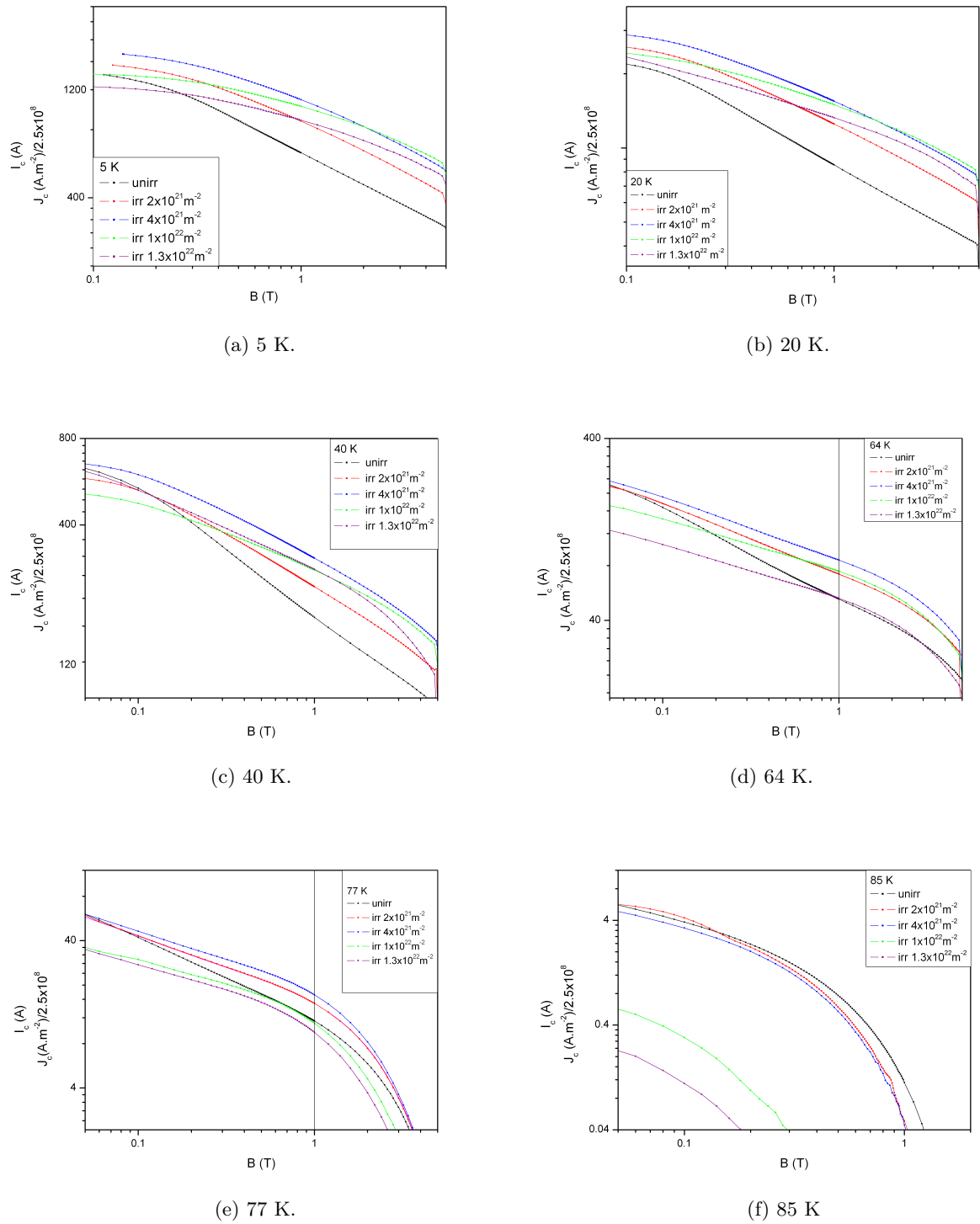


Figure 5.40: Measurements in the VSM at different fluences of fast neutron irradiation, $H//c$.

evaluated from several measurements performed on 5 different SuperPower samples. The plot includes the variances of the data points as well. As a result, J_c is mos improved at a fluence of $4 \times 10^{21} \text{ m}^{-2}$. This is the level, where the next irradiation begins to reduce the previously enhanced J_c .

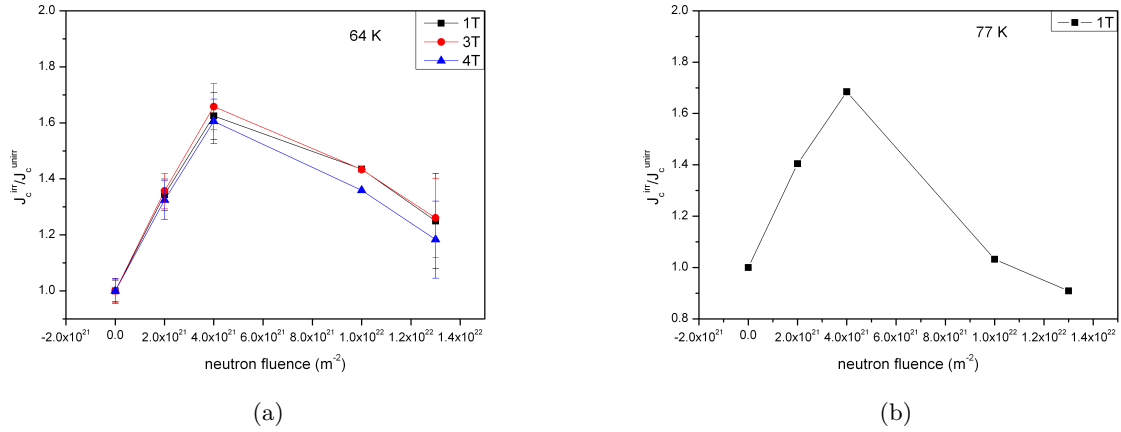


Figure 5.41: Relative J_c enhancement after different irradiation steps.

5.3.2 EHTS

Similar kind of characterizations were performed on the CC from EHTS, although the major part of the characterization on this CC has already been done by R. Fuger [8]. Therefore, only a few missing measurements were made, i.e. transport measurements at high fields and angular resolved transport measurements. Magnetoscan measurements had been performed before the initial transport measurements and the irradiation procedure. Scans of several 26 mm samples had shown very good homogeneity, similar to that one reported for SuperPower (Sec. 5.3.1). Figure 5.42 shows an example of a magnetoscan of a homogeneous EHTS sample.

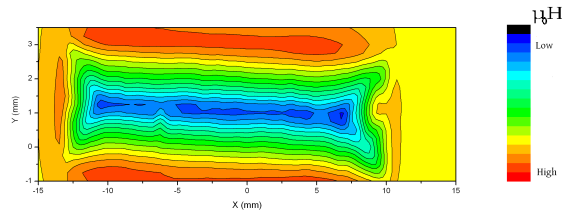


Figure 5.42: Magnetoscan of the EHTS CC.

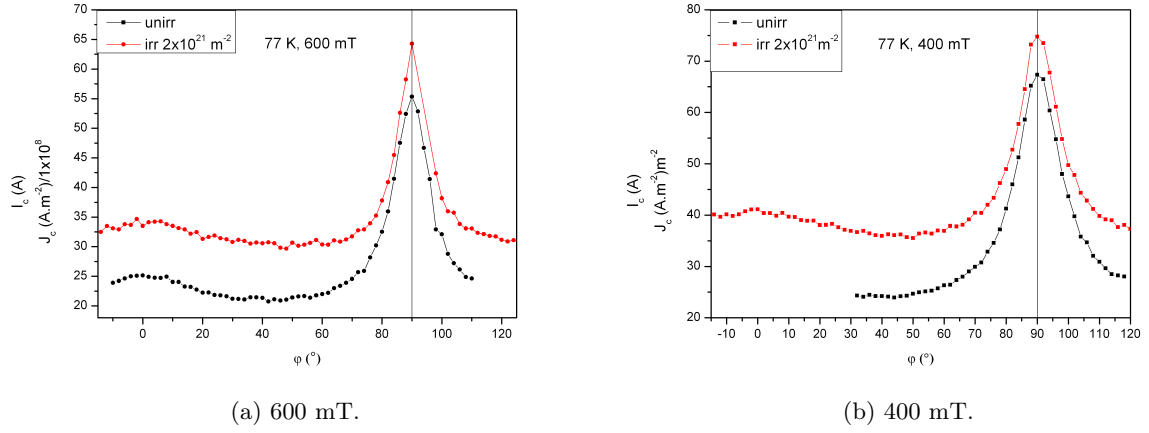


Figure 5.43: EHTS CC measured at low fields in the electromagnet set-up.

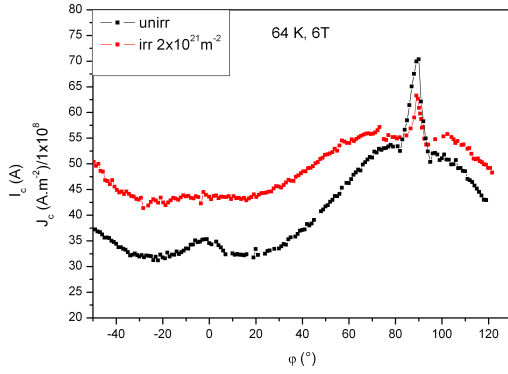
The irradiation was done up to a fast neutron fluence of $1 \times 10^{22} \text{ m}^{-2}$. Unfortunately, none of the irradiated 26 mm long samples was superconducting at fluences above $2 \times 10^{21} \text{ m}^{-2}$. It is possible that the deterioration is due to moisture inside the quartz glass or maybe by the bad sealing of the ampule, which is done at high temperatures ($\sim 1000 \text{ }^{\circ}\text{C}$). Nevertheless, the results at the fluence of $2 \times 10^{21} \text{ m}^{-2}$ are satisfactory for studying the pinning mechanism. However all the 4 mm samples characterized by magnetic measurements, which were irradiated separately, show very good properties even after irradiation to very high fluences, such as $2 \times 10^{22} \text{ m}^{-2}$.

Figure 5.43 presents angular resolved transport measurements at relatively low fields. The measurements were made in the electromagnet set-up (Sec. 5.14), where the effective liquid nitrogen cooling ensures reliable measurements with very high transport currents. As shown in the figures, the critical currents were relatively high. The ab peak was stable before and after irradiation as well. An important information is that the $J_c(\varphi)$ is enhanced for every possible angle φ . The following anisotropy measurements were performed in the 6 T set-up (Sec. 4.1.4) and the resulting graphs can be found in Figures 5.44, 5.45. Except for the ab peak at the 64 K - 6 T measurement, no other $J_c(\varphi)$ degradation due to irradiation is observed. However, the critical currents are very high at this temperature, which produces heat and some unreliability of the result as shown by the noisy $J_c(\varphi)$ and the deformed ab peak. (Figure 5.44a after irradiation).

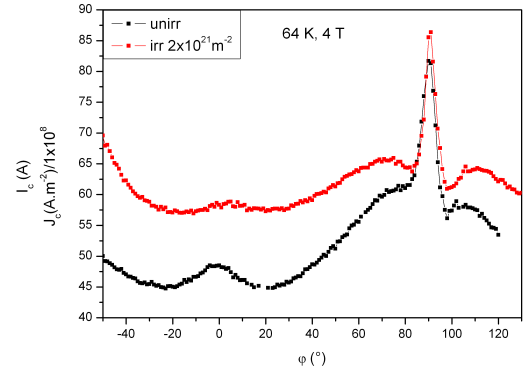
Table 5.5: Anisotropy coefficients of EHTS CC.

64 K	unirr		irr $2 \times 10^{21} \text{m}^{-2}$	
	$\frac{J_c(H\parallel ab)}{J_c(H\parallel c)}$	$\frac{J_c^{max}}{J_c^{min}}$	$\frac{J_c(H\parallel ab)}{J_c(H\parallel c)}$	$\frac{J_c^{max}}{J_c^{min}}$
6 T	1.98	2.185	1.45	1.45
5 T	1.86	2.04	1.44	1.46
4 T	1.68	1.82	1.48	1.5

77 K	unirr		irr $2 \times 10^{21} \text{m}^{-2}$	
	$\frac{J_c(H\parallel ab)}{J_c(H\parallel c)}$	$\frac{J_c^{max}}{J_c^{min}}$	$\frac{J_c(H\parallel ab)}{J_c(H\parallel c)}$	$\frac{J_c^{max}}{J_c^{min}}$
6 T	N/A	N/A	N/A	N/A
4 T	10.6	11.2	8.45	8.45
2 T	2.56	2.78	2.37	2.42
1 T	1.93	2.22	1.81	1.97



(a) 64 K, 6 T.

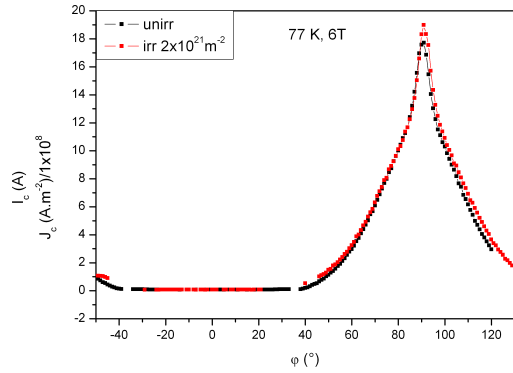


(b) 64 K, 4 T.

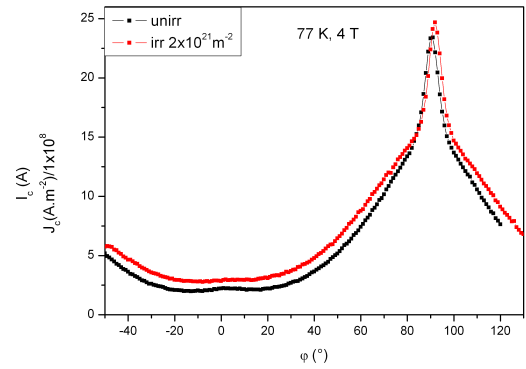
Figure 5.44: EHTS CC measured in the 6 T set-up at a temperature of 64 K.

Other features such as a “shoulder-like” behavior or the missing c -axis peak are present after the irradiation as well. However, they are much less pronounced than in the SuperPower CC. The minima (64 K) near the ab peak are shallow and some remains of the c -axis peak are still noticeable close to $\varphi = 0^\circ$. The anisotropy coefficients are listed in table 5.5.

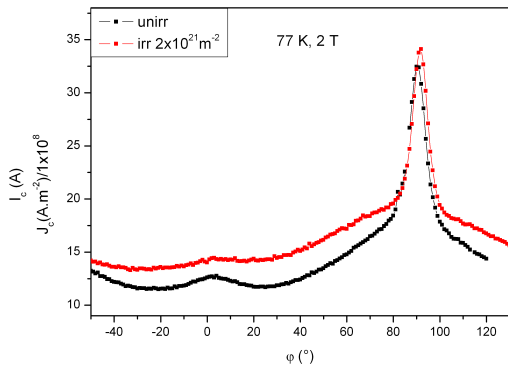
Transport measurements at high magnetic fields were done in the 17 T set-up (Sec. 4.1.5). The results are shown in Figures 5.46, 5.47. The measurements at 64 K and 77 K (both $H\parallel c$) show the J_c enhancement after irradiation. The situation is different at 85 K again, where J_c is reduced is reported. A crossover between J_c at $H\parallel c$ and J_c at $H\parallel ab$ is



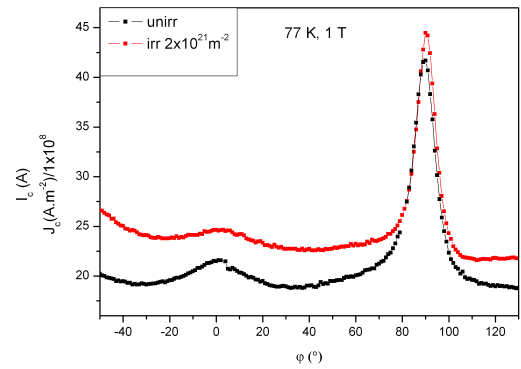
(a) 77 K, 6 T.



(b) 77 K, 4 T.

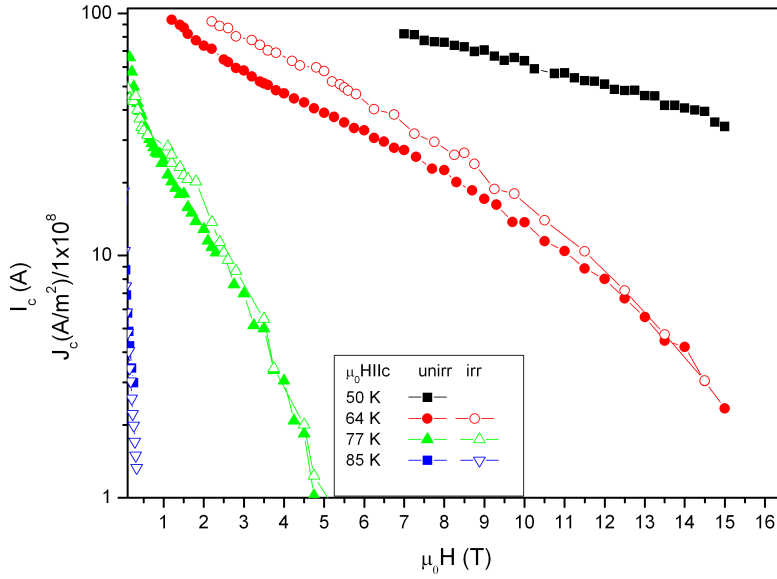


(c) 77 K, 2 T.



(d) 77 K, 1 T.

Figure 5.45: EHTS CC measured in the 6 T set-up at a temperature of 64 K.

Figure 5.46: EHTS CC measured in 17 T set-up at $H//c$.

observed just like in the SuperPower CC.

From the magnetization measurements on the EHTS CC [8], J_c as a function of the fast neutron fluence at 77 K and 1 T is shown in Figure 5.48, which demonstrates that the CC from EHTS keeps a high performance even at high fast neutron fluences. Conclusions:

- The EHTS CC is characterized by high critical currents I_c , but lower critical current densities J_c .
- The tape has probably well aligned ab planes with the sample surface, though it still shows a slightly asymmetric $J_c(\varphi)$.
- Fast neutron irradiation to a fluence of $2 \times 10^{21} \text{ m}^{-2}$ reduces the anisotropy and enhances $J_c(\varphi)$ for all the angles φ . The CC is very resistant to neutron radiation, and fluences, such as $2 \times 10^{22} \text{ m}^{-2}$, still enhance J_c at high temperatures (77 K, 1 T).
- Although a “shoulder-like” feature close to $H//ab$ is created, it is significantly less pronounced than in the SuperPower CC.

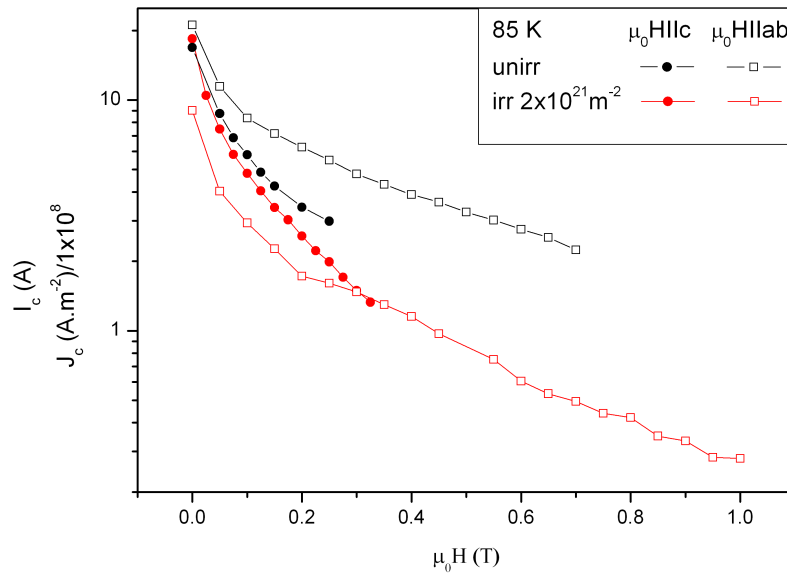


Figure 5.47: EHTS CC at 85 K before and after irradiation.

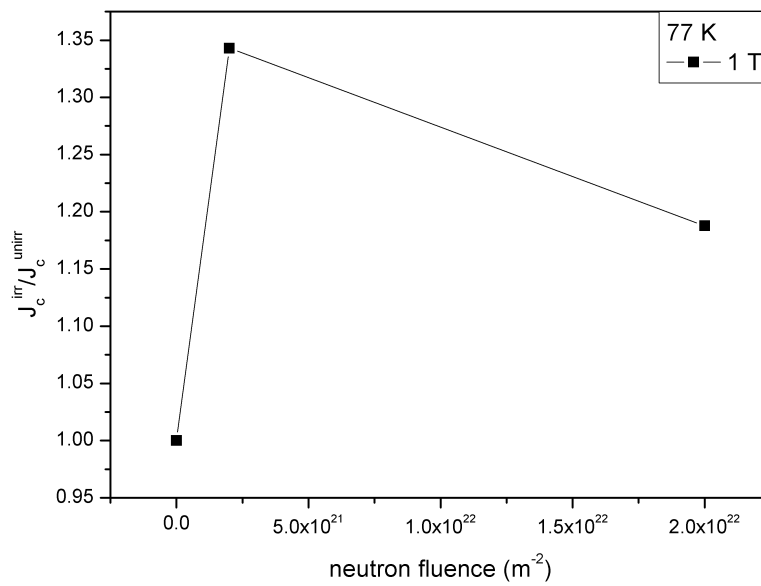


Figure 5.48: Relative J_c at 77 K and 1 T for the EHTS CC (VSM, $H \parallel c$).

6 Impact of Neutron Irradiation on Coated Conductors

6.1 Pinning mechanism

One of the issues of this thesis is to elucidate the pinning mechanism induced by fast neutron irradiation. The enhancements of J_c in YBCO single crystals or tapes have been already discussed many times [7, 8, 58] and satisfactorily explained. Accordingly the enhancement is caused by the introduction of additional effective pinning centres with a diameter of 1-5 nm. Smaller point defects explain the T_c reduction by the introduction of disorder into the YBCO lattice, particularly the oxygen sublattice. However, the features observed in the SuperPower CC at angular resolved measurements (Sec. 5.3.1.1) require an additional explanation, especially the “shoulder-like” feature created on the both sides of the ab peak.

The anisotropic scaling approach [37] is a powerful tool, which allows to study the $J_c(\varphi)$ angular anisotropy of CCs within collective pinning theory [59] and distinguishes between correlated or uncorrelated pinning in various angular intervals. Transforming isotropic to anisotropic functions in the Ginzburg-Landau and London equations is done by a scaling rule [37]:

$$Q(\varphi, H, T, \xi, \lambda, \varepsilon, \gamma) = s_Q \tilde{Q}(\varepsilon_\varphi H, T/\varepsilon, \xi, \lambda, \gamma/\varepsilon), \quad (6.1)$$

where ξ is the planar coherence length, λ - magnetic penetration depth, ε - anisotropy, γ - scalar disorder strength, H - applied magnetic field, φ - enclosing angle and T - temperature. An example of the anisotropic scaling on the SuperPower CC is presented in Figure 6.1. A standard transformation

$$J_c(H, \varphi) = J_c(\tilde{H}) \quad (6.2)$$

$$\tilde{H} = H\varepsilon(\varphi)$$

$$\varepsilon(\varphi) = (\cos^2\varphi + \gamma^{-2}\sin^2\varphi)^{-\frac{1}{2}}$$

is commonly used for (RE)BCO HTS material. The mass anisotropy for YBCO is [60]:

$$\gamma \approx 5 - 7. \quad (6.3)$$

According to L. Civale et al. [60], different regimes in a default $J_c(\varphi)$ dependence were defined. The first is near the ab planes, the intrinsic pinning is considered as a pinning source. This pinning is associated with the periodic modulation of the superconducting order parameter, which arises from the layered structure of YBCO. If the applied magnetic field is progressively tilted from the ab planes, the vortices are still pinned until a certain angle φ_L is reached. The angle φ_L is called lock-in angle and therefore this regime will be denoted as the lock-in regime. A $J_c(\varphi)$ plateau is present in this regime (Figure 6.1 - inset). It is usually rather small in CCs and φ_L does not exceed 0.1° . The second regime is defined as the “staircases” regime. In this regime, a monotonic decrease of the $J_c(\varphi)$ is observable. The border angle φ_t is defined by the full width at half ab peak maximum (FWHM). As the peak base the crossover of the $J_c(\varphi)$ with the $J_{c,asa}(\varphi)$ fit is taken. This is an intermediate regime, where the effect of intrinsic pinning is smeared out. A broad ab peak comes from mass anisotropy and not from intrinsic pinning. Thus the next regime ($\varphi_t - \varphi_{tC}$) is affected by electric mass anisotropy of YBCO and uncorrelated pinning centres. The last regime is present near the broad c -axis peak. A trapping angle φ_{tC} is defined as the place, where the $J_c(\varphi)$ merges with the $J_{c,asa}(\varphi)$ fit. As was already mentioned, the c -axis peak can arise from natural correlated defects such as twin planes, edge and screw dislocations [51, 52]. For angles above φ_{tC} , $J_c(\varphi)$ is not affected by this correlated pinning anymore.

During the last years, the Blatter anisotropic scaling approach has become a widely used tool to study the origin of pinning in anisotropic superconductors. The sequence utilized by L. Civale (Eq. 6.2) was applied in numerous papers from different authors. V. Silhanek together with L. Civale [61] succeeded to scale even YBCO crystals with columnar defects. Others, e.g. Gutierrez et al. [62] scaled YBCO with $\gamma = 3$, which is out of the realistic range of γ . Similar inconsistencies, where the scaling is problematic, strange or hardly possible are present in many types of YBCO tapes or single crystals. The Blatter model describes $J_c(\varphi)$ arising from the electronic mass anisotropy and isotropic point defects. It is not clear, how does this approach apply when the strong pinning is dominant. From the collective pinning theory, there is no reason that Blatter scaling works for the strong pinning. Therefore, N.J. Long presented a different model describing the angular anisotropy of J_c in his work [63]. His model emphasizes the statistical distribution of the pinning encountered by a vortex as determining the observed $J_c(\varphi)$ features. According to his model, the $J_c(\varphi)$ function can be always derived from anisotropic defect population

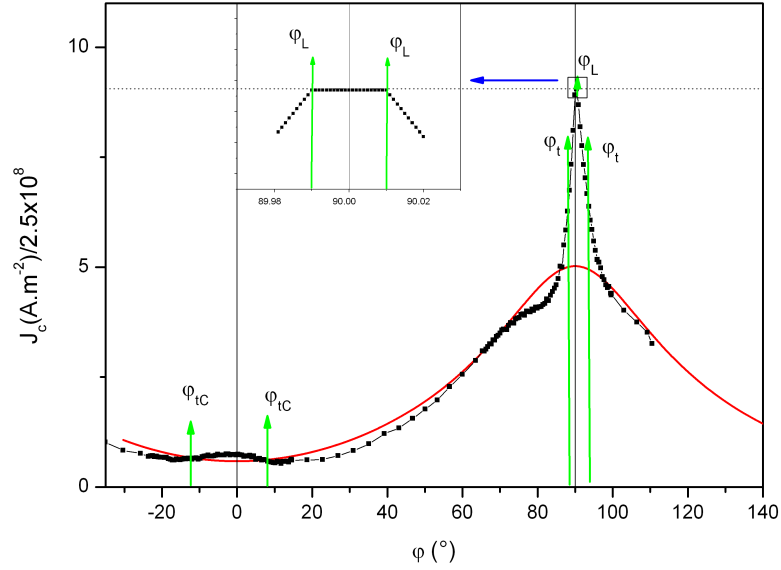


Figure 6.1: Pinning regimes in YBCO, SuperPower CC at 77 K, 5 T, $J_{c,asa}(\varphi)$ fit (red line) is done with $\gamma = 3$. The inset does not correspond to a real measurement.

and the wide usage of the Blatter scaling for YBCO tapes is a misunderstanding of the paper from Blatter [64].

6.1.1 Blatter scaling of the SuperPower CC

The scaling of the SuperPower CC (before irradiation) can be classified as quite problematic. The first reason is the observed asymmetry (Sec. 5.1.3.1, 5.1.3.2). However, it is easily possible to correct the ab peak in the $J_c(\varphi)$ plot to the position $\varphi = 90^\circ$ and exclude the measurements at very low fields, where the ab peak is not stable and is being shifted. The $J_c(H, \varphi) = J_c(\tilde{H})$ (Eq. 6.2) transformation of the SuperPower CC at 77 K is shown in Figure 6.2. The figure explores the second scaling problem, as the curves collapse better at lower γ ($\gamma=3$) than according to Eq. 6.3. The resulting scaling dependence is plotted in Figure 6.1 and corresponds quite well to the experimental results between the angles φ_{tC} and φ_t . The scaling at 64 K has been done in very similar way and the resulting scaling curve is shown in Figure 6.3. The third scaling problem has been detected after the $J_c(H, \varphi) = J_c(\tilde{H})$ transformation with any γ from an interval $\gamma = \langle 3, 7 \rangle$. The curves only partially collapse, however the approximation was more accurate with a double exponential function: $J_c = A_1 \exp(-\tilde{H}/t_1) + A_2 \exp(-\tilde{H}/t_2) + J_{C0}$ than with

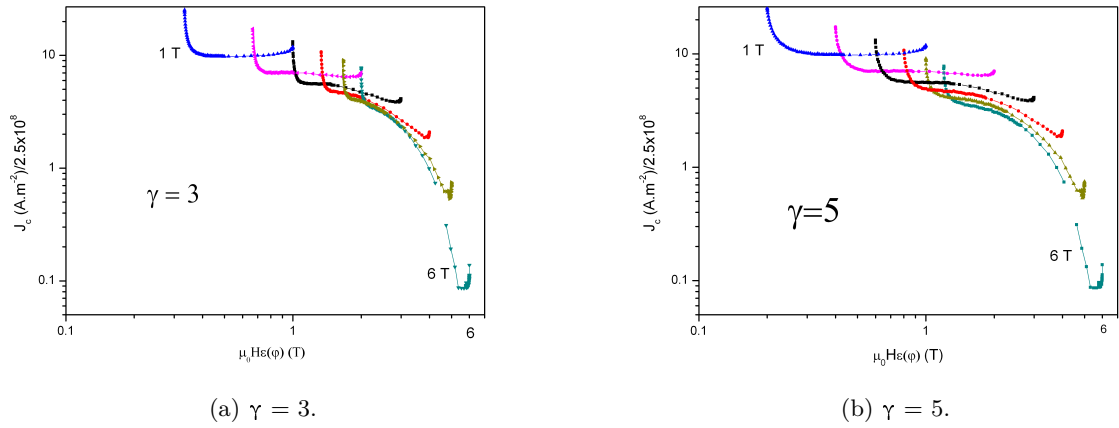


Figure 6.2: SuperPower 77 K, $J_c(H, \varphi) = J_c(\tilde{H})$ transformation.

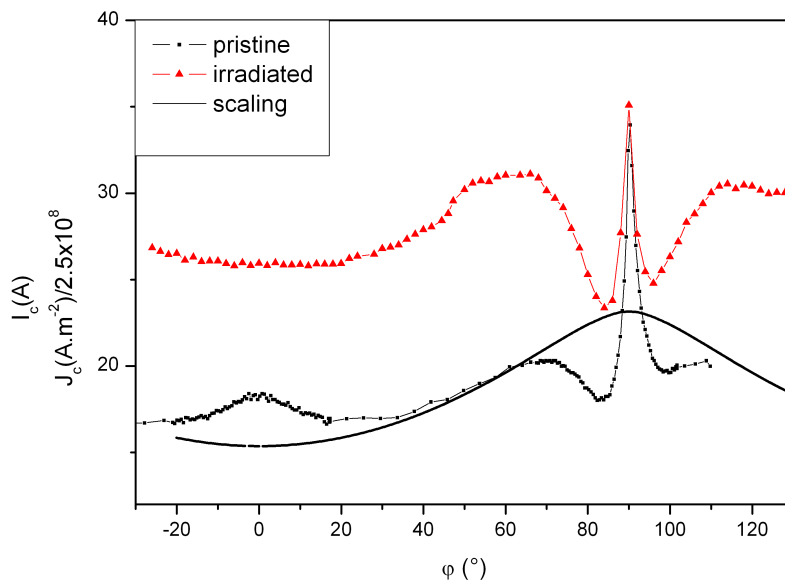


Figure 6.3: SuperPower scaling at 64 K, 6 T, red line represents angular measurements after irradiation to a fluence of $2 \times 10^{21} \text{ m}^{-2}$.

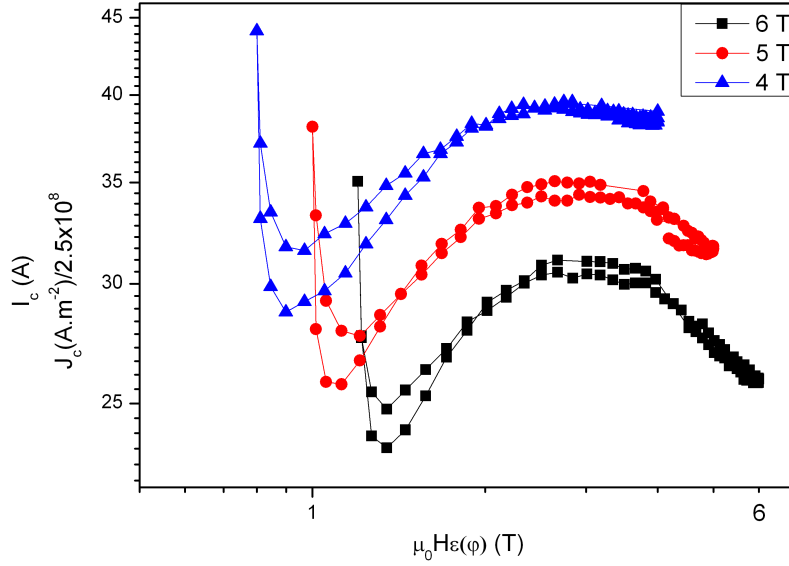


Figure 6.4: SuperPower 64 K, irradiated to $2 \times 10^{21} \text{ m}^{-2}$ $J_c(H, \varphi) = J_c(\tilde{H})$ transformation.

a generally used fit $J_c = \tilde{H}^{-\beta}$. A good match of the shape of the scaling curve $J_{c,asa}(\varphi)$ with the $J_c(\varphi)$ is noticed between 20° and 70° and only at intermediate magnetic fields. Further to the ab peak, the minimum of the “shoulder-like” feature is present. Indeed, it can not be well described by the scaling curve $J_{c,asa}(\varphi)$. The “shoulder-like” feature is even more pronounced in the measurement after fast neutron irradiation, which is shown in Figure 6.3 as well. One could notice, that the shape of this $J_c(\varphi)$ curve after irradiation, except the area close to the ab peak, corresponds quite well to the shape of the scaling curve $J_{c,asa}(\varphi)$ (Figure 6.3, $\varphi < -20, 70^\circ$). This could be easily explained as an effect of the pinning centres introduced by neutron irradiation which are randomly distributed. However, the $J_c(\varphi)$ curves of the SuperPower CC after irradiation do not obey the Blatter anisotropic scaling approach at all. The clear evidence is shown in Figure 6.4, where the transformed curves with Eq. 6.2 do not collapse at any point.

6.1.2 Strong and weak pinning

A basic knowledge of differences between strong and weak pinning is necessary to elucidate the pinning mechanism in the irradiated SuperPower tape. Strong pinning is responsible for the failure of the Blatter scaling in the case of the irradiated SuperPower tape.

The competition between elasticity of the vortex lattice and pinning produces different

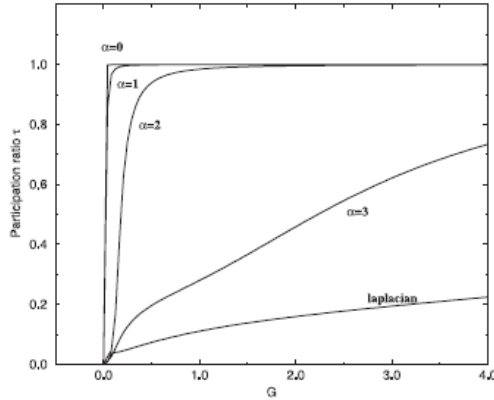


Figure 6.5: Participation ratio τ as a function of the dimensionless surface tension G [65].

phases of vortex matter in HTS [65]. The weak - collective [59] and the strong pinning regime [66] can be recognized. A complex study regarding the transformation between this two regimes has been done by A. Tanguy and T. Vettorel [67]. They studied the case of a one-dimensional elastic line driven at zero temperature on a pinning surface. Their study starts a definition of the instability criterion and with an equation for the pinning energy (Eq. 6.4):

$$V_p = - \int_0^L dx \int_0^{u(x)} dy (\gamma_{SV}(x, y) - \gamma_{SL}(x, y)). \quad (6.4)$$

where $\gamma_{SV}(x, y)$ and $\gamma_{SL}(x, y)$ are spatially varying solid-vapor and solid-liquid tensions, L is the size of a contact line and d is the distance. Weak pinning occurs if the contact line is infinitely rigid and moves as a whole. In the opposite case, each site moves independently, which corresponds to strong pinning. The distinction between strong and weak pinning was done introducing a parameter characterizing the elasticity to pinning ratio G (*dimensionless surface tension*) and the participation ratio τ (Figure 6.5).

When $\alpha \leq 1$, the elastic energy dominates at large scales and pinning is weak. When $\alpha > 1$, the pinning energy dominates at large scales: pinning is strong. As a result, the small pinning centres will act rather as weak pinning (neutron - point defects) and the big ones as the strong pinning (neutron - big spherical defects of a few nm in size).

Very often, both pinning mechanisms are present and this mixed behavior state can be very wide. A method to separate the weak pinning contribution from strong pinning was presented by J. Gutierrez et al. [62]. The $J_c(T)$ function at fixed magnetic field consists of two components: weak pinning component J_c^{weak} and the strong pinning component

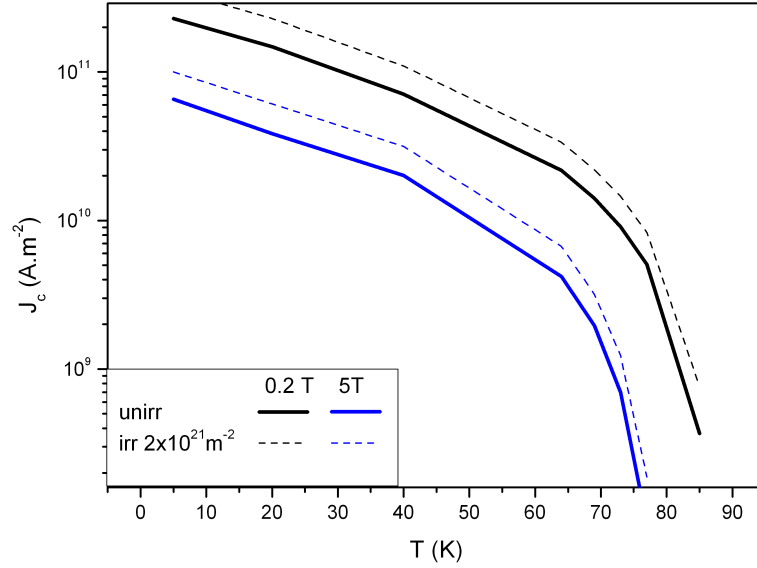


Figure 6.6: $J_c(T)$ lines for SuperPower CC before and after irradiation to $2 \times 10^{21} \text{ m}^{-2}$.

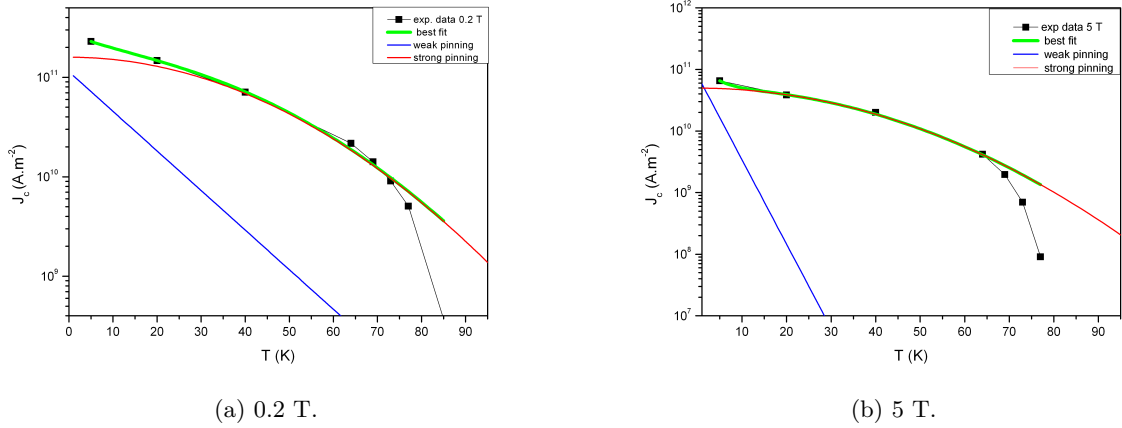
J_c^{strong} , whereby [65, 68]:

$$J_c(T) = J_c^{weak}(T) + J_c^{strong}(T) \quad (6.5)$$

$$J_c^{weak}(T) = J_c^{weak}(0) \exp(-T/T_0) \quad (6.6)$$

$$J_c^{strong}(T) = J_c^{strong}(0) \exp(-3(T/T^*)^2) \quad (6.7)$$

This method was applied to the SuperPower samples before and after irradiation. Since the magnetic measurements in the VSM have been done at a wide scale of temperatures, the data were used in Figure 6.6. It is important to call, that all the data correspond to the $H//c$ field orientation. The data were fitted by the function (Eq. 6.5), where $J_c^{weak}(0)$, $J_c^{strong}(0)$, T_0 and T^* are free parameters. The fits are shown in Figure 6.7 for two different magnetic fields. Since the differences between the fits on irradiated and unirradiated samples were negligible, Figure 6.7 represents only unirradiated samples. Moreover, the best fit curve (green) could not well describe all the experimental points. However, it shows that strong pinning dominates, which is not too surprising as the initial $J_c(T)$ dependence comes from $H//c$, where the c -axis peak arises from correlated pinning


 Figure 6.7: Separation of weak pinning from strong pinning at $H//c$.

centres, which are bigger strong pinning sites. If the sample is irradiated, strong pinning is dominant as well. Then the effective pinning centres are the defects of diameter 1-5 nm, which are strong pinning centres. Extremely interesting would be identical measurements at different magnetic field orientations, where the scaling curve is identical with the experimental points (Figure 6.3, $\varphi < \varphi_t - \varphi_{tC} >$). Unfortunately, this kind of measurements is not available in the VSM up to now. However, angular resolved measurements in the VSM were investigated by F. Hengstberger [69] resulting in very good agreement with transport measurement. Thus, it is disappointing that the fit Eq. 6.5 does not work very well for the SuperPower CC.

From these results, the following statements can be made (although they are not well proven because of missing VSM measurements at different angles and not very successful fits with Eq. 6.5):

1. The Blatter anisotropic scaling does not work for strong pinning, even when strong pinning centres are randomly distributed.
2. The effective pinning centres induced by irradiation are big defects of diameter 1-5 nm, which are strong pinning centres.

Indeed, the Blatter scaling failed for all strong pinning sites, such as the correlated pinning creating the c -axis or the ab peak. Scaling at 64 K, where the “shoulder-like” feature is pronounced, was rather complicated (Figure 6.3), and finally scaling failed after fast neutron irradiation, which introduces perfectly randomly distributed spherical defects big in size (Figure 6.4).

6.1.3 $J_c(\varphi)$ before and after irradiation

The $J_c(\varphi)$ dependence of SuperPower CC contains some interesting features after as well as before irradiation by fast neutrons. In the case of the pristine samples, the “shoulder-like” features on both sides of the ab peak were mainly pronounced at lower temperatures such as 50 K, 64 K (Figures 5.33, 5.34). Similar features were reported in studies by B. Maiorov et al. [70], who explained the “shoulder-like” feature as coming from extended particles, which exhibit a different $J_c(\varphi)$ dependence than the point-like defects. The extended particles are rather bigger strong pinning centres, just like the effective pinning centres introduced by fast neutrons. If the pinning is strong, the collective pinning theory is irrelevant and the single vortex can be considered individually.

The vicinity of the CC tape is probably not a reason explaining the deep minima beside the ab peak, although it is most likely the reason of their different sizes. According to B. Maiorov et. al [70], there are two possible scenarios responsible for the deep minima beside the ab peak. They do not exclude each other and both of them can contribute. First by the case of big pinning sites (bigger than the coherence length), the cross section of the vortex core varies in the rotating magnetic field approaching the field, where $H//ab$. This results in a reduction of the pinning energy close to $H//ab$ [71]. The other scenario is the extended pinning along the c axis. This very broad c -axis peak is also coming from some strong pinning centres, most likely oriented along the c -axis, and the minimum is then placed in the common base of the c -axis and the ab peak. However, the neutron induced defects are not correlated, but random, and they do not create a c -axis peak, but the “plateau-like” feature (Figure 5.33). Since this plateau is for some reasons lost close to the ab peak (Figure 6.8), only the first scenario can be taken into account.

Thus the minimum is created putting together the plateau contribution with the contribution of intrinsic pinning or other pinning in the ab direction. If these two contributions are added together (Figure 6.8), the final $J_c(\varphi)$ can exhibit the shape, which was reported, e.g., in Figure 5.33 after irradiation.

Also another observed phenomenon must be taken into account, when analyzing the pinning mechanism after fast neutron irradiation. At 50 K and 64 K after the irradiation to the highest fluence - $1 \times 10^{22} \text{ m}^{-2}$ (Figures 5.33, 5.34), J_c at the ab peak is significantly lower than J_c of the “shoulder-like” or the “plateau-like” features. Moreover, the “shoulder-like” or the “plateau-like” features are much less pronounced in the EHTS CC (Figure 5.44). This indicates that apart from the simple big spherical, randomly distributed pinning centres addition, another pinning mechanism is present. A similar $J_c(\varphi)$ behavior was reported by D.M. Feldmann et al. [73], who observed a dramatic change in the shape of $J_c(\varphi)$ caused by a growth temperature of YBCO by PLD. This sharp change occurred

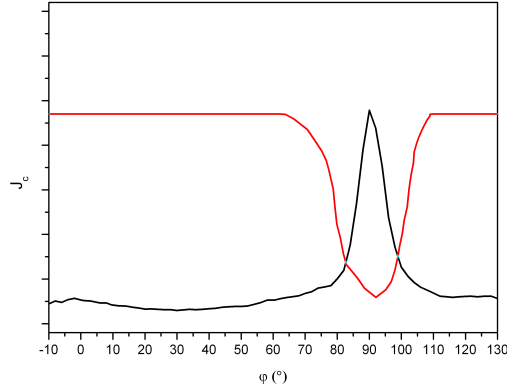


Figure 6.8: Pinning contributions to the $J_c(\varphi)$, black - regular pinning behavior, red - pinning induced by randomly distributed spherical defects.

between a temperature of 810 °C and 830 °C (pressure 200 mtorr) and it is identical to the $J_c(\varphi)$ shape change between the pristine and the irradiated SuperPower sample to a fluence of $1 \times 10^{22} \text{ m}^{-2}$ measured at rather lower temperatures (such as 64 K and 50 K). They found, that a phase transition from a Ba-Cu-O solid phase to a Ba-Cu-O liquid phase was present in this temperature range and under certain pressure [74]. The liquid Ba-Cu-O behaves similar to the hybrid-liquid phase epitaxy fabrication process [75], which may result in similar pinning centres, such as threading dislocations and secondary phases. The similar effect after fast neutron irradiation is then not so surprising considering the YBCO lattice interaction with a high energy fast neutron (Sec. 3.3.2), because the high energy of the collision causes melting of surrounding material. A TEM investigation of the CCs after irradiation is only hardly possible due to silver and copper shunts on top of the YBCO layer. However, the results from [73], where at temperatures above 830 °C, a high number of Ba-rich or Ba-deficient secondary phases has been found, seems to be a reasonable explanation.

However, the $J_c(\varphi)$ curves at 77 K on irradiated tapes are very different from those at lower temperatures. This phenomenon was already studied in [72]. It was shown from the measured n -values (Figure 5.17), that the pinning mechanism differs at 77 K and 64 K (50 K).

Table 6.1: Comparison of ITER and DEMO concept parameters [79].

	ITER	DEMO
Major plasma radius R (m)	6.2	7.5
Minor plasma radius a (m)	2	2.5
Plasma current I_p (MA)	15	20
Toroidal magnetic field B_t (T)	5.3	6
Fusion power P_{fus} (MW)	500	2410
Electrical Power P_{el} (MW)	0	~1000

6.2 Thermonuclear fusion

6.2.1 Requirements for fusion magnets

In parallel to the ITER preparation, power plant conceptual studies have been carried out for the design of a fusion demonstration reactor – DEMO [76]. The construction of DEMO is scheduled to start in about 20-30 years. Different concept possibilities were studied which have in common that DEMO will be a tokamak and the radius and the toroidal magnetic field have to be larger than that of ITER. However, strong improvements of the stellarator fusion reactor concept [77] may change the main directions of fusion research in the future from the tokamak to the stellarator concept. Thus the commercial fusion plants would be stellarators and not tokamaks. Nevertheless, this is a speculation only and DEMO will be most likely still a tokamak, as the development of the stellarator technology is about one decade behind that of the tokamaks. The coefficient Q (output energy/input energy) for ITER is estimated $Q = 10$, whilst for DEMO $Q = 25$ [78]. Higher performance, which will be needed in DEMO, can be achieved by an increased reactor size and by higher toroidal confinement fields B_t . However, the higher fields must be reached at higher temperatures to save energy for cooling. These ambitious goals can be reached by employing high temperature superconductors instead of conventional low temperature superconductors.

The ITER magnet system is presented in Figure 6.9. Different types of magnets have various requirements for the wire performance. The highest performance is needed for the toroidal field coils (TF Coils), because the plasma is confined by this magnetic field in the reactor. The design parameters for the conductors were extracted from ITER and DEMO concept studies [79]. The parameters are compared in Table 6.1.

The radial extension of a tokamak has to be considered, to determine the maximum field at the position of the conductors. The maximum field can be calculated according to J.L.

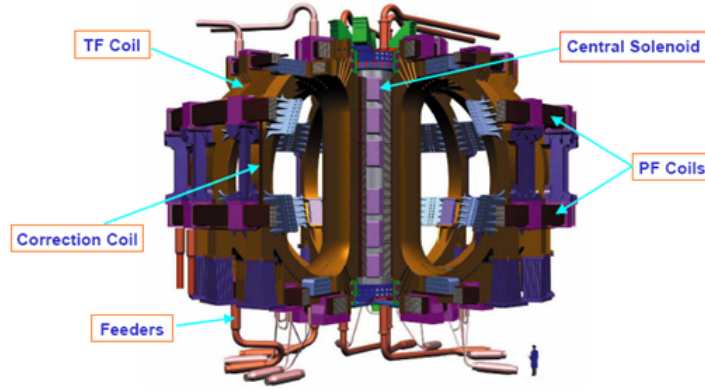


Figure 6.9: ITER magnet system, TF - Toroidal Field (18 coils), PF - Polodial Field (6 Coils).

Duchateau et al.[80] by the formula:

$$B_{tmax} = kB_{tavg} \quad (6.8)$$

$$B_{tavg} = \frac{B_t}{1 - \frac{1}{A} - \frac{\Delta_{int} - t_{cas}}{R}} \quad (6.9)$$

The required parameters for this equation, including the resulting B_{tmax} are presented in Table 6.2. The crucial parameters for the superconductors are the required critical current density of the whole wire (engineering critical current density J_{CE}) and the maximal applied magnetic field. The limits for ITER are already calculated and approved, though they are still not clear for DEMO. There are several DEMO concepts, which will be reconsidered after successful operation of ITER. Therefore, higher J_{CES} of the superconducting wires will be needed. The required engineering current densities for superconducting cables for toroidal field magnets are estimated to 5.2×10^7 A/m² for ITER [79]. Thus, it results about 1.4×10^8 A/m² for DEMO (using the factor ~ 2). ROEBEL cables [18] containing coated conductor strands are considered to be the best solution for DEMO. Thus the ratio between engineering current density and the current density of the tape will be the same as for coated conductors (coolant is not taken into account). The critical engineering current density of CCs results from the current divided by the cross-section of the whole tape, including also the not superconducting parts. It is usually about 2 orders of magnitude lower than the current densities of the superconducting layer. The engineering current density of the SuperPower CC is only 1.12 % of the current density of the superconducting layer. The corresponding ratios for EHTS and AMSC CCs are: 2.08

Table 6.2: ITER and DEMO concept parameters [80].

	ITER	DEMO
Maximum field on the conductor B_{tmax} (T)	11.8	14.6
Increasing factor due to the casing k	1.07	1.07
Average magnetic field on the conductor B_{tavg} (T)	11.02	13.62
Toroidal magnetic field B_t (T)	5.3	6
Major plasma radius to minor plasma radius ratio R/A	6.2/3.1	7.5/3
Front thickness of the casing t_{cas}	0.1	0.1
Internal plasma edge and the superconducting winding distance Δ_{int}	1.125	1.6

%, 0.5 % . With these values, it is then easy to calculate the required critical current densities for each tape to reach the needed engineering critical current densities for ITER and DEMO. These values for ITER are: for SuperPower $\sim 4.6 \times 10^9$ A/m², for EHTS CC $\sim 2.3 \times 10^9$ A/m². For DEMO they are simply multiplied by a factor 2. Here, the ~ 2.5 μ m thick YBCO layer of EHTS CC seem to be an advantage even despite the rather lower critical current densities.

6.2.2 Critical superconducting design parameters

High values of irreversibility fields in the range of 64 - 77 K are crucial for future fusion magnet applications. The irreversibility lines define, if the CC is still in the superconducting stage at fields required, e.g., for the TF coils. Unfortunately, the measurement set-up does not allow to apply fields above 15 T. As a consequence, the most interesting temperature range (64 K- 77 K) is not fully covered for none of the characterized CCs. The irreversibility lines of all 3 types of CCs are shown in Figure 6.10. The differences are rather small at the $H//ab$ field direction. Larger differences in irreversibility fields are pronounced for $H//c$. For instance at 77 K, the irreversibility field of the AMSC CC is only ~ 5 T, but the best value ~ 9 T is achieved by the EHTS CC. The SuperPower CC is in the middle of this range with an irreversibility field of ~ 7.8 T.

However, the irreversibility lines do not contain another important information on the CCs performance. The critical current density and engineering critical current density can behave differently from that one could expect from the irreversibility field dependence. The $J_{c,s}$ (J_{CES}) of the SuperPower CC together with the corresponding ITER (DEMO) requirements are shown in Figure 6.11. As discussed above, the ITER and DEMO requirements (blue line - ITER, red line - DEMO) must be calculated for the each tape separately. The requirements in the case of the EHTS CC are shown in the next plot (Figure 6.13). The

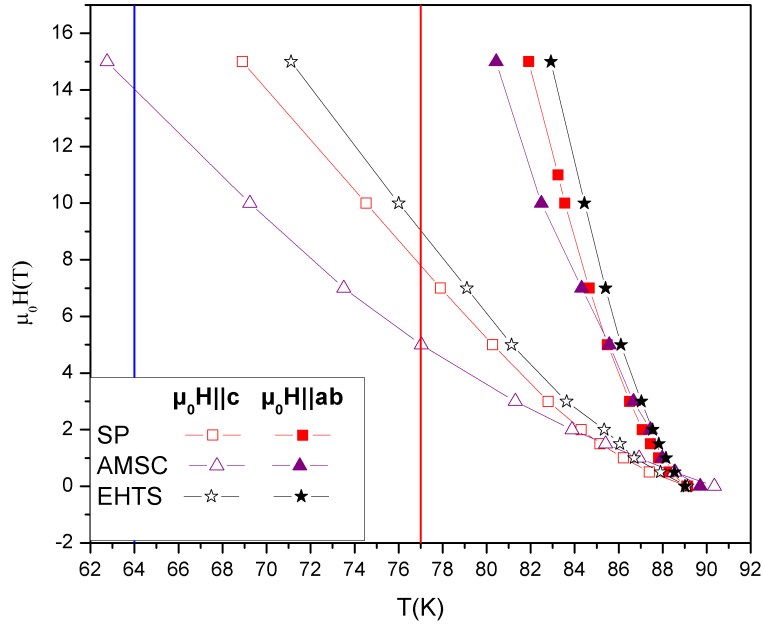


Figure 6.10: Irreversibility lines of 3 different types of CC.

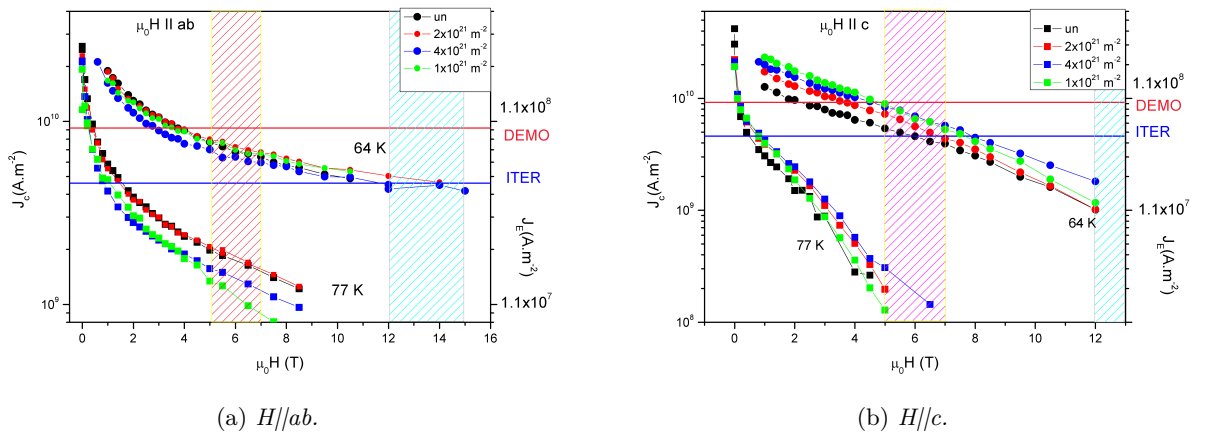


Figure 6.11: J_c of the SuperPower CC after irradiation together with the expected fusion requirements (pink area - toroidal field on axis, blue area - maximal toroidal field, central solenoid).

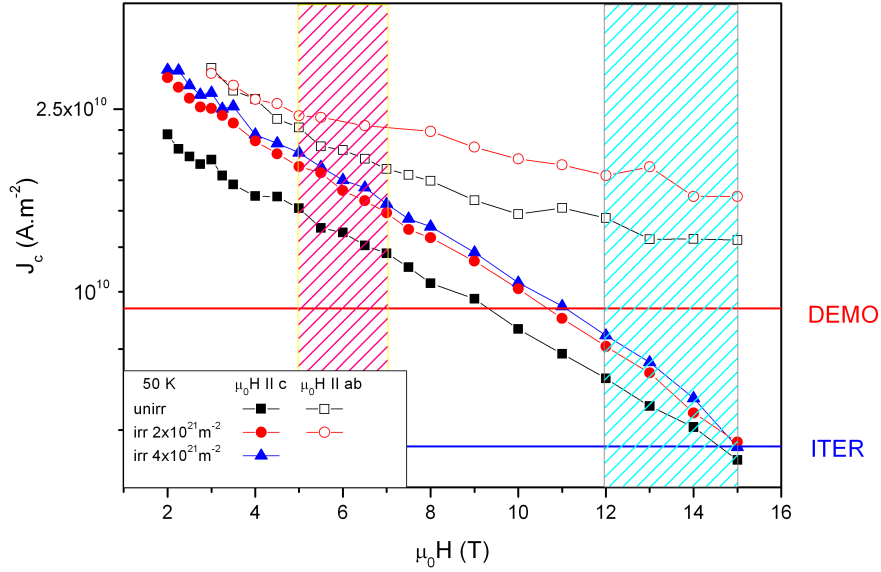


Figure 6.12: J_c of the SuperPower CC at 50 K (pink area - toroidal fields on axis, blue area - maximal toroidal field, central solenoid).

requirements are fulfilled better than in the case of the SuperPower CC. Despite of lower critical current densities of the YBCO, this tape is closer to the fusion needs than the other ones, even the SuperPower CC with the highest achieved critical current densities. The investigation has been usually performed at temperatures 50, 64 and 77 K. Unfortunately, the transport measurements at temperature of 50 K were affected by the typical problem of heating due to very high transport currents. The measurements at 50 K are presented in Figure 6.12 and the performance is above ITER and partially also above the DEMO requirements. The magnetic measurements were performed also in this temperature range, but the maximal available magnetic field of 5 T is not interesting for fusion.

However, measurements on similar CCs at temperatures of liquid helium were performed in other laboratories. Here, the samples were etched and superconducting layer abridged. Pulse magnets are often used for characterization in very high magnetic fields. This kind of measurements were performed e.g. by A. Xu et al. [81]. Their resulting J_c s are: $\sim 3.5 \times 10^{10}$ A/m² - 7 T; $\sim 2.2 \times 10^{10}$ A/m² - 15 T; $\sim 1.5 \times 10^{10}$ A/m² - 30 T at $H//c$ and $\sim 10.8 \times 10^{10}$ A/m² - 7 T; $\sim 10.8 \times 10^{10}$ A/m² - 15 T; $\sim 10.5 \times 10^{10}$ A/m² - 30 T at $H//ab$ magnetic field configuration. All of these J_c s are safely above the estimated J_c ITER and DEMO requirement for the SuperPower CC.

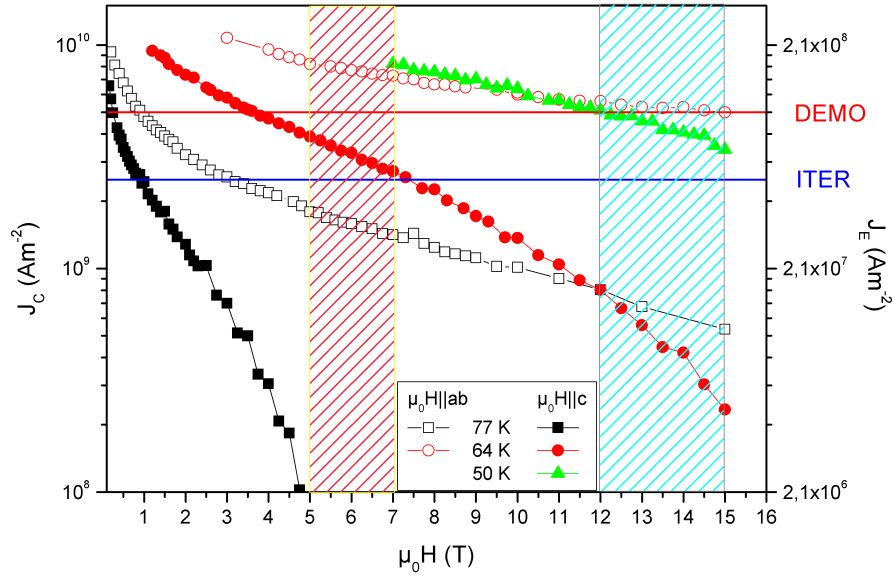


Figure 6.13: J_c of EHTS CC together with fusion requirements (pink strip - toroidal fields on axis, blue strip - max. toroidal fields, central solenoid).

6.2.3 Results and fusion requirements

The present results show an enormous potential of high temperature superconductors. Their performance at temperatures of liquid helium (~ 4.2 K) can satisfy also high requirements estimated for future fusion reactor concepts as DEMO. The projected coil systems for ITER could be easily replaced by HTS superconducting coils, if the operating temperature stays unchanged or increases only slightly. However, the employment of these materials at this temperature range does not make sense due to very high costs of the HTS materials compared to the conventional low temperature superconductors. This is also one of the reasons, why HTS have not spread to wider applications. The real chance of HTS and CC employment comes with increasing operating temperature to the range of liquid nitrogen (64 K - 77 K). This raise of the operating temperature can save an enormous amount of energy spent on cooling, which can be crucial for a fusion power plant to be effective. The energy saving on cooling was reconsidered in the ITER design either. As a result, the current leads for ITER magnets will be based on HTS materials (BSCCO) [2].

7 Summary

Coated conductors as strong candidates for future fusion applications were studied in this work. Three different kinds of commercial CCs were measured: SuperPower, EHTS and AMSC. The main focus was bond on the samples from SuperPower, which were stepwise irradiated to a fast neutron fluence of $1.3 \times 10^{22} \text{ m}^{-2}$ and fully characterized. Only parts of the characterization of the EHTS CCs was done in this work. The rest of the characterization made on the EHTS CC as well as the complete characterization of the AMSC CC can be found in the work of R. Fuger [8]. However, several additional characterizations have been performed on the AMSC CC in this work as well.

The TRIGA Mark II reactor was employed as an irradiation facility. The ZBR (Central Irradiation Facility) of the TRIGA Mark II reactor was used for the simulation of the neutron spectrum in a fusion reactor. After considering several possible problems and disagreements, the ZBR of the TRIGA Mark II reactor was evaluated to be suitable irradiation facility for irradiating CCs for fusion applications. A brief introduction into neutron physics, more precisely into possible neutron interactions with particular parts of the CCs was presented. Changes in the CCs, such as the production of activation products, were studied employing gamma spectroscopy. The SuperPower CC shows rather high radioactivity after irradiation, due to the presence of silver in the silver shunt. The half-life of decay of silver ($^{110\text{m}}\text{Ag}$) is 250 days. This fact was complicating the characterization process, since long relaxation times for the samples after irradiation were needed. Also an additional analysis dealing with the impact of the activation of the other CCs buffer layers on the superconducting properties was performed. No real impact has been found. The EHTS tape showed usually one order of magnitude lower radioactivity at the same level of irradiation than the comparable sample from SuperPower. The major part of radiation was coming from ^{60}Co in this case.

Direct transport and magnetization measurements show strong J_c enhancements after fast neutron irradiation for all CCs. The direct transport measurements were performed in: 17 T set-up, 6 T set-up, electromagnet set-up and 2-axis goniometer set-up. The MagLab VSM was used for magnetization measurements. The characterization was focused on two main goals of the thesis: evaluate the performance of the CCs before and after fast neutron irradiation with respect to fusion requirements; studies of pinning focused on the

flux pinning mechanism in the CCs after fast neutron irradiation. The results from the 17 T set-up and from the VSM were compared with fusion requirements for toroidal and central solenoid magnetic fields. From the results is concluded, that the present CCs do not fulfill the fusion requirements in the temperature range of liquid nitrogen. The SuperPower CC has the highest critical current densities. However, the EHTS CC has better properties for this application due to its thicker superconducting layer resulting in higher engineering critical current densities. The ITER requirements are well achieved already at 50 K for the EHTS CC and the SuperPower CC. At 64 K and 77 K the performance was rather insufficient for all the CCs. The good news is, that even the fluences projected over the whole ITER lifetime did not reduce the critical current densities below the values of the pristine samples, but it was usually the other way round. The bad news is, that still a lot of research and development is needed to achieve the required performance for fusion machines at temperatures of liquid nitrogen.

Fast neutron irradiation results in special phenomena of flux pinning. The angular resolved transport measurements offered the best opportunity for studies on the flux pinning mechanism. Especially the SuperPower CC shows unique $J_c(\varphi)$ curves after, but also before fast neutron irradiation. The $J_c(\varphi)$ curves exhibited extraordinary shapes, such as “shoulder-like” or “plateau-like” features. Although it is not usual to study the flux pinning mechanism on commercial CCs without any special sample preparation techniques, such as etching or patterning, the extraordinary $J_c(\varphi)$ shapes were a strong motivation to do so. Moreover, advanced measurement techniques and the employment of several set-ups allowed to perform reliable measurements in a wide range of temperatures and magnetic fields. A 2-axis high current goniometer was developed for this purpose in Cambridge. The angular resolved transport measurements in the maximal Lorentz force configuration were crucial for the flux pinning investigation. The “shoulder-like” or “plateau-like” features in the $J_c(\varphi)$ dependencies were explained on the level of microscopic flux vortices behavior. The vortex (pinned by a big defect caused by fast neutron) cross section varies close to the parallel field orientation ($H//ab$). It causes a drop of the pinning energy close to $H//ab$. The other contributions to the unique $J_c(\varphi)$ behavior are the pinning centres created after melting due to neutron collisions and following recrystallization. The pinning centres created in this way are similar to the centres created by the liquid phase epitaxy process.

Bibliography

- [1] B.D. Bondarenko, "Role played by O A Lavrentev in the formulation of the problem and the initiation of research into controlled nuclear fusion in the USSR" *Phys. Usp.* 44 844 (2001)
- [2] R. Wesche, R. Heller, P. Bruzzone, W. H. Fietz, R. Lietzow, A. Vostner, *Fusion Engineering and Design* 82 (2007), 1385–1390
- [3] J.G. Bednorz, K. A. Z. Müller, "Possible High-Tc Superconductivity in the Ba-La-Cu-O System", *Z. Phys. B* 64, 189–193, (1986)
- [4] C.Y. Han, W. Lin, Y.S. Wu, B. Yin and D.S. Tang, *Physica C* 282-287, (1997), 1189-1190
- [5] H. Takahashi, K. Igawa, K. Arii, Y. Kamihara, M. Hirano, H. Hosono, "Superconductivity At 43 K In An Iron-based Layered Compound $\text{LaO}_{1-x}\text{F}_x\text{FeAs}$ ", *Nature* 453: 376–378 (2008)
- [6] F. Seitz, "The effect of irradiation on metals", *reviews of modern physics*, vol 34, pp. 656-666, 1962
- [7] F.M. Sauerzopf, H.P. Wiesinger, W. Kraitschka, H.W. Weber, G.W. Crabtree, J.Z. Liu, *Phys. Rev. B* 43 (1991) 3091
- [8] R. Fuger, "Measurements on HTS superconductors for fusion magnets" , Phd thesis, TU Wien - Atominstitut, 2008
- [9] S. Takács, L. Cesnak, "Supravodivost' ", *Vydavatelstvo Alfa*, Dec. 1979
- [10] S.R. Foltyn, L. Civale, J.L. MacManus-Driscoll, Q.X. Jia, B. Maiorov, H. Wang, M. Maley, *Nature Materials* 6, 631 - 642 (2007)
- [11] H. Maeda, Y. Tanaka, M. Fukutumi, and T. Asano (1988). "A New High-Tc Oxide Superconductor without a Rare Earth Element", *Jpn. J. Appl. Phys.* 27 (2): L209–L210

- [12] A. Usoskin, L. Kirchhoff, J. Knoke, B. Prause, A. Rutt, V. Selskij, and D.E. Farrell, IEEE Trans. Appl. Supercond. 17, pp. 3235 - 3238, 2007
- [13] M.W. Rupich, U. Schoop, D.T. Verebelyi, C. Thieme, et al., “YBCO Coated Conductors by an MOD/RABiTSTM Process”, IEEE Trans. Appl. Supercond. 13, (2003) 2458
- [14] F.A. List, T. Kodenkandath, and M.W. Rupich, IEEE Trans. Appl. Supercond. 17, pp. 3355 - 3358, 2007
- [15] V. Selvamanickam, Y. Chen, X. Xiong, Y.Y. Xie, J.L. Reeves, X. Zhang, Y. Qiao, K.P. Lenseth, R.M. Schmidt, A. Rar, D.W. Hazelton, and K. Tekletsadik, IEEE Trans. Appl. Supercond. 17, No. 2, june 2007
- [16] http://www.superpower-inc.com/system/files/SP_2G+Wire+Spec+Sheet_for+web_0509.pdf, (november 2010)
- [17] G. Janeschitz, R. Heller, W.H. Fietz, W. Goldacker, G. Kotzyba, R. Lietzow, R. Nast, B. Obst, S.I. Schlachter, C. Schmidt, K.-R. Weiss, “High Temperature Superconductors for Future Fusion Magnet Systems – Status, Prospects and Challenges” , 21st IAEA Fusion Energy Conf., Chengdu, China, October 16-21, 2006
- [18] W. Goldacker, A. Frank, R. Heller, S.I. Schlachter, B. Ringsdorf, K.-R. Weiss, C. Schmidt, S. Schuller, IEEE Trans. Appl. Supercond. 17, pp. 3398 - 3401, 2007
- [19] H.W. Weber, H. Böck, E. Unfried, L.R. Greenwood, “Neutron dosimetry and damage calculations for the TRIGA Mark-II reactor in Vienna”, Journal of Nuclear Materials 137, 236-240, 1986
- [20] General Atomic, “Calculated Fluxes and cross sections for TRIGA reactors”, 1963
- [21] B. Batlogg, R.J. Cava, A. Jayaraman, R.B. van Dover, G.A. Kourouklis, S. Sunshine, D.W. Murphy, L.W. Rupp, H.S. Chen, A. White, K.T. Short, A.M. Majsce, and E.A. Rietman, Phys. Rev. Lett. 58, 2333, 1987
- [22] P. Vladimirov and S. Bouffard, Comptes Rendus Physique 9, pp. 303-322, 2008
- [23] V. Hlinka, “Experimentálna jadrová fyzika”, scripts, Comenius University Bratislava, Department of Nuclear Physics and Biophysics
- [24] G.M. Zhao, V. Kirtikar, K.K. Singh, A.P.B. Sinha, D.E. Morris and A.V. Inyushkin, Phys. Rev. B 54 (1996) 14956

- [25] M. Okada; T. Kawakubo, "Radiation Effects and Defects in Solids", 108, pp. 137 – 144, 1989
- [26] H. Ohyama, K. Hayamaa, K. Takakura, T. Jonoa, E. Simoen, C. Claeys, *Microelectronic Engineering* 66 (2003) 530–535
- [27] H. P. Wiesinger, F.M. Sauerzopf, H.W. Weber, H. Gerstenberg, G.W. Crabtree, *Europhys. Lett.*, 20 (6), pp. 541-546 (1992)
- [28] S.M. Khanna and A.M. Figueredo, "Proton Irradiation Effects on Critical Current of Single-Crystal Superconducting YBCO Wire", *IEEE Trans. Nucl. Sci.* 44, pp. 1870 - 1877 , 1997
- [29] H. Ozkan, B. A. Albiss, N. Hamdan, A. Menard, *Journal of Superconductivity* 7, 885-888, 1994
- [30] J. Giapintzakis, W.C. Lee, J.P. Rice, D.M. Ginsberg, I. M. Robertson, *Physical Review B* 45, 10677–10683, 1992
- [31] Design description document of magnets, IDM number : ITER_D_22HV5L
- [32] R. Herzog and J. E. Evetts, "Low-Temperature 2-Axis Goniometer With Accurate Temperature Control" *Rev. Sci. Instr.* 65 (11), 3574 (1994)
- [33] T.D. Withnell, K.R. Schöppl, J.H. Durrell, and H.W. Weber, *IEEE Trans. Appl. Supercond.* 19, 2925, 2009
- [34] Oxford Instruments Superconductivity, "Vibrating Sample Magnetometer Superconducting system with integral VTI", Version 1.0, July 2000
- [35] C. P. Bean, "Magnetization of hard superconductors", *Phys. Rev. Lett.* 8 (1962) 250
- [36] M. Zehetmayer, "Anisotropic magnetic properties of superconductin MgB₂ and HgBa₂CuO_{4+δ} single crystals", PhD Thesis TU Wien - Atominstitut, 2003
- [37] G. Blatter, V. B. Geshkenbein, A. I. Larkin, *Phys. Rev. Lett.* 68 (1992) 875
- [38] B. Mayorov, S.A. Baily, H. Zhou, O. Ugurlu, J.A. Kennison, P.C. Dowden, T.G. Holesinger, S.R. Foltyn and L. Civale, *Nature* 8, 398, 2009
- [39] P. Paturi, M. Irjala and H. Huhtinen, *J. Appl. Phys.* 103, 123907, 2008

- [40] R.C. Budhani, Y. Zhu and M. Suenaga, "Flux Pinning By Heavy-Ion-Irradiation Induced Linear Defects In $\text{YBa}_2\text{Cu}_3\text{O}_7$ Epitaxial Films", AIP Conf. Proc. 273, pp. 171-178, 1992
- [41] V. Selvamanickam, A. Guevara, Y. Zhang, I. Kesgin, Y. Xie, G. Carota, Y. Chen, J. Dackow, Y. Zhang, Y. Zuev, C. Cantoni, A. Goyal, J. Coulter and L. Civale, Supercond. Sci. Technol. 23 (2010) 014014 (6pp)
- [42] Y. Chen, V. Selvamanickam, Y. Zhang, Y. Zuev, C. Cantoni, E. Specht, M. P. Paranthaman, T. Aytug, A. Goyal, D. Lee Appl. Phys. Lett. 94, 062513, 2009
- [43] B. Maiorov, B. J. Gibbons, S. Kreiskott, V. Matias, T. G. Holesinger, L. Civale, Appl. Phys. Lett. 86, 13204, 2005
- [44] Z. Chen, F. Kametani, Y. Chen, Y. Xie, V. Selvamanickam, D.C. Larbalestier, Supercond. Sci. Technol. 22 (2009) 055013
- [45] A.V. Silhanek, L. Civale and M.A. Avila, Phys. Rev. B 65 (2002), p. 174525.
- [46] M.J. Hogg, F. Kahlmann, Z.H. Barber and J.E. Evetts, Supercond. Sci. Technol. 14 (2001), p. 647.
- [47] K.R. Schöppl, H.W. Weber and J.H. Durrell, Physica C 460 (2007), p. 1188.
- [48] A.A. Zhukov, H. Küpfer, H. Claus, H. Wühl, M. Kläser and G. Müller-Vogt, Phys. Rev. B 52 (1995), p. R9871
- [49] M. Oussena, P.A.J. de Groot, K. Deligiannis, A.V. Volkozub, R. Gagnon and L. Taillefer, Phys. Rev. Lett. 76, 2559, 1996
- [50] A.A. Zhukov, G.K. Perkins, J.V. Thomas, A.D. Caplin, H. Küpfer and T. Wolf, Phys. Rev. B 56 (1997), p. 3481
- [51] B. Dam, J.M. Huijbregtse, F.C. Klaassen, R.C.F. van der Geest, G. Doornhos, J.H. Rector, A.M. Testa, S. Freisem, J.C. Martínez, B. Stäubli-Pümpin and R. Griessen, Nature Mat. 399 (1999), p. 439.
- [52] A. Diaz, L. Mechin, P. Berghuis and J.E. Evetts, Phys. Rev. Lett. 80 (1998), p. 3855
- [53] S.A. Harrington, J.L. MacManus-Driscoll, J.H. Durrell, Appl. Phys. Lett. 95 (2009) 022518
- [54] M. Eisterer, S. Haindl, T. Wojcik, and H. W. Weber, Supercond. Sci. Technol. 16 (2003) 1282

- [55] R. Fuger, F. Hengstberger, M. Eisterer, and H.W. Weber, *IEEE Trans. Appl. Supercond.* 17, pp. 3753 - 3756, 2007
- [56] K. Matsumoto, T. Horide, A. Ichinose, S. Horii, Y. Yoshida, M. Mukaida, *Jpn. J. Appl. Phys.* 44 (2005) 246–248
- [57] M. Eisterer, R. Fuger, M. Chudy, F. Hengstberger and H WWeber, *Supercond. Sci. Technol.* 23 (2010) 014009 (6pp)
- [58] R. Fuger, M. Eisterer, F. Hengstberger, H.W.Weber, *Physica C* 468 (2008)1647
- [59] A.I. Larkin and Yu Ovchinnikov, "Pinning in type II superconductors", *J.Low Temp.Phys.* 34, 409-428, 1979
- [60] L. Civale, B. Maiorov, A. Serquis, J. O. Willis, J. Y. Coulter, H. Wang, Q. X. Jia, P. N. Arendt, J. L. MacManus-Driscoll, M. P. Maley, and S. R. Foltyn, *Appl. Phys. Lett.* 84, (2004), 2121a
- [61] A.V. Silhanek, L. Civale, *Journal of Low Temperature Physics*, Vol. 135,p.157-60, 2004
- [62] J. Gutierrez, A. Llodes, J. Gazquez, M. Gibert, N. Roma , S. Ricard, A. Pomar, F. Sandiumenge, N. Mestres, T. Puig and X. Obrados, *Nature Mater.* 6, 367, 2007
- [63] N.J. Long, *Supercond. Sci. Technol.* 21 (2008) 025007 (8pp)
- [64] N.J. Long, private communication
- [65] G. Blatter, M.V. Feigelman, V.B. Geshkenbein, A.I. Larkin, V.M. Vinkour, *Rev. Mod. Phys.* 66 (1994) 1125
- [66] R. Labusch, *Cryst. Lattice Defects* 1 (1969) 1
- [67] A. Tanguy and T. Vettorel, *Eur. Phys. J. B* 38, 71–82 (2004)
- [68] D.R. Nelson, V.M. Vinokur, "Boson localization and correlated pinning of superconducting vortex arrays", *Phys. Rev. B* 48, 13060–13097 (1993).
- [69] F. Hengstberger , private communication
- [70] B Maiorov, A Kursumovic, L Stan, H Zhou, H Wang, L Civale, R Feenstra and J L MacManus-Driscoll, *Supercond. Sci. Technol.* 20 (2007) S223–S229
- [71] Yu. N. Ovchinnikov and B. I. Ivlev, *Phys. Rev. B* 43, 8024 (1991)

- [72] M. Chudy, M. Eisterer and H.W. Weber, *Physica C* 470, p. 1300-1303, 2010
- [73] D. M. Feldmann, O. Ugurlu, B. Maiorov, L. Stan, T. G. Holesinger, L. Civale, S. R. Foltyn, and Q. X. Jia, *Appl. Phys. Lett.* 91, 162501, 2007
- [74] J.L. MacManus - Driscoll, J.C. Bravman, and R.B. Beyers, *Physica C* 241, 401, 1995.
- [75] A. Kursumovic, J.E. Evetts, J.L. MacManus-Driscoll, B. Maiorov, L. Civale, H. Wang, Q.X. Jia and S.R.Foltyn, *Appl. Phys. Lett.* 87 (2005) 252507
- [76] D. Maisonnier, I. Cook, S. Pierre, B. Lorenzo, Di Pace Luigi, G. Luciano, N. Prachai, “DEMO and fusion power plant conceptual studies in Europe”, *Fusion Engineering and Design* 81 (2006) 1123
- [77] J.F. Lyon , “Recent advances in stellarator development”
- [78] <http://fusionforenergy.europa.eu/>
- [79] J.L. Duchateau, P. Hertout, J. Johner, *EEE Trans. Appl. Supercond.* 17, pp. 1342 - 1347, 2007
- [80] J.L. Duchateau, J.M. Rey, P. Roussel, EFDA Contract TW4-TMS-HTSMAG: Final Report, AIM/NTT-2007.004 (2007)
- [81] A. Xu, J.J. Jaroszynski, F. Kametani, Z. Chen, D.C. Larbalestier, Y.L. Viouchkov, Y. Chen, Y. Xie , V. Selvamanickam, *Supercond. Sci. Technol.* 23 (2010) 014003 (7pp)

Curriculum Vitae

Personal Information

Name: Michal Chudý

Address: Alliiertenstrasse 4, 1020 Vienna, Austria

E-mail: chudy4@gmail.com

Date of birth: 09.02.1984

Place of birth: Želiezovce, Slovak Republic

Nationality: Slovak

Language skills: Slovak (mother tongue), Czech, English, German, Russian

Education & Work experience

- 1994 - 2002 Secondary School : Gymnázium A. Vrábla, Levice
- 2002 – 2007 University : Faculty of Mathematics, Physics and Informatics - Comenius University, Bratislava, Slovak Republic section: Physics, since 2004 Department of Nuclear Physics and Biophysics, specialization: Nuclear physics
- 2004 – 2007 University: Faculty of Social and Economic Sciences - Comenius University, Bratislava, Slovak republic specialization : European studies and international relations
- October 2007 PhD research (Project Assistant) at Vienna University of technology - Atominstitut, Vienna, Austria

List of Publications

- M. Eisterer, R. Fuger, M. Chudý, F. Hengstberger and H.W. Weber, "Neutron irradiation of coated conductors", Supercond. Sci. Technol. 23 (2010) 014009

- M.Chudý, M. Eisterer, H.W. Weber, "Asymmetric angular dependence of J_c in coated conductors prior to and after fast neutron irradiation", *Physica C* 470 (2010) pp.1300-1303
- M.Chudý, R. Fuger, M. Eisterer, H.W. Weber, "Characterization of commercial YBCO coated conductors after neutron irradiation", submitted *IEEE Trans. Appl. Sup.* August 2010